TECHNISCHE UNIVERSITÄT MÜNCHEN
LEHRSTUHL FÜR HOCHFREQUENZTECHNIK

Echo Suppression Techniques for Near-Field Antenna Measurements

Kazeem Yinusa

Vollständiger Abdruck der von der Fakultät für Elektrotechnik und
Informationstechnik der Technischen Universität München
zur Erlangung des akademischen Grades eines

- *Doktor-Ingenieurs* -

genehmigten Dissertation.

Vorsitzender: Univ.-Prof. Dr.-Ing. habil., Dr. h.c. Alexander W. Koch
Prüfer der Dissertation:
1. Univ.-Prof. Dr.-Ing. Thomas Eibert
2. Prof. Olav Breinbjerg
Technical University of Denmark / Dänemark

Die Dissertation wurde am 19.05.2015 bei der Technischen Universität München
eingereicht und durch die Fakultät für Elektrotechnik und Informationstechnik
am 22.09.2015 angenommen.

Acknowledgements

I would like to first and foremost, thank my doctoral advisor, Prof. Thomas Eibert, for his support and encouragement during the course of my research work at the Institute for High-Frequency Engineering. This work would not have been possible without his insightful comments and guidance. The several human and technical skills which I learned by interacting with him has made me a better researcher and a more prepared person for future challenges and opportunities.

I would like to thank Dr. Carsten Schmidt who introduced me to the field of antenna measurements. His support and insights during the course of this work are very much appreciated. Many thanks to Prof. Olav Breinbjerg of the Technical University of Denmark for reviewing this work. To Dr. Ayyaz Qureshi and Raimund Mauermayer for reviewing the first draft of this thesis and for their helpful suggestions. To all my friends and colleagues who have supported me in any way during the course of my doctoral research.

Special thanks to my family especially my parents, Hon. Yahaya Yinusa and Hajiya Adama Yinusa, for their unconditional love and support. I am eternally grateful.

Contents

Abbreviations

AUT	Antenna Under Test
BW	Bandwidth
CG	Conjugate Gradient
dB	Decibel
DFT	Discrete Fourier Transform
DUT	Device Under Test
EPIC	Extended Probe Instrument Calibration
EL	Error Level
FFT	Fast Fourier Transform
FIAFTA	Fast Irregular Antenna Field Transformation Algorithm
GHz	Gigahertz
GMRES	Generalized Minimum Residual Solver
IFFT	Inverse Fast Fourier Transform
LHCP	Left Hand Circular Polarization
LOS	Line-of-Sight

MARS	Mathematical Absorber Reflection Suppression
MLFMM	Multilevel Fast Multipole Method
MP	Matrix Pencil
MPM	Matrix Pencil Method
NFFFT	Near-Field Far-Field Transformation
OEWG	Open-Ended Waveguide
PCA	Principal Components Analysis
PWE	Plane Wave Expansion
PWRC	Plane Wave Receiving Characteristic
PWS	Plane Wave Spectrum
RAM	Radiation Absorbent Material
RHCP	Right Hand Circular Polarization
SER	Signal to Echo Ratio
SVD	Singular Value Decomposition
SWE	Spherical Wave Expansion
TE	Transverse Electric
TDOA	Time Difference of Arrival
TM	Transverse Magnetic
TSVD	Truncated Singular Value Decomposition
TZF	Test Zone Field

Nomenclature

$\mathbf{A}$	Matrix
$\boldsymbol{A}$	Vector
$\\|\boldsymbol{A}\\|$	Magnitude of a vector
$\hat{\boldsymbol{A}}$	Unit vector
$(\cdot)^H$	Conjugate complex transpose
$\bar{\boldsymbol{A}}$	Dyad
$\lceil x \rceil$	Smallest integer not less than x
∇	Nabla operator

List of Symbols

$\mathbf{C}$	coupling matrix
$U(\boldsymbol{r}_\mathrm{M})$	probe signal at measurement position $\boldsymbol{r}_\mathrm{M}$
dx, dy, dz	infinitesimal length elements
θ, ϕ, r	spherical coordinate components
e_θ, e_ϕ, e_r	spherical unit vectors
λ	wavelength
$\mathbf{j}$	imaginary unit
k	wavenumber
η	antenna radiation efficiency
x, y, z	Cartesian coordinate components
$\hat{x}, \hat{y}, \hat{z}$	Cartesian unit vectors
k_x, k_y, k_z	wavenumber in x-,y- and z-direction
π	constant (pi = 3.1415...)
χ_o, θ_o, ϕ_o	Euler angles
$Q_{smn}^{(c)}$	spherical wave coefficients

$\vec{F}^{(c)}_{smn}$	spherical vector wave functions
$P_{s\mu n}(kA)$	probe response constants
T_{smn}	transmitting coefficients of an antenna
$R^{p}_{\sigma\mu\nu}$	receiving coefficients of an antenna
$C^{sn(c)}_{\sigma\mu\nu}(kA)$	spherical translation coefficients
$d^{n}_{\mu m}(\theta)$	rotation coefficients
N	multipole order of AUT
$\tilde{\boldsymbol{J}}(\hat{k})$	plane wave coefficients of AUT
$T_L(\hat{k},\boldsymbol{r}_{\mathrm{M}})$	fast multipole method translation operator
L	multipole order of the translation operator
$h^{(2)}_l(kr_{\mathrm{M}})$	spherical Hankel function of the second kind
$P_l(\hat{k}\cdot\hat{r}_{\mathrm{M}})$	Legendre polynomial
ω	angular frequency
σ	relative residual
ε	near-field residual
$C^1_\phi(k_{\phi 1},k_{\theta 1},\phi_1,\theta_1)$	components of the coupling matrix
$W(k_{\theta_q})$	weighting function
$\bar{\boldsymbol{D}}^{i_n}_n(\boldsymbol{k},\boldsymbol{r}^{i_n}_n)$	combined disaggregation and anterpolation operator
$\bar{\boldsymbol{V}}_n(\hat{k})$	anterpolation operator
S_{ij}	scattering matrix coefficients

Abstract

Near-field antenna measurements are usually performed in an anechoic chamber in order to ensure a free-space interaction between the antenna under test (AUT) and the probe. However, for electrically large antennas or for in-situ antenna measurements, the cost of building and maintaining an anechoic chamber can be prohibitively high due to the required space. Measurements can be performed in these cases in a semi-anechoic or in an outdoor measurement facility. When near-field antenna measurements are performed in semi-anechoic or outdoor facilities, the measured near-field distribution is contaminated with multipath signals. These errors in the near-field distribution are carried over to the far field if adequate steps are not taken to remove the errors. Echo suppression can be performed during the actual data acquisition or during the application of a near-field far-field transformation (NFFFT) algorithm.

NFFFT algorithms relate the measured near-field distribution to the far-field pattern of the AUT. Examples of such algorithms include the modal expansion techniques and techniques based on equivalent currents. Recently, a plane-wave based near-field far-field transformation algorithm has been presented. The algorithm utilizes a translation operator derived from the fast multipole method (FMM) to translate outgoing plane waves from the AUT to incident plane waves at the probe. It allows the efficient processing of measurements acquired on an irregular grid and it includes capabilities for full probe correction.

In this thesis, novel measurement and signal processing techniques for obtaining reliable antenna measurement results in non-anechoic facilities are presented. This is achieved by a careful modification of either the measurement procedure or the post-processing steps. The presented techniques are applied to simulated and actual echoic data and the results are compared to those obtained from echo-free measurement data. Substantial improvement in the measurement results were obtained by the following approaches:

- By utilizing certain a priori knowledge about the measurement geometry in a spatial filtering formulation. Auxiliary sources with associated plane wave spectra are assumed for echo sources during the process of near-field far-field transformation. These additional plane wave spectra are translated to the measurement points and superimposed on the incident plane waves from the AUT. This representation improves the model of the inverse problem formulation such that the model is closer to the actual source arrangement from which the near-field data was acquired. The echo sources are assumed to be localized and translations of plane waves are performed from the echo locations to the measurement points. The advantage of localized echo sources is that only the minimum number of unknowns are introduced to the problem by considering the echo sources. When the locations of the echo sources are not known, a technique for determining the directions of the most dominant echo sources is presented. Also, when echo localization is not feasible, a technique for representing non-localized echo sources is presented.

- The manner in which the auxiliary sources are formulated is such that the technique is applicable to measurements that are acquired on non-canonical measurement geometries as opposed to some existing filtering techniques which depend on canonical set-ups for echo suppression. The presented techniques can, therefore, be utilized with conformal or non-redundant sampling strategies. Conformal and non-redundant sampling techniques are becoming important as the enormous sizes of test antennas present new challenges that are not well suited to traditional antenna measurement techniques.

- Additional unknowns which are introduced by an assumption of additional sources for the echo sources typically require additional information for sources that are outside the measurement volume. A multi-probe measurement technique for providing additional information about all the sources in a multipath measurement environment is presented. The technique is based on measuring the field distribution with an inward looking and an outward looking sets of probes. Additional information can also be obtained by utilizing two oppositely directed Huygens' source. Huygens' sources measure a linear combination of the electric and the magnetic fields. This measure-

ment technique provides the information required to resolve both the outgoing and incident wave on the measurement volume.

- Probe antennas operate as spatial filters on the near-field as well as angular filters of the far-field. Directive probes, therefore, have the advantage of filtering off-axis multipath signals. However, traditional near-field antenna measurements are not well-suited for directive probes. For instance, multiple interactions between the AUT and the probe can be a setback. Also, numerical errors can result due to probe insensitivity in certain directions in the forward hemisphere of the probe for planar measurements. In this thesis, a beamforming technique which filters off-axis multipath signals is presented. The technique depends on combining neighboring measurement signals with appropriate weights such that the synthetic probe array is steered towards the AUT. The actual measurement is performed with a small probe in order to avoid multiple reflections. Probe correction is also performed using the far-field pattern of the small probe in order to avoid numerical errors.

- For an arbitrary measurement surface enclosing the AUT, the same number of AUT modes are captured in the measurement data once adequate sample spacing and measurement distance are utilized. However, for echo sources outside the measurement surface, the echo contributions change with the particular measurement distance. In order to identify and suppress the multipath components, a technique derived from principal component analysis (PCA) is investigated. Measurements are performed on multiple measurement surfaces with varying measurement distances. The measurement data on the different measurement surfaces are then processed jointly with the plane wave based NFFFT algorithm or by applying the singular value decomposition (SVD) to the obtained far-field patterns for each measurement.

The presented techniques typically require additional information in form of additional measurements. However, they will help to relax the usually stringent requirements for an anechoic chamber when performing near-field antenna measurements.

Chapter 1

Introduction

An important step after the design and fabrication of antennas is the testing stage when the antenna is measured in order to assess its radiation parameters. Such measurements are necessary, for example, to confirm that the fabricated antenna satisfies certain design specifications such as the required radiation pattern, cross-polarization, gain, directivity, etc. and that it conforms with government regulations [IEEE, 2013]. The most important antenna parameter is the field pattern which gives the radiation properties of the antenna as a function of direction. Since antennas are usually employed in order to convey energy to far away distances, the most informative radiation pattern is that which characterizes the antenna in the far-field. The far-field is the region starting from a commonly accepted radial distance of $2D^2/\lambda$ from the antenna, where D is the largest dimension of the antenna and λ is the wavelength [Balanis, 2005]. The amplitude of the electric field in this region decays linearly with distance and the waves can be assumed to have a locally planar wavefront. The far-field pattern of an antenna under test (AUT) or generally a device under test (DUT) can be obtained by a direct far-field measurement. Measurements in the far-field are quite straight-forward for antennas whose radiation characteristics satisfy the far-field criteria at a relatively short distance from the antenna. A short distance makes it practical to provide a controlled environment necessary to avert errors due to echoes, electromagnetic interference and to avoid security lapses. As the DUT becomes electrically larger, the far-field boundary emerges farther away from the antenna and direct far-field measurements can become inconvenient due to the required space. Direct far-field measurements in these cases can be achieved by means of compact antenna ranges. In compact ranges, one or more collimating reflectors are used to create a region of plane waves, called the quiet zone, in front of a reflector [Dudok and Fasold, 1986, Hartmann et al., 2002, Olver, 1991]. However, due to the required equipments, compact ranges can be expensive to set-up. Near-field techniques [Yaghjian, 1986] allow measurements at shorter distances and provide adequate information for the determination of the test antenna parameters and for antenna diagnostics [Lee et al., 1988, Leibfritz et al., 2007b]. To obtain the far-field pattern, the measured near-field data is processed with a near-field far-field transformation (NFFFT) algorithm [Johnson et al., 1973, Ludwig, 1971, Petre and Sarkar, 1994]. NFFFT algorithms relate the measured near-field data to equivalent sources which are initially unknown. The choice of the equivalent source type typically depends on the acquisition geometry. Plane wave, cylindrical wave, and spherical wave expansions are easily related to measurements acquired on planar, cylindrical, and spherical measurement surfaces, respectively. Once the equivalent sources are obtained, the field values can be evaluated outside the source region. Recently, a plane wave based NFFFT algorithm has been developed in which the AUT is represented by means of a set of outgoing plane waves on the complete unit sphere [Schmidt et al., 2008]. The outgoing plane waves from the AUT are translated into incident waves at the probe by means of a diagonal translation operator derived from the Fast Multipole Method (FMM). The incident plane waves are then weighted by the far-field pattern of the probe to correct for the probe influences. The formulation of the algorithm is such that no particular measurement geometry is assumed, therefore, any arbitrary scanning surface can be selected. Also, full probe correction is possible for arbitrary probes without effect on the efficiency of the algorithm. The algorithm and other NFFFT algorithms are reviewed in detail in Chapter 2.

In order to obtain accurate results of the far-field pattern from near-field measurements, it is essential that measurements are carried out in an environment devoid of multipath propagation. As such, antenna measurements are usually carried out in anechoic chambers. An anechoic chamber is a room shielded to prevent electromagnetic waves penetrating from outside and interior lined with Radiation Absorbent Material (RAM) to prevent reflections off the walls, ceiling and floor of the room. However, in certain situations, especially for electrically large antennas or when antennas are tested in-situ, i.e. while they are mounted within the final operating environment, it can be quite challenging to move the whole structure into an anechoic chamber. Moreover, the cost of building large anechoic chambers can be prohibitively high. Alternatives in these situations include outdoor

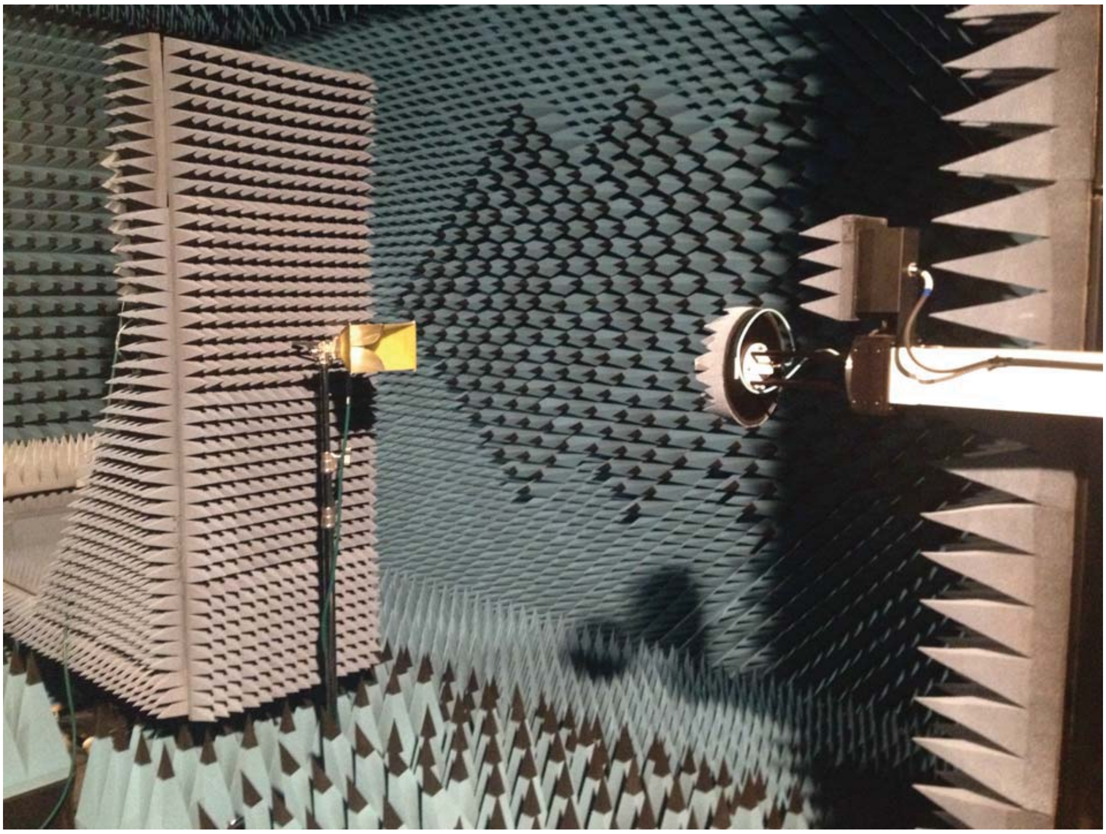

Figure 1.1: Interior of the anechoic chamber at the TU München.

measurements or measurements in a semi-anechoic environment. It is known in such measurements that the measured near-field data will be corrupted with multipath contributions. Far-field patterns obtained via near-field measurements and NFFFT algorithms are particularly prone to errors due to multipath propagation since errors in a single near-field data point affect the obtained far-field values for several directions. Techniques dealing with suppressing multipath signals in antenna measurements have, therefore, gained significant research attention. Various techniques have been suggested to improve the quality of measurements acquired in non-anechoic environments including Matrix Pencil (MP) and Fast Fourier Transform (FFT) based algorithms. Both techniques attempt to identify the line-of-sight signal from a broadband measurement [Leon et al., 2008, Leon Fernandez et al., 2009, Loredo et al., 2004]. The need for a broadband measurement, however, means that these methods are not suitable for narrowband antennas. Furthermore, they can result in a substantial increase in measurement time for broadband antennas. Recent research efforts have been dedicated to multipath suppression using a single frequency measurement [Black and Joy, 1995, Cano-Fácila et al., 2011, Direen et al., 2009, Gonzalez et al., 2011, Gregson et al., 2009, Hess, 2010, Hindman and Newell, 2005, Pogorzelski, 2009, 2010, Toivanen et al., 2010, Wittmann, 1990]. In [Hindman and Newell, 2005] and [Gregson et al., 2009], a modal filtering technique applicable to measurements on canonical geometries is described. The multipath suppression is achieved by altering the measurement set-up and by eliminating the higher order modes which result from multipath signals.

The source reconstruction method has also been extended for multipath suppression [Gonzalez et al., 2011], where the equivalent sources are obtained over a surface encompassing the desired source and the disturbers. The increment in the computational domain, however, can be substantial when the multipath sources are not in close proximity with the AUT, leading to unrealistic sample spacing and measurement distance. The same restriction is applicable to the modal technique presented in [Hess, 2010]. Outward probes or interior scanning in spherical measurements was proposed by Wittmann et al. in [Wittmann, 1990] and [Direen et al., 2009] for the Test Zone Field (TZF) evaluation, whereby measurements are taken over a sphere in order to determine the incident field within the test volume. Subsequently, TZF compensation and extended probe instrument calibration (EPIC) [Black and Joy, 1995, Pogorzelski, 2009, 2010, Toivanen et al., 2010] techniques were introduced requiring an initial measurement in the measurement chamber. The knowledge gained from this measurement is then used to correct for the room reflections in subsequent measurements of the AUT. In [Black and Joy, 1995, Toivanen et al., 2010] a spherical mode analysis of the test zone field is carried out using measurements of a calibration antenna with known spherical mode coefficients. The TZF is then removed from the AUT measurement during subsequent measurements and post-processing. In [Pogorzelski, 2009, 2010], room reflections are considered by calibrating and correcting for the effect of an extended probe which includes the effect of reflections from fixed objects in the measurement room. However, room calibration has to be carried out whenever there is a change in the scattering situation of the room and the mentioned techniques have only been considered for measurements acquired on a spherical geometry. Non-canonical measurement geometries are sometimes desireable because of some advantages such as non-redundant sampling [Bucci and Gennarelli, 2102, Bucci et al., 1996, 1998, D'Agostino et al., 2012, Qureshi et al., 2013], reduction of multiple reflections [Qureshi et al., 2012a], etc. All of the mentioned single frequency echo suppression methods still have rather restricted performance, in particular for the suppression of multipath signals emanating from locations beyond the measurement surface or when measurements are acquired on non-traditional geometries. Details of these techniques and a literature review of echo suppression in antenna measurements are presented in Chapter 3.

In this thesis, the effect of multipath signals on far-field patterns obtained from echoic near-field measurements is studied. Measurement approaches and post-processing procedures are then developed in order to improve the quality of such measurements acquired in echoic environments. Specifically, in terms of post-processing procedures, spatial filtering methods are investigated. Spatial filtering depends on the fact that AUT signals and echo signals originate from different locations. The plane wave based algorithm is well suited to exploit the source locations for echo suppression since translations of plane waves can be efficiently performed to and from arbitrary locations. In Chapter 4, the scattering centers representation of non-anechoic measurement environments is presented. In this technique, additional sets of outgoing plane waves are assumed for each echo source and plane wave translations are carried out from the echo locations to the measurement points. In this way, the echo sources are integrated into the NFFFT process and their contributions are retrieved and separated from that of the AUT by solving an inverse problem.

Integrating echo sources that are outside the measurement volume within the NFFFT process introduces additional unknowns which requires additional information during near-field measurements. Measurement approaches involve the use of an additional or a special type of hardware or field acquisition in such a way that more information is obtained about the multipath signals. For example, the multi-probe measurement technique measures the AUT with two sets of probe antennas namely: the inward and outward looking set of probes or two oppositely directed Huygens' sources. This measurement procedure aids the subsequent removal of echo contributions by means of auxiliary sources. This measurement technique is presented in Chapter 5.

The difference between the AUT and echo source locations is exploited further in Chapter 6 with the beamforming technique. Unlike the scattering centers approach where auxiliary sources are assumed for the echo sources, the beamforming technique seeks to focus the probes' main radiation on the AUT and attenuating the echo signals. It is well known that a field probe acts as a filter for the measured AUT fields, whose influence can be either described in spatial or in spectral domain. Directive probes, for instance, serve to filter out signals that originate far away from the boresight axis. However, there are several drawbacks to the use of such directive probes including the possibility of multiple reflections and probe nulls. Beamforming techniques are used to generate the effects of a directive probe without the previously stated disadvantages. The AUT is measured with a small probe antenna in the usual manner. Neighboring measurement signals are thereafter combined in a moving average manner in order to generate the signal as would be measured by a highly directive probe array. The generated near-field signals are then transformed using the plane wave based near-field far-field transformation algorithm. Probe correction does not reverse the reduction in multipath signals achieved by the use of a directive probe or beamforming since sources are assumed only within the minimum sphere enclosing the AUT.

In Chapter 7, statistical techniques for echo suppression are presented. These techniques depend on multiple measurement surfaces to collect additional information about the echo signals and to cancel the effects of multipath errors in the far-field. The thesis is concluded in Chapter 8 with a summary.

Chapter 2

Overview of Near-Field Far-Field Transformation Algorithms

An antenna is a transducer which serves as an interface between guided and unguided waves. As a transmitter, an antenna converts alternating currents to radiated electromagnetic waves and vice versa as a receiver. Antennas are an important component of several modern wireless communication devices such as mobile phones, TVs, etc. They are used to control and optimize the radiation or reception of electromagnetic power. The characteristics of an antennas are defined by certain key properties and parameters.

2.1 Antenna Parameters

2.1.1 Directivity and Gain

An isotropic antenna is an hypothetical antenna which radiates power equally in all directions. In reality, antennas radiate preferentially in certain directions than others. Directivity is a parameter which defines the degree to which an antenna concentrates its radiated energy in a particular direction in space. Specifically, it is defined according to [IEEE, 2013] as “the ratio of the radiation intensity in a given direction from the antenna to the radiation intensity averaged over all directions”, i.e.

$$D = \frac{4\pi U}{P_{\text{rad}}}, \tag{2.1}$$

where P_{rad} is the total radiated power and U is the radiation intensity in a specific direction. Directivity is a function of direction but it is often used to refer to the maximum directivity when the direction is not specified. The directivity requirement of an antenna can vary according to its application. For instance, in a line-of-sight microwave radio relay or satellite dish antennas, it is desireable for the involved antennas to be highly directive in the direction in which the signal is expected to be received or transmitted. However, the requirement for a mobile phone antenna, for instance, is different since electromagnetic waves can arrive in any direction depending on the users environment. For such applications, a less directive antenna is desired. Gain also measures the directionality of an antenna. It is related to directivity by

$$G = \eta D, \tag{2.2}$$

where η is known as the radiation efficiency. The radiation efficiency $\eta = P_{\text{rad}}/P_{\text{in}}$ is the ratio between the total radiated power by the antenna to the accepted power by the antenna. The term accepted power means that gain does not include losses due to polarization or impedance mismatch. Radiation efficiency is always between 0 and 1 meaning that the gain of an antenna in a particular direction is usually less than the directivity in the same direction. Both parameters are dimensionless quantities and are usually given in decibels (dB), i.e.

$$D = 10\log(D) \text{ dB}. \tag{2.3}$$

2.1.2 Polarization

Polarization is a property of an antenna that describes the plane in which the electromagnetic wave received or transmitted by the antenna is polarized in the far zone. The polarization of an electromagnetic wave is the path along which the time-varying electric field vector oscillates at a fixed observation point. There are three main categories of polarizations as shown in Fig. 2.1. Polarization can be represented by two orthogonal components $\mathbf{E}_x$ and $\mathbf{E}_y$. Vertical and horizontal polarization belong to the linear polarization category where the trace of the field vector is either horizontal $\mathbf{E}_x$ or vertical $\mathbf{E}_y$ as seen from an observation point along the direction of propagation. Waves with $||\mathbf{E}_x|| = ||\mathbf{E}_y||$ and having

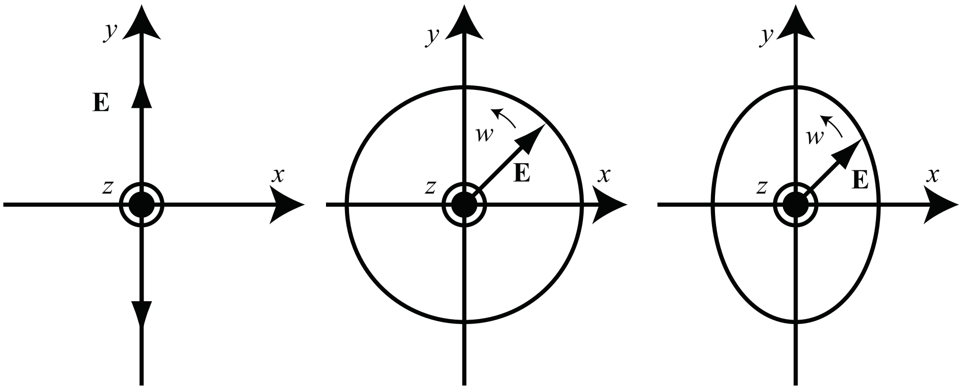

(a) Linear polarization (b) Circular polarization (c) Elliptical polarization

Figure 2.1: Different types of polarizations.

a phase difference of 90° between the two orthogonal components are circularly polarized. Depending on the direction of the trace, circular polarization can be either right hand circular polarization (RHCP) or left hand circular polarization (LHCP). Waves that are neither linearly or circularly polarized are said to have elliptical polarization. In this category, the orthogonal components have different magnitudes and can have arbitrary phase difference. For efficient reception of electromagnetic wave, the receiving antenna has to be polarization matched with the incoming wave. Polarization mismatch between the incident wave and a receiving antenna results in polarization mismatch losses.

2.1.3 Input Impedance

An antenna is usually operated within electronics systems where it either receives or transmits electromagnetic waves. The input impedance of an antenna is the impedance seen from the point of view of the connected electronics. For a transmitting antenna, power is supplied to the antenna by means of a generator with peak voltage V_g and an internal impedance

$$Z_g = R_g + \mathrm{j}X_g. \tag{2.4}$$

The antenna itself can also be represented by an impendance

$$Z_A = (R_L + R_r) + \mathrm{j}X_A, \tag{2.5}$$

where R_L and R_r are the loss resistance and radiation resistance, respectively, of the antenna. The Thevenin equivalent circuit with these components is depicted in Fig. 2.2 [Balanis, 2005]. The power delivered to the antenna goes towards radiation through R_r and losses in form of heat dissipation in R_L. The remaining power is dissipated in the internal resistance R_g of the generator. In order to deliver maximum power to the antenna, the antenna and the generator must be conjugate matched i.e. when

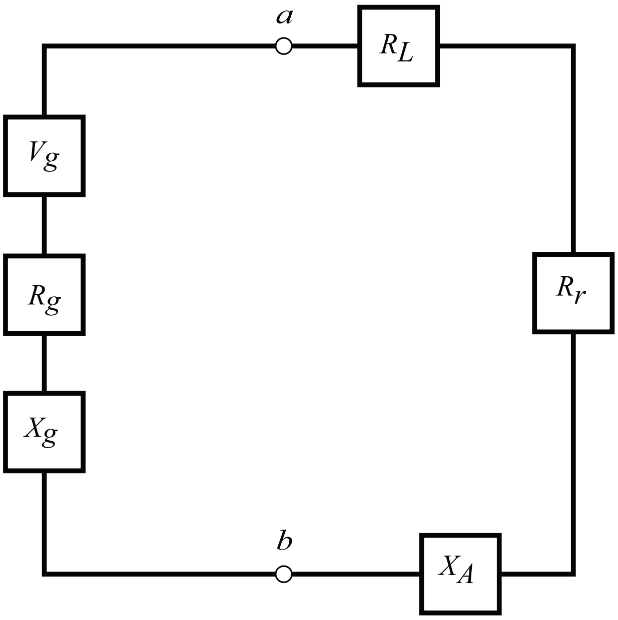

Figure 2.2: Equivalent circuit of an antenna connected to a generator.

$$R_r + R_L = R_g \tag{2.6}$$

and

$$X_A = -Xg. \tag{2.7}$$

Under these conditions, half of the power provided by the generator is dissipated as heat in the internal resistance of the generator and the other half is delivered to the antenna. The amount that goes towards radiation depends on the antenna radiation efficiency

$$\eta = \frac{R_r}{R_r + R_L}. \tag{2.8}$$

2.1.4 Bandwidth

The bandwidth of an antenna is the range of frequencies in which the performance of the antenna does not degrade according to some criterion. The criterion maybe input impedance, shape of the radiation pattern, beamwidth, etc. Broadband antennas are the antennas whose performance fulfil certain specifications for a relatively wide range of frequencies. Narrowband antennas are those that have an acceptable characteristics within only a small frequency range.

2.2 Antenna Field Regions

The space surrounding an antenna is usually categorized into three field regions, namely, the reactive near-field, the radiating near-field and the far-field or Fraunhofer regions as shown in Fig. 2.3. The reactive near field is typically the region in the immediate vicinity of the antenna up to a distance of about $0.62\sqrt{D^3/\lambda}$ [Balanis, 2005]. In this region, either the electric field or magnetic field dominates such that the power density is predominantly reactive. In the radiating near field, the radiating components of the field start to become dominant but the field distribution in this region varies depending on distance. Near-field measurements are carried out in this region because of the reduced multiple interactions between the AUT and the probe. The most interesting field region from the perspective of

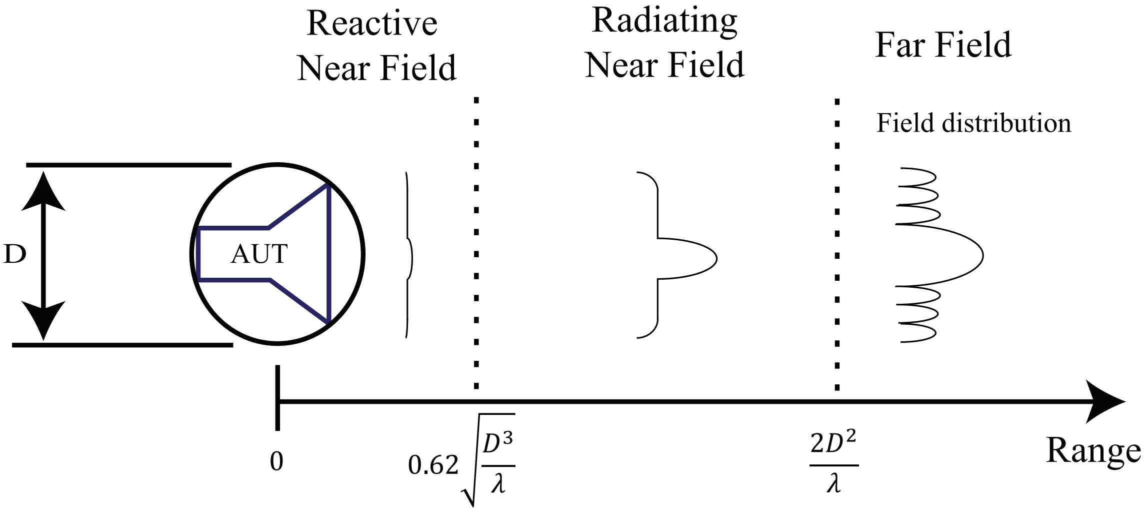

Figure 2.3: Antenna Field Regions.

antenna applications is the far-field region because antennas are usually evaluated based on their ability to convey energy efficiently over relatively large distances. The far-field region begins at a distance of about $2D^2/\lambda$. The shape of the radiation pattern in the far field is independent of distance and the waves can be assumed to have a locally planar wavefront with radial dependence $\exp(\mathrm{j}kr)/r$. In order to obtain the far-field pattern by near-field measurements, the field distribution in the near field is measured and the measurements are transformed to the far field by means of NFFFT algorithms. Due to the band limited nature of the radiated field, the field distribution can be acquired by taking discrete samples over a chosen surface following a sampling criterion. The NFFFT is achieved by replacing the AUT with some equivalent sources such as equivalent electric and magnetic currents or eigenmodes and relating the measured near-field data to the assumed equivalent sources. Equivalent sources are then obtained by solving an inverse problem and correcting for the probe antenna influences [Laitinen and Breinbjerg, 2008, Paris et al., 1978, Sánchez-Escuderos et al., 2010]. Once the equivalent sources are obtained, the field values can afterwards be computed outside the source region. The far-field pattern is usually expressed in terms of two complex orthogonal polarization basis. There are several possible options for choosing polarization basis and coordinate systems depending on the orientation of the AUT during measurements and the measurement geometry [Ludwig, 1973, Masters, 2014]. In this thesis, the far field is plotted on the polar spherical polarization basis where the field is resolved onto two unit vectors one aligned to each of the two spherical unit vectors $\hat{e}_\theta$ and $\hat{e}_\phi$. The coordinate system is the spherical coordinate system with angle ϕ ranging from 0° to 360° and angle θ from 0° to 180°.

There are three classical acquisition geometries, planar, cylindrical and spherical measurement geometries as shown in Fig. 2.4, Fig. 2.5 and Fig. 2.6, respectively. These geometries are easily associated with modal NFFFT algorithms where plane wave expansion, cylindrical wave expansion and spherical wave expansion are utilized for planar, cylindrical and spherical measurement geometries, respectively.

2.3 Planar Near-Field Measurements

The planar near-field measurement [Hajian et al., 1993, Wang, 1988] set-up is widely used because of its simplicity in terms of the required measurement hardware and the ease of obtaining the far-field pattern from planar near-field data. The planar acquisition involves a measurement of the near-field distribution over a plane located at a distance d away from the AUT, as shown in Fig. 2.4. The AUT is usually fixed and the probe moves horizontally and vertically with a fixed orientation along the scan plane. For practical reasons, the scan plan is truncated when the near-field signal has fallen considerably with respect to the maximum. Due to the finite size of the scan plane, only an angular segment of the far field is obtained from planar measurements. The valid angles,

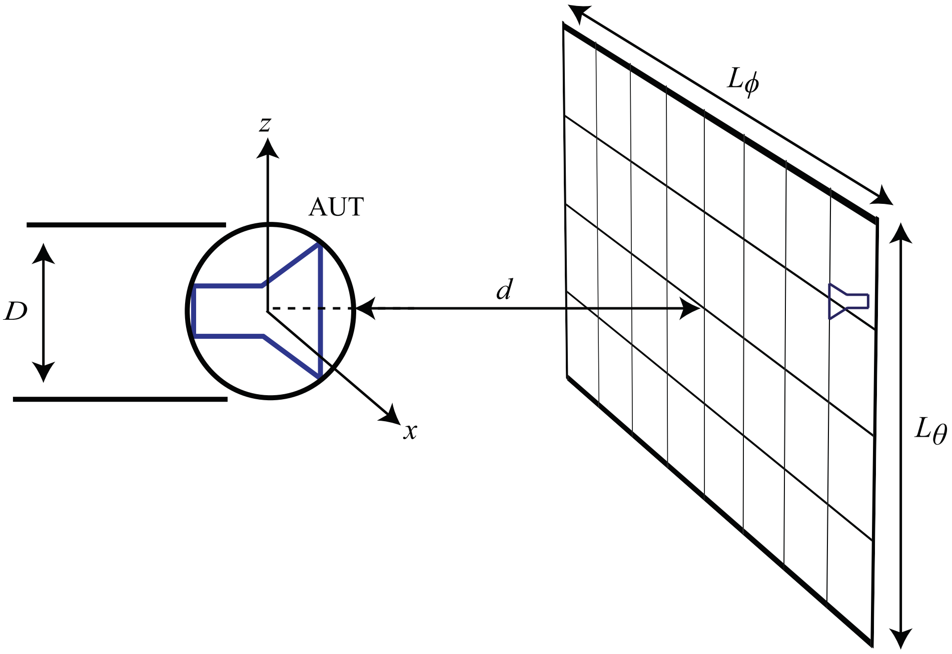

Figure 2.4: Planar measurement set-up.

$$\phi_v = \arctan\left(\frac{L_\phi - d_\phi}{2d}\right) \tag{2.9}$$

and

$$\theta_v = \arctan\left(\frac{L_\theta - d_\theta}{2d}\right) \tag{2.10}$$

are the angular ranges for which the far field can be obtained reliably from the near-field measurement [Newell and Crawford, 1974, Yaghjian, 1975]. In Eq. (2.9) and Eq. (2.10), L_ϕ and L_θ are the lengths of the scan plane, where a is the separation distance between the AUT and the measurement plane and d_ϕ and d_θ are the dimensions of the AUT. The finite extent of the scan plane results in a truncation error in the far-field [Bucci and Migliore, 2006, D'Agostino et al., 2007, Newell, 1988]. In order to minimize the truncation error, the near field should be acquired until its magnitude falls to about $-35\,\mathrm{dB}$ relative to the peak. As such, planar measurements are more appropriate for directive antennas where most of the radiated energy can be captured with a limited scan plan size. The transmission equation [Newell, 1988]

$$U'(\boldsymbol{r}_\mathrm{M}) = F'a_o \int\!\!\int t_{10}(\boldsymbol{K})S'_{02}(\boldsymbol{K})e^{\mathrm{j}\gamma d}e^{\mathrm{j}\boldsymbol{K}\cdot\boldsymbol{r}_\mathrm{M}}\mathrm{d}\boldsymbol{K}, \tag{2.11}$$

relates the measured probe signal $U'(\boldsymbol{r}_\mathrm{M})$ to the transmitting function $t_{10}(\boldsymbol{K})$ of the AUT and the probe's plane wave spectrum receiving characteristic (PWRC) $S'_{02}(\boldsymbol{K})$. The probe position in the measurement plane is denoted by $\boldsymbol{r}_\mathrm{M}$ and $\boldsymbol{K}$ is the transverse component of the propagation vector $\boldsymbol{k}$, i.e.

$$\boldsymbol{K} = k_x\hat{x} + k_z\hat{z}, \tag{2.12}$$

and

$$\gamma = \sqrt{k^2 - K^2} \tag{2.13}$$

is the y-component of the propagation vector. Also, in Eq. (2.11), the constant

$$F = \frac{1}{1 - \Gamma_l\Gamma_p} \tag{2.14}$$

is a mismatch correction term where Γ_l and Γ_p are reflection coefficients of the load and the probe, respectively. By taking the Fourier transform of the measured signal $U'(\boldsymbol{r}_\mathrm{M})$, the coupling product

$$D'(\boldsymbol{K}) = \frac{e^{-\mathrm{j}\gamma d}}{4\pi^2 F'a_o} \int\!\!\int U'(\boldsymbol{r}_\mathrm{M})e^{-\mathrm{j}\boldsymbol{K}\cdot\boldsymbol{r}_\mathrm{M}}\mathrm{d}\boldsymbol{r}_\mathrm{M}, \tag{2.15}$$

with

$$D'(\boldsymbol{K}) = t_{10}(\boldsymbol{K})S'_{02}(\boldsymbol{K}) \tag{2.16}$$

is obtained. Eq. (2.16) provides a single equation for the two unknown components of $t_{10}(\boldsymbol{K})$. The second equation,

$$D''(\boldsymbol{K}) = t_{10}(\boldsymbol{K})S''_{02}(\boldsymbol{K}) \tag{2.17}$$

is obtained by taking a second measurement utilizing a probe which has a PWRC that is linearly independent from the first probe. In practice, the first probe is simply rotated by an angle of 90° around the y-axis for the second measurement. The components of the probe corrected transmission function of the AUT

$$t_{10\mathrm{m}} = \frac{D'(\boldsymbol{K})S''_{02\mathrm{c}}(\boldsymbol{K}) - D''(\boldsymbol{K})S'_{02\mathrm{c}}(\boldsymbol{K})}{s'_{02\mathrm{m}}s''_{02\mathrm{c}} - s'_{02\mathrm{c}}s''_{02\mathrm{m}}} \tag{2.18}$$

and

$$t_{10\mathrm{c}} = \frac{D''(\boldsymbol{K})S'_{02\mathrm{m}}(\boldsymbol{K}) - D'(\boldsymbol{K})S''_{02\mathrm{m}}(\boldsymbol{K})}{s'_{02\mathrm{m}}s''_{02\mathrm{c}} - s'_{02\mathrm{c}}s''_{02\mathrm{m}}} \tag{2.19}$$

are obtained by solving Eq. (2.16) and Eq. (2.17) [Newell, 1988]. Processing of the discrete near-field data is accomplished through the discrete form of Eq. (2.16) and Eq. (2.17). In order to take the advantages of the FFT, planar near-field measurements are usually done with equal sample spacing. To satisfy the Nyquist sampling criterion, a maximum sample spacing of $\Delta x \le \lambda/2$ and $\Delta z \le \lambda/2$ is required. The sets of wavenumbers defined by the FFT are

$$k_x = \frac{2\pi m}{M\Delta x}; \qquad \frac{-M}{2} \le m \le \frac{M}{2} - 1 \tag{2.20}$$

$$k_z = \frac{2\pi n}{N\Delta z}; \qquad \frac{-N}{2} \le n \le \frac{N}{2} - 1 \tag{2.21}$$

where M and N are the number of near-field samples along the x- and z-directions of the measurement plane, respectively. The number of k samples in each direction is the same as the number of measurement samples in the corresponding direction. However, once the Nyquist sampling criterion is fulfilled, the near-field data can be padded with zeros in order to achieve higher resolution in the spatial frequency domain. Once the transmitting coefficients of the AUT are obtained, the electric far field

$$E(r,\boldsymbol{K}) = \frac{\mathrm{j}ka_o e^{-\mathrm{j}kr}}{r} t_{10}(\boldsymbol{K})\cos\theta \tag{2.22}$$

can be evaluated as derived in [Newell, 2009].

2.4 Cylindrical Near-Field Measurements

Certain types of antennas, such as base station antennas, feature fan-beam radiation patterns owning to their elongated shape. This means that, whereas planar scanning is suitable for the plane in which the antenna is elongated and in which the pattern is narrow, the broad pattern in the orthogonal plane will require a prohibitively large scan plane size in that direction. A cylindrical scan geometry, shown in Fig. 2.5, allows for such antennas to be measured fully in the direction in which the radiation pattern is broad while having a truncation similar to the planar measurement in the other direction. The AUT is usually mounted on a positioner capable of rotating around the azimuth direction while the probe only moves vertically over each step in azimuth. Similar to planar measurements, a valid angle

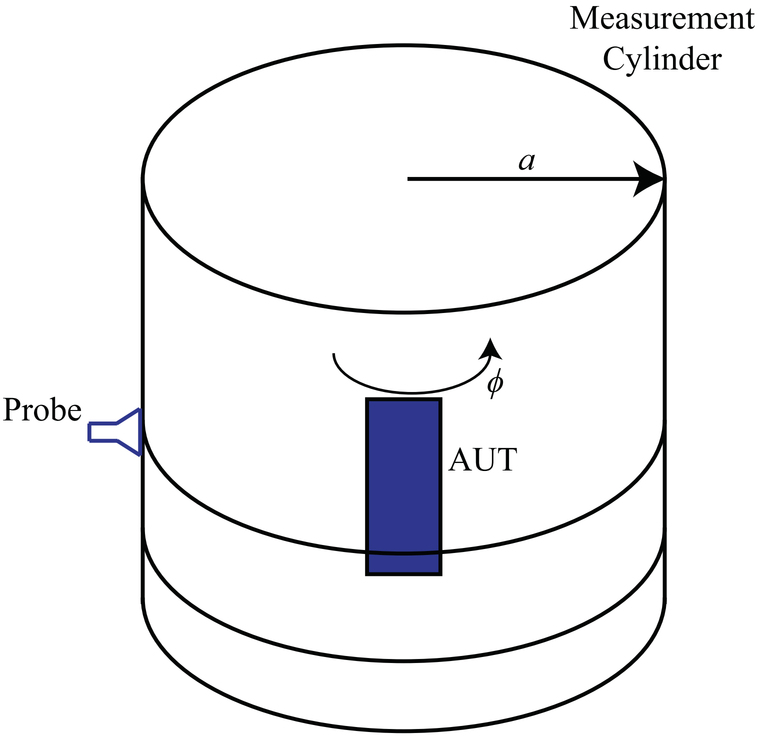

Figure 2.5: Cylindrical measurement set-up.

$$\theta_v = \arctan\left(\frac{L_\theta - d_\theta}{2a}\right) \tag{2.23}$$

is defined where a and L_θ are the radius and length of the cylindrical scan surface, respectively. If the cylinder is also truncated along the azimuth direction, a second valid angle

$$\phi_v = \phi_t - \arcsin\left(\frac{\rho_o}{a}\right) \tag{2.24}$$

is defined where ρ_o is the radius of the minimum cylinder enclosing the AUT [Balanis, 2008]. The sampling criterion along the vertical axis is $\Delta z \leq \lambda/2$ similar to that of planar measurements and the angular sample spacing

$$\Delta\phi \leq \frac{360^\circ}{2N+1} \tag{2.25}$$

is chosen according to the size of the AUT where $N = k\rho_o$ is the number of azimuthal modes. Modal NFFFT for cylindrical near-field measurement is accomplished by means of cylindrical wave expansion. The transmission equation [Yaghjian, 1977]

$$U'(\phi_o, z_o) = F'a_o \int_{-\infty}^{\infty} \sum_{n=-\infty}^{\infty} \sum_{s=1}^{2} R_n'^s(\gamma) T_n^s(\gamma) e^{\mathrm{j}n\phi_o} e^{\mathrm{j}\gamma z_o} \mathrm{d}\gamma, \tag{2.26}$$

relates the probe signal $U'(\phi_o, z_o)$ at measurement point (ϕ_o, z_o) to the AUT cylindrical wave transmitting function $T_n^s(\gamma)$ and the probe cylindrical wave receiving function $R_n'^s(\gamma)$. Using Fourier series for n and Fourier integral for γ, the coupling product

$$I_n'(\gamma) = \sum_{s=1}^{2} R_n'^s(\gamma) T_n^s(\gamma) = \frac{1}{4\pi^2 a_o} \int_{-\infty}^{\infty} \int_0^{2\pi} U'(\phi_o, z_o) e^{-\mathrm{j}n\phi_o} e^{-\mathrm{j}\gamma z_o} \mathrm{d}\phi_o \mathrm{d}z_o \tag{2.27}$$

is written in terms of the measurement signal. A second measurement is obtained with a second probe to set up the second equation of the coupling product. The components of the transmission functions of the AUT

$$T_n^1(\gamma) = \frac{\frac{I_n'(\gamma)}{R_n'^1(\gamma)} + \frac{I''{}_n(\gamma)}{R_n''^2(\gamma)} \frac{R_n'^2(\gamma)}{R_n'^1(\gamma)}}{1 - \frac{R_n'^2(\gamma)}{R_n'^1(\gamma)} \frac{R_n''^1(\gamma)}{R_n''^2(\gamma)}} \tag{2.28}$$

and

$$T_n^2(\gamma) = \frac{\frac{I''{}_n(\gamma)}{R_n''^2(\gamma)} + \frac{I'{}_n(\gamma)}{R_n'^1(\gamma)} \frac{R_n''^1(\gamma)}{R_n''^2(\gamma)}}{1 - \frac{R_n'^2(\gamma)}{R_n'^1(\gamma)} \frac{R_n''^1(\gamma)}{R_n''^2(\gamma)}} \tag{2.29}$$

are obtained by expanding Eq. (2.27) where $I''{}_n(\gamma)$ is obtained from the second probe. Once these coefficients are computed the asymptotic far electric field components

$$E_\theta(r \to \infty, \theta, \phi) = 2\mathrm{j}k_o \sin(\theta) \sum_{n=-\infty}^{\infty} (-\mathrm{j})^n T_n^2(\gamma) e^{\mathrm{j}n\phi}, \tag{2.30}$$

and

$$E_\phi(r \to \infty, \theta, \phi) = -2\mathrm{j}k_o \sin(\theta) \sum_{n=-\infty}^{\infty} (-\mathrm{j})^n T_n^1(\gamma) e^{\mathrm{j}n\phi} \tag{2.31}$$

can then be found anywhere else in space by summing up the mode coefficients [Leach and Paris, 1973, Yaghjian, 1977]. The mode summation can be truncated at $n = N$ without introducing significant errors into the transformation process.

2.5 Spherical Near-Field Measurements

In spherical near-field measurements, the near-field distribution of the AUT is measured over a sphere. A typical spherical measurement set-up is shown in Fig. 2.6. The probe antenna samples the near-field distribution of the AUT over the measurement sphere with the angular sample spacing,

$$\Delta\theta, \Delta\phi \leq \frac{360^\circ}{2N+1}. \tag{2.32}$$

In Eq. (2.32), $N = kr_{min} + n_1$ is the multipole order of the AUT where r_{min} is the radius of the minimum sphere enclosing the AUT. The value of n_1 is chosen according to the measurement distance and the required accuracy. It is often set to $n_1 = 10$ [Hansen, 1988] for relatively good accuracy. Spherical scanning is used when it is desired to obtain a wider range of angles than can be obtained through planar and cylindrical measurement since the complete angular range can be obtained in principle through spherical measurements. Modal NFFFT is accomplished in spherical measurements by means of spherical wave expansion (SWE). The electric field

$$E(\phi, \theta, r) = k\sqrt{Z_{F0}} \sum_{c=3}^{4} \sum_{s=1}^{2} \sum_{n=1}^{\infty} \sum_{m=-n}^{n} Q_{smn}^{(c)} \vec{F}_{smn}^{(c)}(\phi, \theta, r) \tag{2.33}$$

is written as a superposition of spherical waves $\vec{F}_{smn}^{(c)}(\phi, \theta, r)$ with spherical mode coefficients $Q_{smn}^{(c)}$ where (s,m,n) are the mode indices with $s = 1$ and $s = 2$ representing the transverse electric (TE) and the transverse magnetic (TM) modes, respectively [Ludwig, 1971]. The index n can be truncated at $n = N$ without introducing significant errors in the expansion since the mode coefficients are very small for higher indices $n > N$. N is chosen according to the electrical size of the AUT as explained previously. The upper index (c) specifies the radial dependence of the spherical wave function with $(c) = 3$ corresponding

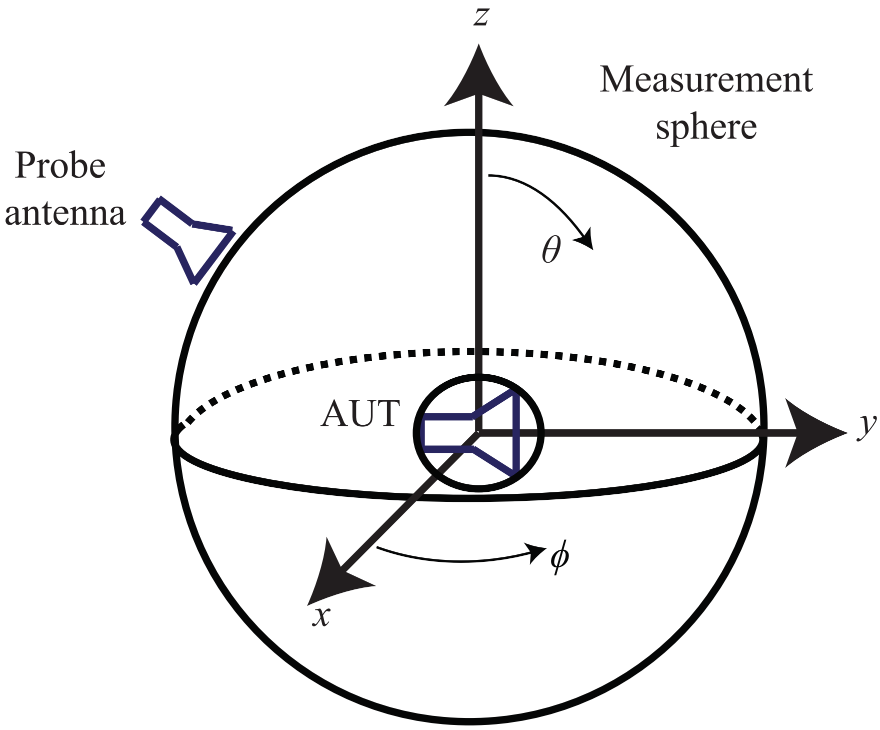

Figure 2.6: Spherical measurement set-up.

to the spherical Hankel function of the first kind or outgoing spherical waves and $(c) = 4$ corresponds to spherical Hankel function of the second kind or incoming spherical waves. When sources are restricted within the measurement sphere, $(c) = 3$ is sufficient for the expansion. Processing of sampled measurement data is done through the spherical transmission equation

$$w'(A,\chi,\theta,\phi) = \sum_{\substack{smn\\ \mu}} vT_{smn}e^{\mathrm{j}m\phi}d^{n}_{\mu m}(\theta)e^{\mathrm{j}\mu\chi}P_{s\mu n}(kA), \tag{2.34}$$

which relates the received probe signal, $w'(A,\chi,\theta,\phi)$ at the probe location (A,χ,θ,ϕ) to the unknown expansion coefficients T_{smn} of the AUT where $d^{n}_{\mu m}(\theta)$ are known as the rotation coefficients. In Eq. (2.34), (χ,θ,ϕ) are the Euler angles and the measurement radius is denoted by A. The probe polarization angles $\chi = (0^\circ, 90^\circ)$ are sufficient for first order probe correction. The probe response constants,

$$P_{s\mu n}(kA) = \frac{1}{2}\sum_{\sigma v} C^{sn(3)}_{\sigma\mu v}(kA)R^{p}_{\sigma\mu v}, \tag{2.35}$$

take into account the response of the probe to outgoing spherical waves from the AUT, where $C^{sn(3)}_{\sigma\mu\nu}(kA)$ are the translation coefficients and $R^{p}_{\sigma\mu\nu}$ are the receiving coefficients of the probe antenna. Dependence on the spatial coordinate is removed by means of the discrete Fourier transform (DFT) for the χ, ϕ and θ integrals to obtain

$$w^{n}_{\mu m}(A) = \nu \sum_{s=1}^{2} T_{smn} P_{s\mu n}(kA). \tag{2.36}$$

By choosing $\mu = \pm 1$ for first order probes, two equations

$$w^{n}_{1m}(A) = \nu T_{1mn} P_{11n}(kA) + \nu T_{2mn} P_{21n}(kA), \tag{2.37}$$

and

$$w^{n}_{-1m}(A) = \nu T_{1mn} P_{1,-1,n}(kA) + \nu T_{2mn} P_{2,-1,n}(kA), \tag{2.38}$$

can be solved for the expansion coefficients T_{1mn} and T_{2mn} of the AUT [Hansen, 1988]. First order probes are rotationally symmetric probes with the spherical mode index $\mu = \pm 1$ and thus with a simple sinusoidal azimuthal pattern. Also, for the regular rectangular open-ended waveguide probes which are not rotationally symmetric, this first order approximation can be made if the measurement distance is not too short [Laitinen et al., 2004, Newell and Gregson, 2013].

2.6 Arbitrary Measurement Geometries

There are certain NFFFT techniques that can be applied to arbitrary measurement geometries. These techniques are useful in situations in which the canonical measurement geometries previously described do not offer the best sampling approach. For example, it can be useful to have a measurement surface that is conformal to the measured device such as for in-situ antenna measurements whereby it can be challenging to mount the whole structure on a positioner [Geise et al., 2014]. Also, in order to reduce multiple interactions between the AUT and the probe in planar measurements, the measurement geometry in Fig. 2.7 has been suggested in [Qureshi et al., 2012a]. Similar concept is also applicable for cylindrical measurements. The scan plane is moved away from the AUT in the region where the measurement is more vulnerable to multiple interactions and the other regions are measured at a closer distance in order to keep a wide valid angle. The process of using the FFT in order to

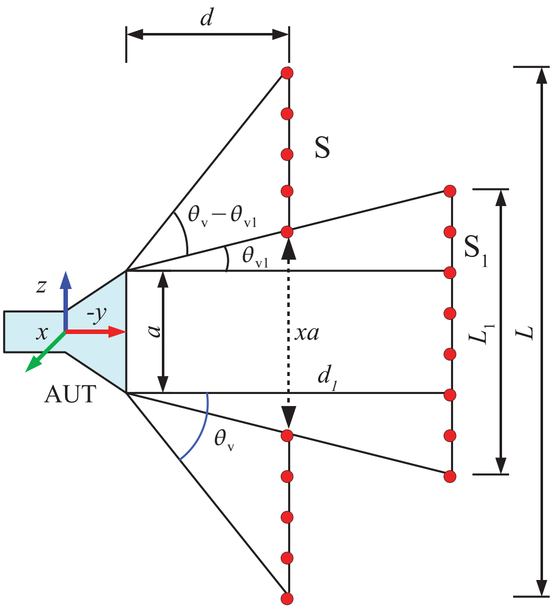

Figure 2.7: Measurement approach to reduce multiple reflections [Qureshi et al., 2012a].

obtain the far-field is, however, not applicable. Also, non-redundant sampling techniques, such as the one described in [Qureshi et al., 2013], can result in geometries that are not canonical. Techniques that can handle arbitrary measurement geometries are, therefore, invaluable in these scenarios. One of such techniques based on equivalent magnetic currents is discussed in [Blanch et al., 1995, Petre and Sarkar, 1992, Sarkar and Taaghol, 1999].

Fast Irregular Antenna Field Transformation Algorithm

The Fast Irregular Antenna Field Transformation Algorithm (FIAFTA) is an NFFFT algorithm applicable to measurements acquired on arbitrary measurement geometries. In this technique, the radiation behavior of the AUT is represented by a set of plane waves $(\bar{\boldsymbol{I}}-\hat{k}\hat{k})\cdot\tilde{\boldsymbol{J}}(\hat{k})$ propagating on the complete Ewald sphere. The measured signal at the point $\boldsymbol{r}_\mathrm{M}$,

$$U(\boldsymbol{r}_\mathrm{M}) = -\mathrm{j}\frac{\omega\mu}{4\pi}\sum_{\hat{k}} T_L(\hat{k},\boldsymbol{r}_\mathrm{M})\bar{\boldsymbol{P}}(\hat{k},\hat{r}_\mathrm{M})\cdot(\bar{\boldsymbol{I}}-\hat{k}\hat{k})\cdot\tilde{\boldsymbol{J}}(\hat{k}) \tag{2.39}$$

is then related to the AUT by translating the outgoing plane waves from the AUT to incident plane waves at the probe as depicted in Fig. 2.8 using the fast multipole method translation operator [Coifman et al., 1993]

$$T_L(\hat{k}, \boldsymbol{r}_\mathrm{M}) = -\frac{\mathrm{j}k}{4\pi} \sum_{l=0}^{L} (-\mathrm{j})^l (2l+1) h_l^{(2)}(kr_\mathrm{M}) P_l(\hat{k} \cdot \hat{r}_\mathrm{M}), \tag{2.40}$$

where $h_l^{(2)}$ and P_l are the spherical Hankel function of the second kind and the Legendre polynomials of degree l, respectively. The far-field pattern of the probe, $\bar{\boldsymbol{P}}(\hat{k}, \hat{r}_\mathrm{M})$, is used to weight the plane waves to fully compensate for the probe pattern influences. The multipole order L of the translation operator is chosen depending on the size of the AUT and of the probe antenna according to

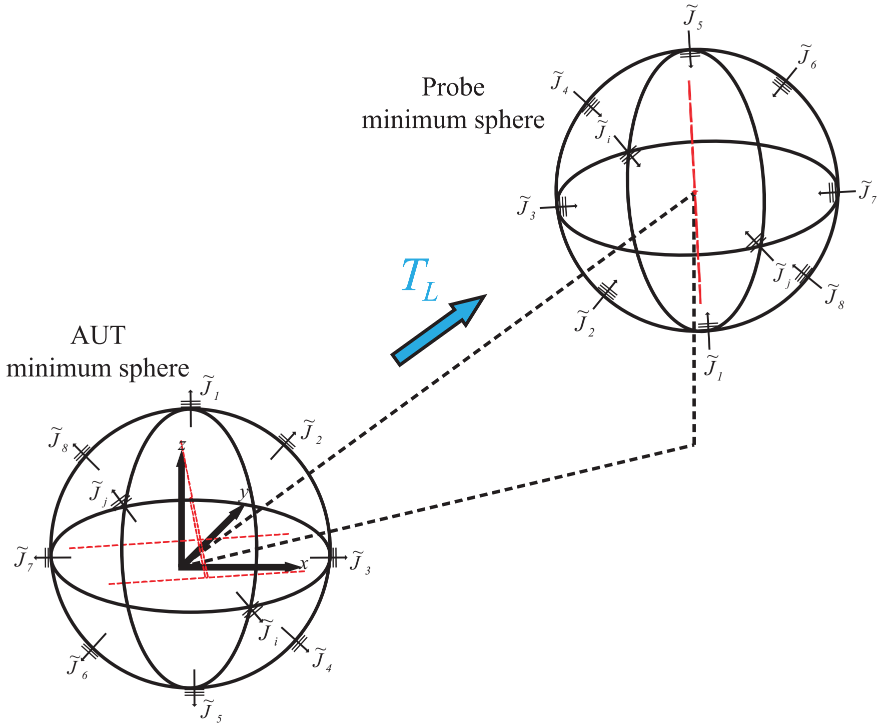

Figure 2.8: Translation of outgoing plane waves at the AUT to incident plane waves at the probe position.

$$L = \left\lceil \frac{kd}{2} + 1.8 d_o^{2/3} \left(\frac{kd}{2} \right)^{1/3} \right\rceil, \tag{2.41}$$

where d is the sum of the diameters of the minimum spheres enclosing the AUT and the probe antenna and d_o is the desired accuracy of the multipole expansion. It should also be noted that the minimum spheres of the AUT and the probe antenna must not overlap for the multipole representation to converge. The plane wave translation is performed from the AUT to all the measurement points and a linear system of equations

$$\boldsymbol{U'} = -\mathrm{j}\frac{\omega\mu}{4\pi}\mathbf{C}\cdot\tilde{\boldsymbol{J}}' \tag{2.42}$$

is formulated. The normal system of equations,

$$\mathbf{C}^H\cdot\boldsymbol{U'} = -\mathrm{j}\frac{\omega\mu}{4\pi}\mathbf{C}^H\mathbf{C}\cdot\tilde{\boldsymbol{J}}', \tag{2.43}$$

is solved iteratively using the generalized minimum residual solver (GMRES) [Saad and Schultz, 1986] to retrieve the plane wave coefficients of the AUT. Among other advantages, which will be mentioned later, the choice of GMRES is due to its applicability to a more general type of matrices as compared to other iterative methods such as the conjugate gradient (CG) [Hestenes and Stiefel, 1952] method. The CG method is only suitable for systems of equations involving symmetric, positive definite matrices. For these kinds of problems, the CG method converges to the global minimum of the quadratic form which coincides with the solution to the linear systems of equations. The algorithm, however, can break down when these conditions are not met [Saad and Schultz, 1986]. Certain methods, such as the biconjugate gradient method [Lanczos, 1952, Saad, 2003, Watson, 1974], try to generalize the CG method for non-symmetric matrices. However, certain conditions may still lead to the algorithm to breakdown [Freund and Nachtigal, 1991]. The relative residual of GMRES

$$\sigma = \frac{\|\mathbf{C}_k^H\mathbf{C}_k\tilde{\boldsymbol{J}}'_k - \mathbf{C}^H\boldsymbol{U'}\|}{\|\mathbf{C}^H\boldsymbol{U'}\|} \tag{2.44}$$

and the near-field residual

$$\varepsilon = \|\boldsymbol{U'} + \mathrm{j}\frac{\omega\mu}{4\pi}\mathbf{C}\cdot\tilde{\boldsymbol{J}}'\| \tag{2.45}$$

are used to determine the accuracy of the obtained plane wave coefficients obtained at the k-th iteration and to decide when to terminate the iterative solver. The coupling matrix

$$\mathbf{C} = \begin{pmatrix} C^1_\phi(k_{\phi 1}, k_{\theta 1}, \phi_1, \theta_1) & . \quad . \quad . & C^1_\theta(k_{\phi P}, k_{\theta Q}, \phi_1, \theta_1) \\ . & . & . \\ . & . & . \\ . & . & . \\ C^1_\phi(k_{\phi 1}, k_{\theta 1}, \phi_M, \theta_N) & . \quad . \quad . & C^1_\theta(k_{\phi P}, k_{\theta Q}, \phi_M, \theta_N) \\ C^1_\phi(k_{\phi 1}, k_{\theta 1}, \phi_1, \theta_1) & . \quad . \quad . & C^1_\theta(k_{\phi P}, k_{\theta Q}, \phi_1, \theta_1) \\ . & . & . \\ . & . & . \\ . & . & . \\ C^1_\phi(k_{\phi 1}, k_{\theta 1}, \phi_M, \theta_N) & . \quad . \quad . & C^1_\theta(k_{\phi P}, k_{\theta Q}, \phi_M, \theta_N) \end{pmatrix} \tag{2.46}$$

relates the plane wave coefficients of the AUT

$$\tilde{\boldsymbol{J}}' = \begin{pmatrix} \tilde{J}_\phi(k_{\phi 1}, k_{\theta 1}) \\ \tilde{J}_\theta(k_{\phi 1}, k_{\theta 1}) \\ . \\ . \\ . \\ \tilde{J}_\phi(k_{\phi P}, k_{\theta Q}) \\ \tilde{J}_\theta(k_{\phi P}, k_{\theta Q}) \end{pmatrix} \tag{2.47}$$

to the measured signal

$$\boldsymbol{U}' = \begin{pmatrix} U^1(\phi_1, \theta_1) \\ . \\ . \\ . \\ U^1(\phi_M, \theta_N) \\ U^2(\phi_1, \theta_1) \\ . \\ . \\ . \\ U^2(\phi_M, \theta_N) \end{pmatrix}, \tag{2.48}$$

where

$$C^{1,2}_{\phi,\theta}(k_{\phi p}, k_{\theta q}, \phi_m, \theta_n) = T_L(\hat{k}, \hat{r}_{\mathrm{M}}) W(k_{\theta_q}) P^{1,2}_{\phi,\theta}(k_{\phi p}, k_{\theta q}, \phi_m, \theta_n), \tag{2.49}$$

are the elements of the coupling matrix. In (2.49), $W(k_{\theta_q})$ are the weighting factors for integration over the sphere. The number of measurement points in the ϕ and θ directions are denoted by M and N, respectively, while the indices P and Q are the number of plane wave samples in the ϕ and θ directions, respectively. The algorithm can also be implemented in a multilevel manner similar to the multilevel fast multipole method whereby neighboring measurement points are grouped into boxes and the boxes are subsequently grouped into subboxes in a multilevel fashion [Schmidt and Eibert, 2009]. Plane wave translations

$$\tilde{\boldsymbol{J}}^{iN}_{N}(\hat{k}) = T_L(\hat{k}, \boldsymbol{r}_{\mathrm{box}}) \left(\bar{\boldsymbol{I}} - \hat{k}\hat{k}\right) \cdot \tilde{\boldsymbol{J}}(\hat{k}) \tag{2.50}$$

are performed from the AUT to the box center at the highest level as shown in Fig. 2.9. A series of anterpolations and disaggregations are applied in order to obtain the plane wave spectra

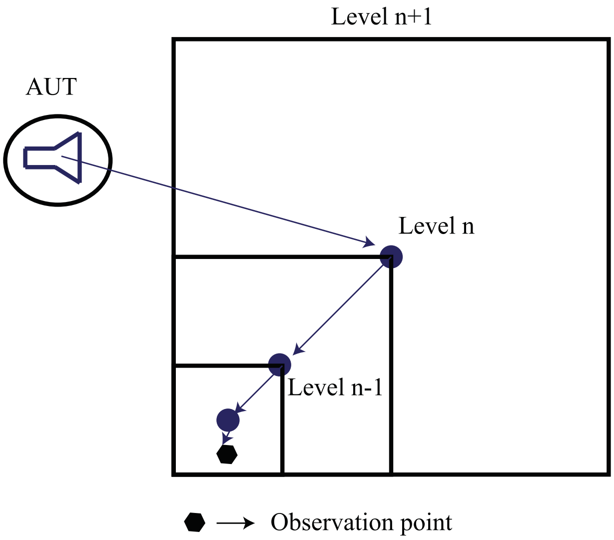

Figure 2.9: Multilevel grouping of measurement points.

$$\tilde{\boldsymbol{J}}^{iN}_{N}(\hat{k}) = \bar{\boldsymbol{D}}^{i_n}_{n}(\boldsymbol{k}, \boldsymbol{r}^{i_n}_{n}) \cdot \left(\bar{\boldsymbol{I}} - \hat{k}\hat{k}\right) \cdot \tilde{\boldsymbol{J}}^{i_{n+1}}_{n+1}(\hat{k}) \tag{2.51}$$

at the lowest level where

$$\bar{\boldsymbol{D}}^{i_n}_{n}(\boldsymbol{k}, \boldsymbol{r}^{i_n}_{n}) = \bar{\boldsymbol{V}}_n(\hat{k}) e^{-\mathrm{j}\boldsymbol{r}^{i_n}_{n} \cdot \boldsymbol{k}} \tag{2.52}$$

is the combined disaggregation and anterpolation operator. The anterpolation operator $\bar{\boldsymbol{V}}_n(\hat{k})$ is the adjoint operator of interpolation and it is used to reduce the spectral content at the lower levels of the multilevel structure. For points that are too close to the AUT, direct translations of outgoing plane waves can be carried out to the measurement points. Also, a subdivision of the AUT can be done to allow for a multilevel processing of groups of measurement points at short measurement distances [Schmidt and Eibert, 2012]. In this case, the AUT is subdivided into smaller sources regions and plane wave translations are performed from each of the sources regions to the measurement points.

Chapter 3

Survey of Existing Echo Suppression Techniques

Multipath propagation leads to erroneous near-field distribution for near-field antenna measurements carried out in non-anechoic environments. These errors are carried forward to the equivalent sources and subsequently to the far field if adequate steps are not taken to remove the multipath contributions. Semi-anechoic or outdoor measurements can become a necessity when the DUT is too large to move to an anechoic chamber. This is particularly true for in-situ antenna measurements where the AUT is mounted for instance on an airplane in order to observe how the antenna performs when mounted on the final system. Even for small test devices, the test frequency may not be ideal for the available measurement chamber because different absorber dimensions are more effective for different frequency ranges. Techniques that help in obtaining reliable measurement results from echoic data become invaluable in these circumstances. Echo suppression techniques usually involve either a dedicated echo-aware measurement procedure or post-processing of acquired data. Some techniques involve a combination of both. Dedicated measurement approaches involve, for example, the use of directive probe antennas [Hansen and Larsen, 1984, Slater, 1985]. The idea is to improve the signal to echo ratio by amplifying the line-of-sight (LOS) signals and by attenuating the echo signals at the time of measurement. The effect of the probe patterns is then corrected during the NFFFT process. This technique requires highly directive probe antennas and can result in multiple interactions between the AUT and the probe. Also, there are still individual measurement points which can be strongly corrupted by multipath signals. The dedicated measurement category includes hardware-gating techniques which exploit the time difference of arrival (TDOA) of the LOS signal and the multipath signal components to avoid the latter. This is achieved by gating out unwanted components by means of fast switching signal generators [Blech et al., 2010, Leibfritz et al., 2007a]. These techniques seek to improve the quality of the acquired data at the time of data acquisition by means of specialized hardware. The remaining techniques that are discussed in the following are those that do not depend only on hardware and can be categorized into two groups; techniques requiring broadband measurements or time domain techniques and those requiring a single frequency measurement.

3.1 Time Domain Techniques

The AUT and multipath signal components arrive at the probe with different time delays due to the different propagation paths of the signals. To exploit this time difference to separate the signals, a broadband measurement of the AUT is carried out and processed. There are two main techniques in this category; the fast Fourier transform (FFT) based method and the technique based on the matrix-pencil method (MPM). These techniques require a broadband measurement, which can considerably increase the measurement time, and they are only suitable for broadband AUTs and probes.

3.1.1 FFT-Based Method

Under free-space condition, the LOS is the only path between the AUT and the probe. The frequency response of the system is therefore characterized by a flat amplitude and linear phase responses. However, in the presence of multipath propagation, frequency-selective fading starts to appear. This is because, although the physical lengths traveled by the spectral components are the same, these distances represent different proportions of the wavelengths for different frequencies. The signals then combine either constructively or destructively at different degrees depending on the frequency. To obtain an echo free data from the echoic measurement facility, the $S_{21}(\phi, \theta)$ parameter is carried out in the frequency domain within a chosen bandwidth around a center frequency (f_o), with a frequency step of Δf. The bandwidth is chosen in relation to the reciprocal of the smallest expected time delay (δt) between the LOS signal and the first arriving multipath signal i.e. $BW = 1/\delta t$. In order to better distinguish the contributions in the time domain, a larger bandwidth $BW = 10/\delta t$ is suggested in Loredo et al. [2004]. The spacing Δf is chosen small enough to provide a good separation between the most important components to avoid aliasing. It is related to the time response length i.e. the time until the last reflection is received. In this way, the frequency response of the measurement environment can be modeled for each measurement point and by transforming to the time domain via the inverse fast Fourier transform (IFFT), the late arriving signals can then be identified and filtered out. The echo-free frequency response of the measurement facility can be obtained by transforming back to the frequency domain. A drawback of the FFT based technique is that it requires a relatively wide bandwidth in order to be effective [Loredo et al., 2004, 2009]. In [Moon et al., 2009], a method to reduce the required measurement bandwidth for the FFT based technique by generating virtual measurement data is described. Similar techniques based on equalizing for the multipath propagation channel are described in [Karthaus et al., 1998, Leather et al., 2004a,b, Newall and Rappaport, 1997].

3.1.2 Matrix-Pencil Method

The Matrix-Pencil Method (MPM) is a technique used to decompose a complex signal into a sum of complex exponentials [Sarkar and Pereira, 1995]. For the purpose of echo suppression in antenna measurements [Fourestie et al., 1999], the transmission coefficient S_{21} of the echoic system is measured at different frequencies between $f_o - BW/2$ and $f_o + BW/2$. The measurement bandwidth BW is the reciprocal of the TDOA between the LOS signal and the signal from the echo source. The broadband measurement sequence for each measurement point

$$S_{21}(n\Delta f) = \sum_{i=1}^{M} R_i e^{s_i n \Delta f} \tag{3.1}$$

is written as a sum of complex exponentials, with

$$s_i = \alpha_i + \mathrm{j}\beta_i, \tag{3.2}$$

where M and R_i represent the number of contributing paths to be considered and the complex amplitudes of those paths, respectively. The factors α_i represents the attenuation and β_i is related to the propagation time of the i-th path. Once the unknown coefficients R_i, α_i and β_i are found for the boresight azimuth angle using the MPM [Sarkar and Pereira, 1995], a single path (exponential) having the largest R_i is selected based on the assumption that the LOS signal will have the largest amplitude compared to the multipath signals. This leads to a solution in the form

$$S_{21}(f_o) = Re^{(\alpha+\mathrm{j}\beta)f}. \tag{3.3}$$

The same representation in (3.1) is applied for all the desired azimuth angles and by comparing β of the boresight azimuth angle to those of the candidate paths. The corresponding factors for the other azimuth angles are chosen based on the fact that the propagation time for the LOS signal should be the same for all the azimuth angles. Compared to the FFT based method, MPM requires a smaller measurement bandwidth for good accuracy. However, the performance degenerates as the number of echo sources increases [Leon Fernandez et al., 2009] and it depends on the assumption that the multipath signal level is lower than the LOS signal.

3.2 Single Frequency Techniques

Recent research efforts have been dedicated to multipath suppression using single frequency measurements [Black and Joy, 1995, Cano-Fácila et al., 2011, Direen et al., 2009, Gonzalez et al., 2011, Gregson et al., 2009, Hess, 2010, Hindman and Newell, 2005, Pogorzelski, 2009, 2010, Toivanen et al., 2010, Wittmann, 1990]. These techniques, unlike those explained in the previous section, require only a single frequency data for echo suppression. This broadens their applicability to include narrowband antennas along with the advantage that the measurement time is not considerably increased. As explained in Chapter 2, in order to obtain the far-field pattern from near-field measurements, equivalent sources are used to replace the AUT during the NFFFT process and the goal is to obtain these equivalent sources by solving an inverse problem. Echo suppression techniques seek to integrate echo suppression within the NFFFT process, for example, by obtaining additional equivalent sources for the echo contributions. Higher order modes may be considered for echo sources in modal NFFFT algorithms. Likewise, by using the knowledge of the echo locations in source reconstruction NFFFT techniques, additional sources can be obtained to represent echo sources at the considered locations. These techniques are discussed in the following.

3.2.1 Chamber Calibration Techniques

The techniques in this category require an initial measurement in the semi-anechoic or outdoor facility. The initial measurement usually involves known antennas and evaluates the scattering situation of the facility. The knowledge gained from the initial measurement is utilized during the main measurement to correct for the multipath effects. In the test zone field (TZF) compensation method [Black and Joy, 1995, Toivanen et al., 2010], the first task is to determine the TZF using a calibration antenna with known radiation characteristics through initial measurements. The calibration antenna is positioned in place of the AUT and the received signal

$$w = \sum_{s\mu n} R_{s\mu n} Q^{(4)}_{smn} \tag{3.4}$$

is expressed in terms of the receiving coefficients of the calibration antenna $R_{s\mu n}$ and the mode coefficients of the TZF $Q^{(4)}_{smn}$. The superscript index 4 indicate the coefficients for incoming waves. There are different sets of $R_{s\mu n}$ for each orientation of the calibration antenna such that $R_{s\mu n}$ is a function of (ϕ, θ, χ). The calibration antenna should be electrically larger than the measured AUT to ensure that the calibration antenna is sensitive to all spherical modes to be corrected. It can also be shifted away from the origin to increase its electrical size in the spherical mode expansion. A system of equations

$$\mathbf{R}\boldsymbol{q} = \boldsymbol{w} \tag{3.5}$$

is set up to obtain the TZF mode coefficients. $\mathbf{R}$ is a M-by-J matrix where M is the total number of orientations of the calibration antenna and J is the number of spherical modes. Also, $\boldsymbol{q}$ and $\boldsymbol{w}$ are column vectors containing the spherical wave coefficients of the TZF and the measured signal values, respectively. The second stage involves the usage of the obtained $Q^{(4)}_{smn}$ for field compensation. This is done in a similar way as the first stage. The AUT is used for the measurement and the measured signal

$$\boldsymbol{w} = \mathbf{Q}\boldsymbol{r} \tag{3.6}$$

is expressed in terms of the TZF coefficients previously obtained and the AUT receiving coefficients $\boldsymbol{r}$. In order to set-up Eq. (3.6), rotations are applied to the vector $\boldsymbol{q}$ for each of the M orientations of the AUT so that the dimension of matrix $\mathbf{Q}$ is M-by-J. In this way, the obtained AUT coefficients are free from the multipath contributions. Extended probe instrument calibration (EPIC) [Pogorzelski, 2009, 2010] is a similar technique requiring an initial measurement in the measurement room. Room scattering is estimated and included in the computed spherical wave coefficients of the probe. By correcting the AUT measurement for probe influences, the measurement is also corrected for echo contributions. Since both techniques require an initial estimation of the room scattering, the estimation has to be repeated whenever there is a change in the room configuration.

3.2.2 Modal Echo Suppression Techniques

As mentioned in Chapter 2, modal NFFFTs are utilized for canonical measurement geometries with a specific wave expansion taking advantage of the orthogonality of the employed set of eigenmodes. Planar, cylindrical, and spherical wave expansions are usually used for planar, cylindrical and spherical measurement geometries, respectively. These sets of waves take the role of equivalent sources for the purpose of NFFFT. The number of eigenmodes required to represent the AUT or the multipole order of the AUT is related to the size of the minimum sphere enclosing the AUT. However, in presence of multipath signals, the multipole order of the field will be different from the multipole order of the AUT with the former being higher. Modal echo suppression techniques utilize the a priori knowledge of the AUT multipole order in various ways for the purpose of removing multipath components.

Oversampling

The angular sample spacing in cylindrical and spherical near-field measurements is usually decided according to the size of the AUT. However, when sources are present outside the measurement volume, the multipole order of the field over the volume is higher than the multipole order of the AUT. This means that if the sampling criterion and cut-off mode for the mode expansion is determined from the size of the AUT, aliasing would occur. A simple method to reduce the introduced multipath error is to oversample the field and to include higher order modes in the expansion. This can be done, for example, according to the size of the measurement sphere for spherical measurements. The higher order modes are thereafter ignored for the purpose of evaluating the far-field pattern.

Mathematical Absorber Reflection Suppression (MARS)

When antennas are measured in traditional set-ups, such as planar, cylindrical, or spherical configurations, the AUT is placed in a way that it requires the minimum number of eigenmodes to represent its equivalent sources. This corresponds to placing the AUT during the measurement campaign at a location that minimizes the radius of the minimum sphere centered at the origin and enclosing the AUT. For spherical measurements, the most efficient placement of the AUT is such that it is centered at the origin of the measurement sphere. This is because the spherical wave expansion is usually done with respect to the origin of the coordinate system. The use of a minimum sphere not centered at the origin will require the ability to specify the origin of the spherical wave expansion for which efficient implementations have not been reported [Hansen, 1988]. In [Wood, 1977a,b], Wood presented a method capable of specifying the origin for a spherical wave expansion but it requires the measurement of both the electric and magnetic fields. Fig. 3.1 shows two possible placements of the AUT in a spherical measurement set-up. The AUT in Fig. 3.1(a) requires the minimum number of modes to represent it because it is located at the center of the coordinate system. In Fig. 3.1(b), however, the AUT is shifted away from the origin. This means that the minimum sphere enclosing the AUT is larger than in the first case even though the AUTs are identical. In the Mathematical Absorber Reflection Suppression (MARS) technique, the AUT is measured with a set-up as shown in Fig. 3.1(b) so that the effects of the echo contributions are more pronounced [Gregson et al., 2013]. The consequence of this shift away from the origin is also that the required number of spherical modes and the number of required field samples are increased in accordance with the radius of the minimum sphere in Fig. 3.1(b). Once these spherical modes are obtained, a phase shift is applied to the spherical modes according to how much the AUT is shifted from the origin. This corresponds to mathematically shifting the AUT back to the origin. The spherical modes after the phase shift with $n \leq N$ represent the AUT in Fig. 3.1(a). Once the modes are at the origin, the a priori knowledge about the required number of modes to represent the AUT is used to separate the modes belonging to the AUT ($n \leq N$) and those due to the multipath signals ($n > N$).

IsoFilter$^{\text{TM}}$

The idea of the IsoFilter$^{\text{TM}}$ is similar to MARS in exploiting the a priori knowledge about the electrical size of the AUT [Hess, 2011, Hess and McBride, 2010]. In this technique,

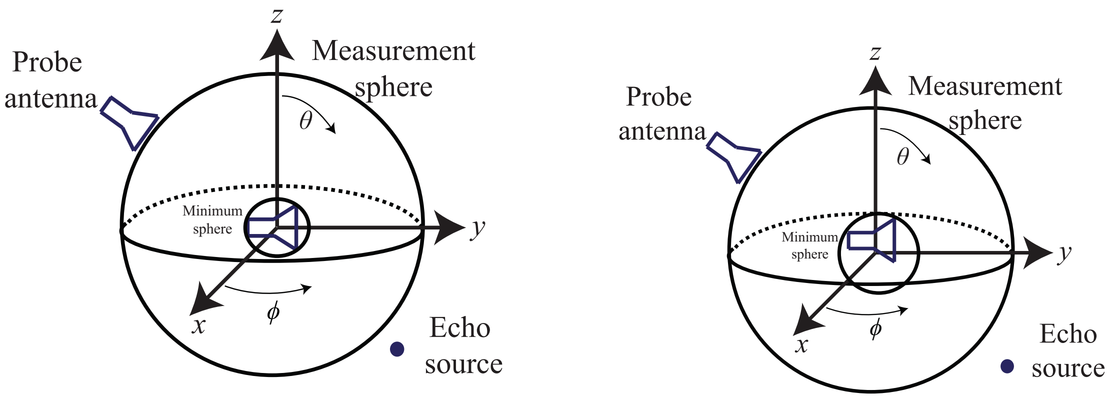

(a) Centered AUT (b) Offset AUT

Figure 3.1: Spherical measurement set-up including the minimum sphere with AUT located at the center of the coordinate system in (a) and the AUT shifted away from the origin in (b). The required number of spherical modes is minimum when the AUT is located at the origin of the measurement sphere.

it is required that the measurement sphere encompass all the echo sources. The sampling criterion is chosen by considering a minimum sphere that includes all contributing sources as demonstrated in Fig. 3.2. The increase in the size of the minimum sphere obviously mandates an oversampling of the near field. After the full set of spherical modes due to all the sources are obtained, the ones that belong to the AUT are retained. This is achieved by phase shifting the modes to the AUT phase center and discarding higher order modes $N > kr_{min}$ according to the size of the minimum sphere enclosing the AUT (r_{min}). Because of the need for the measurement sphere to encompass all radiating sources, the IsoFilter technique is more suited to filter contaminations that are due to the AUT mounting structures. Like MARS and other modal filtering techniques, the described technique is only applicable to measurements obtained on canonical measurement geometries and as such cannot take advantages provided by other measurement set-ups such as non-redundant sampling geometries.

3.2.3 Source Reconstruction Techniques

Echo suppression techniques in this category are used in conjunction with NFFFT algorithms that are based on source reconstruction. Source reconstruction in NFFFT algorithms assumes equivalent Huygen's sources over a fictitious surface over or enclosing the AUT to represent the AUTs radiation behavior. Once these currents are found, the radiation pat-

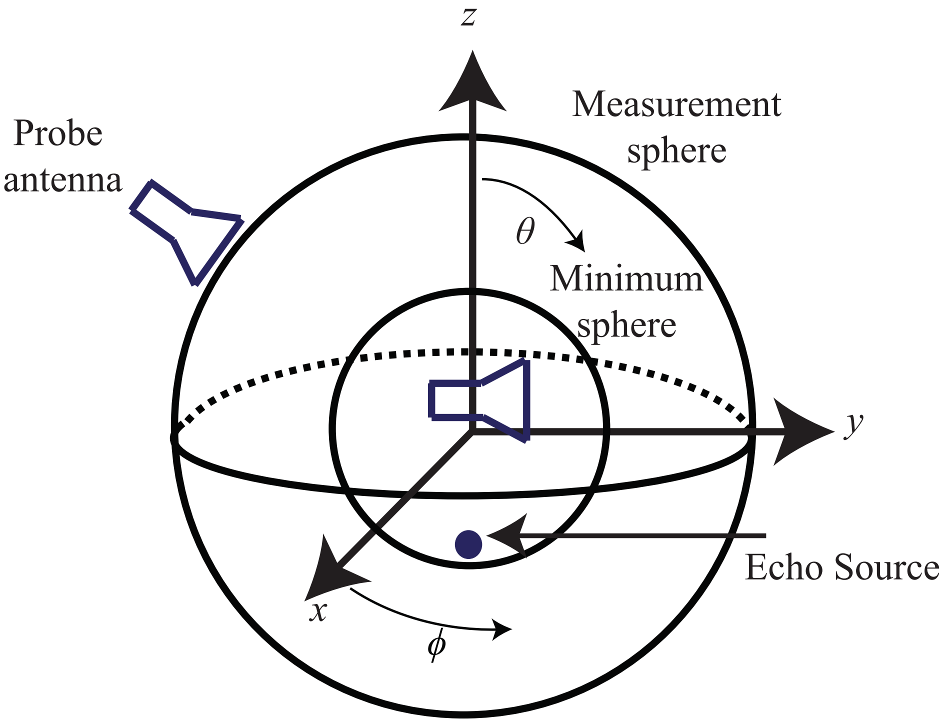

Figure 3.2: Spherical measurement geometry in the IsoFilter technique.

tern of the AUT or goal field can be computed at any distance in the near- or far-regions. For suppression of unwanted contributions, the fictitious surface over which the equivalent sources are obtained are extended to include the locations of the echo sources. Spatial filtering of the unwanted current sources is performed afterwards before computing the goal field. For example, when the equivalent current sources are obtained on a fictitious cylinder enclosing the AUT, the length of the cylinder is normally determined by the length of the AUT. However, in order to account for the echo contributions, the size of the cylinder is extended to include the known disturbers such as radiations from the feed cables and the AUT mounting structures, etc. The obtained current distribution is then truncated to spatially filter out the unwanted contributions [Araque Quijano et al., 2011, Quijano and Vecchi, 2010, Quijano et al., 2011]. In [Cano-Fácila et al., 2011], the plane wave spectrum is computed over an extended aperture according to the image theory to account for ground reflections. The part representing the AUT is retained for transformation into the far-field while the images representing reflections are removed from the plane wave spectrum. Other echo suppression techniques based on source reconstruction are presented in [Gonzalez et al., 2011] and [Cano et al., 2010]. However, motivations for new echo suppression technique still remains. Most of the mentioned echo supression techniques require, for instance, that the measurement samples be acquired on a canonical measurement geometry. Modern antenna measurements requirements are, however, tending towards conformal measurement surfaces with arbitrary probe orientations due to large test devices [Geise et al., 2014]. Also, because minimal knowledge of the measurement geometry in utilized in some of the techniques, the additional oversampling required to effectively filter the echo signals can be substantial.

Chapter 4

Scattering Centers Representation of Echoic Measurement Facilities

The plane wave based NFFFT algorithm was presented in Chapter 2. It involves a representation of the radiated AUT field by a set of outgoing plane waves in all directions taking the role of equivalent sources for the AUT. These outgoing plane waves are translated into incident plane waves at the probe by means of the FMM translation operator. This results in a linear system of equations

$$\boldsymbol{U'} = -\mathrm{j}\frac{\omega\mu}{4\pi}\mathbf{C}\cdot\tilde{\boldsymbol{J}}', \tag{4.1}$$

where $\tilde{\boldsymbol{J}}'$ contains the unknown plane wave coefficients of the AUT and $\mathbf{C}$ is the coupling matrix which includes the effects of plane wave translations and probe correction. The formulation in (4.1) is that of an inverse problem where one has a knowledge of some output, usually noisy, and a system model derived from the physical nature of the problem with an unknown input. Typically, the problem is ill-posed in terms of uniqueness and stability of the solution as it involves ill-conditioned system matrices. The reliability of the result depends on the accuracy of the model and the process from which the result is obtained. Several regularization techniques such as the Tikhonov regularization [Tikhonov and Arsenin, 1977] and the truncated singular value decomposition (TSVD) [Hansen, 1990, Xu, 1998] exist to improve the stability of ill-posed problems. However, due to the large size of the involved matrices in antenna measurements, iterative solutions are more favorable. The stability of the solution with the GMRES solver to random errors has been studied by Qureshi in [Qureshi et al., 2012b] for planar near-field measurements. The regularization properties of the GMRES [Calvetti et al., 2002a,b] helps to stabilize the solution when the model is accurate. In a multiple source scenario with additional sources other than the AUT, the model in Eq. (4.1) is essentially incomplete since the measured signal

$$\boldsymbol{U'} = \boldsymbol{U'}_{\mathrm{AUT}} + \boldsymbol{U'}_{\mathrm{echo}}, \tag{4.2}$$

is a superposition of the AUT signal $\boldsymbol{U'}_{\mathrm{AUT}}$ and signals from the echo sources $\boldsymbol{U'}_{\mathrm{echo}}$. The model can be improved by integrating these additional sources. This can be achieved by attributing the measured signal to the AUT and the echo sources during the problem formulation and obtaining the equivalent sources for each contributing source. Echo sources are treated as auxiliary sources or scattering centers contributing to the measured near-field data and their contributions are retrieved by integrating them into the NFFFT process. To this end, the formulation in Eq. (4.1) is done for all the contributing sources by assuming a set of out-going plane waves over the Ewald spheres related to the various scattering centers as an equivalent source for the echo sources. Plane wave translations are performed from each of these scattering centers to the measurement points as illustrated in Fig. 4.1. A new system of equations

$$\boldsymbol{U'} = -\mathrm{j}\frac{\omega\mu}{4\pi}\mathbf{C}_{\mathrm{AUT}} \cdot \tilde{\boldsymbol{J}}\boldsymbol{'} - \mathrm{j}\frac{\omega\mu}{4\pi}\sum_{i=1}^{N_{\mathrm{SC}}} \mathbf{C}_{\mathrm{SC}_i} \cdot \tilde{\boldsymbol{J}}\boldsymbol{'}_{\mathrm{SC}_i} \tag{4.3}$$

is formulated with more unknowns due to the new sources [Yinusa et al., 2011, 2012a,b]. The coupling matrix $\mathbf{C}_{\mathrm{SC}i}$ of the i-th scattering center includes the effect of plane wave translations and probe correction in the same way as the coupling matrix for the AUT-probe interaction is formulated. Eq. (4.3) is solved iteratively using GMRES to retrieve the contributions of the AUT and of the scattering centers. The computation of the translation operator in Eq. (2.40) generally requires the knowledge of the source and probe locations both of which are usually available for the AUT. This can also be easily evaluated for localized echo sources. However, echo locations may not be known exactly in certain situations such as in outdoor measurement set-ups or when the number of echo sources

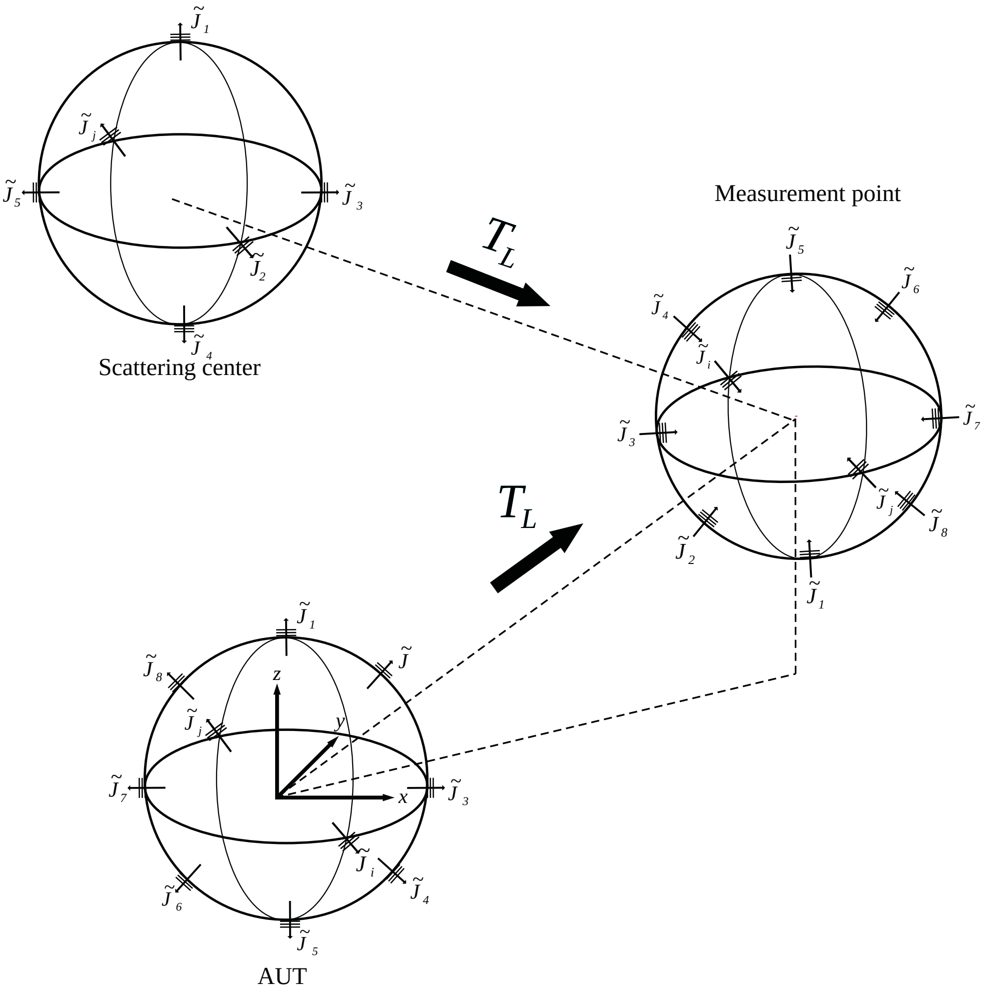

Figure 4.1: The translation operator converts out-going plane waves at the sources to incident plane waves at the probe antenna. Here, plane wave translations are performed for the AUT and for the additional plane waves assumed for the auxiliary sources. Copyright ©2013, IEEE.

are relatively large for manual input to be practical. The approach to scattering centers placements for echo sources, therefore, depends on the amount of information known about the echo sources. The different situations are discussed later.

4.1 Echo Data Generation

Throughout the remainder of this thesis, several echo suppression techniques will be presented and their effectiveness will be investigated by applying the techniques to echoic data. In practical antenna measurements, there are several other types of errors that can lead to unreliable measurements including, probe position uncertainty, probe alignment errors, etc. In order to study the effects of echoes in isolation from the other types of errors, synthetic data is relied upon in several examples in addition to actual measurement data. Synthetic data is obtained by modeling the AUT and probe by means of dipole distributions as described in [Schmidt et al., 2011].

Echo Scenario #1

A 3 GHz AUT is modeled with the dipole distribution shown in Fig. 4.2. The length and color of the dipoles represent the relative amplitude excitation and the phase, respectively, of the dipoles. The two layers of dipoles are separated by a distance of $\lambda/4$ and have a phase difference of 90° in order to concentrate the radiation in the -y direction. Echo sources are represented as point sources in a similar fashion by means of electric dipoles. The probe antenna is modeled similarly with 50 electric dipoles on two square planes each

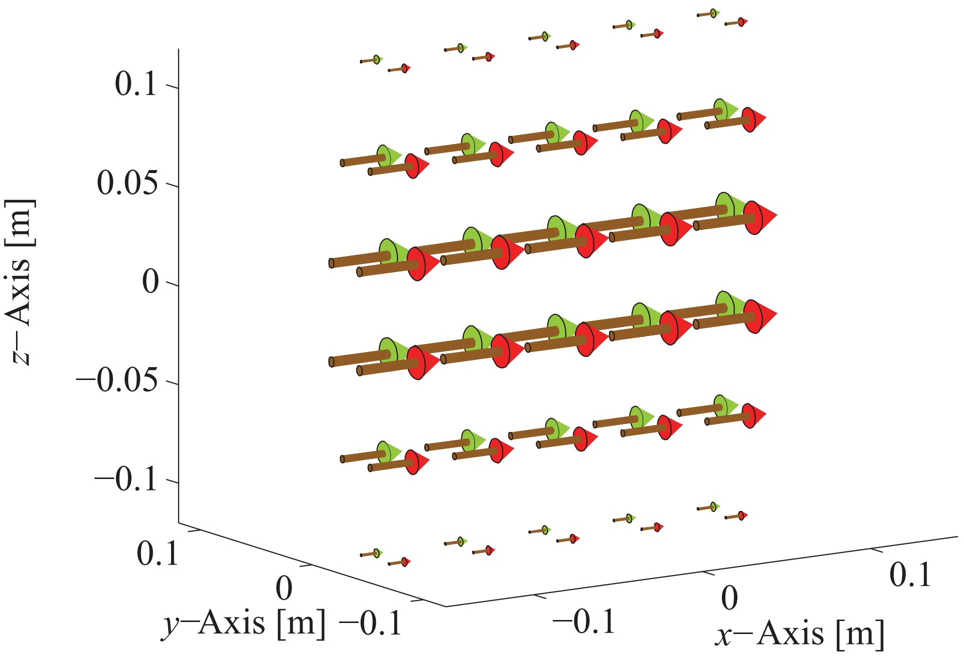

Figure 4.2: Electric dipole distribution used to model the 3 GHz AUT. The length and color of the dipoles represent the relative amplitude excitation and the phase, respectively.

measuring 8.64 cm x 8.64 cm with a symmetric amplitude excitation. The far-field pattern of the probe antenna is as shown in Fig. 4.3. The output signal at a measurement point $\boldsymbol{r}_\mathrm{M}$,

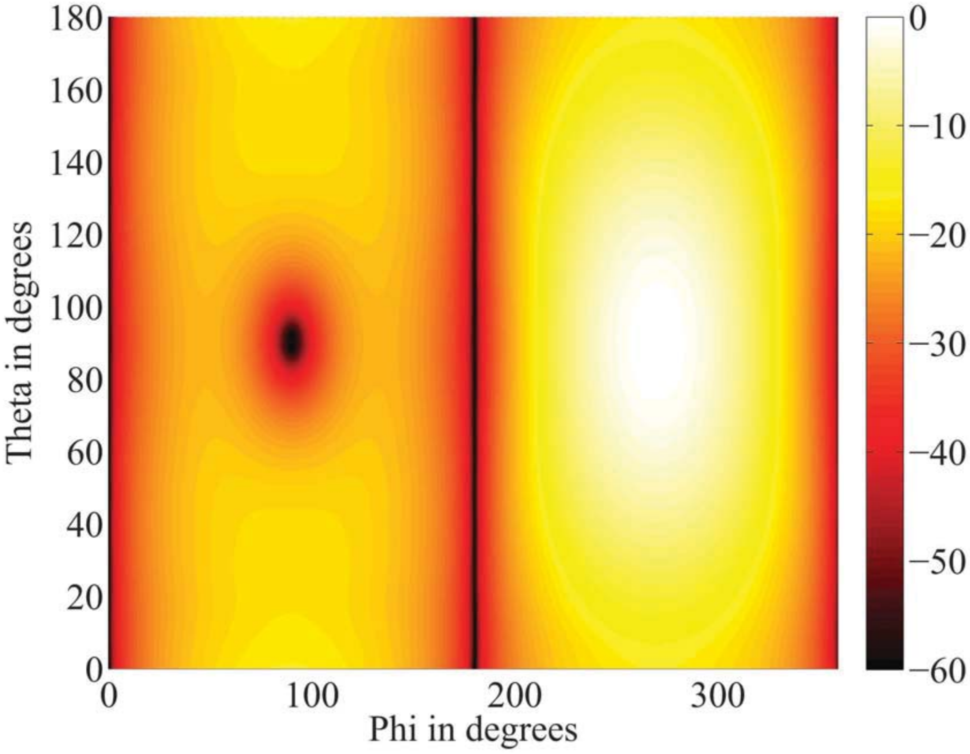

Figure 4.3: Normalized E_ϕ far-field pattern of the 3 GHz probe antenna in dB.

$$U(\boldsymbol{r}_\mathrm{M}) = \sum_{i=1}^{i_{probe}} E(\boldsymbol{r}_\mathrm{M} - \boldsymbol{r}_{p,i}) \cdot \boldsymbol{p}_i, \tag{4.4}$$

is generated by weighting and superimposing the electric field around the probe aperture at positions $\boldsymbol{r}_\mathrm{M} - \boldsymbol{r}_{p,i}$. The amplitude, phase and polarization of the i-th probe dipole are represented by $\boldsymbol{p}_i$ and

$$E(\boldsymbol{r}_\mathrm{M}) = -\mathrm{j}\frac{\omega\mu}{4\pi} \sum_{i=1}^{i_{AUT+Echo}} \left(\bar{\boldsymbol{I}} + \frac{1}{k^2}\nabla\nabla\right) \frac{e^{-\mathrm{j}k|\boldsymbol{r}_\mathrm{M} - \boldsymbol{r}_{d,i}|}}{|\boldsymbol{r}_\mathrm{M} - \boldsymbol{r}_{d,i}|} \cdot \boldsymbol{d}_i \tag{4.5}$$

denotes the electric field at the point $\boldsymbol{r}_\mathrm{M}$, obtained by superimposing the dyadic Greens function of free space at the desired location for all the source dipoles including the echo sources. In (4.5), $\bar{\boldsymbol{I}}$ is the unit dyad and $\boldsymbol{d}_i$ incorporates the amplitude, phase and polarization of the i-th source dipole. The minimum sphere enclosing the AUT modeled in Fig. 4.2 has a radius of 0.16 m. At a frequency of 3 GHz, this corresponds to a multipole order $N = 20$. Following Eq. (2.32), a maximum angular sample spacing of 8.7° is required along the ϕ and θ directions for the spherical measurement of this AUT. The measurement distance is set at 0.5 m. The plane wave based NFFFT is then applied to the near-field data without echo sources using a stopping tolerance of 10^{-7} for the GMRES solver. Fig. 4.4 shows the obtained far-field pattern of the AUT. This far-field pattern will also be used as a reference far-field for a subsequent evaluation of the presented techniques. In the next step, echo sources are introduced by means of electric dipoles. The echo sources in this example are three point sources located outside the measurement sphere as shown in Fig. 4.5. Signals arising due to echo sources are evaluated and superimposed on the AUT signal. The same sampling criterion as the non-echoic scenario is utilized. The plane wave based NFFFT algorithm is applied to the simulated echoic data with identical processing as the non-echoic case. The obtained far-field in this case is shown in Fig. 4.6 with the main cuts

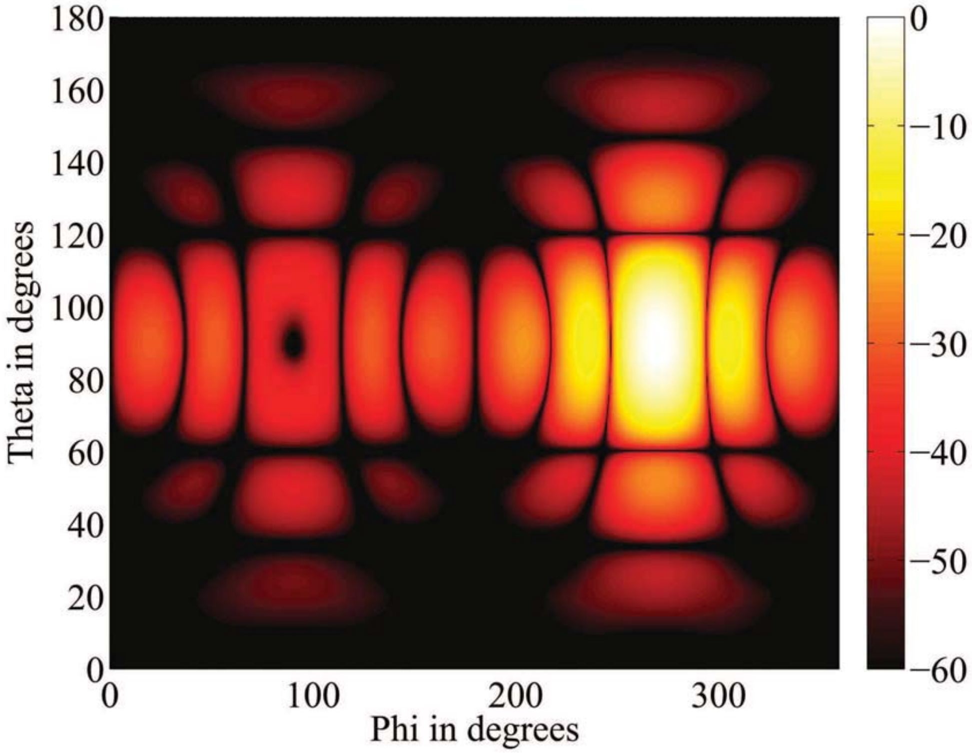

Figure 4.4: Normalized E_ϕ far-field pattern of the 3 GHz horn antenna in dB obtained from anechoic near-field data.

in Fig. 4.7.

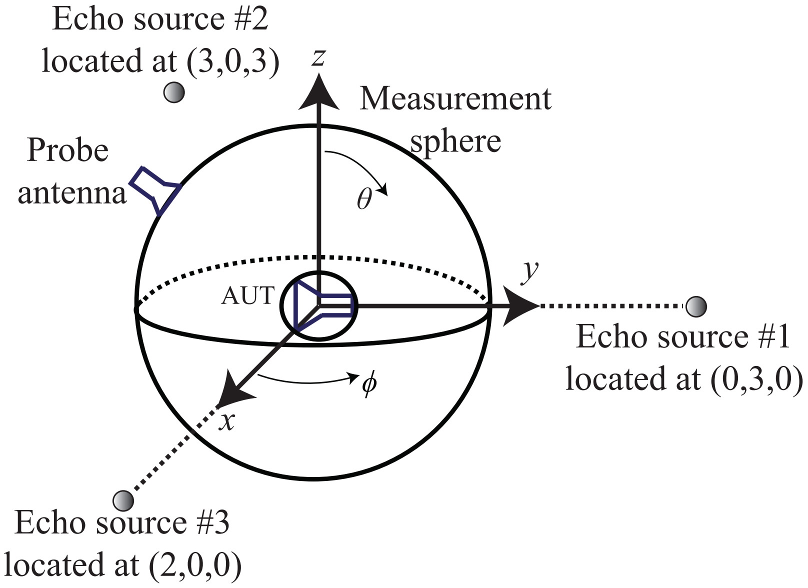

Figure 4.5: Scenario 1; Simulated echoic scenario with three echo sources. Echo source #1, #2 and #3 are located at coordinates (0,3,0), (3,0,3) and (3,0,0), respectively. Distances are in meters.

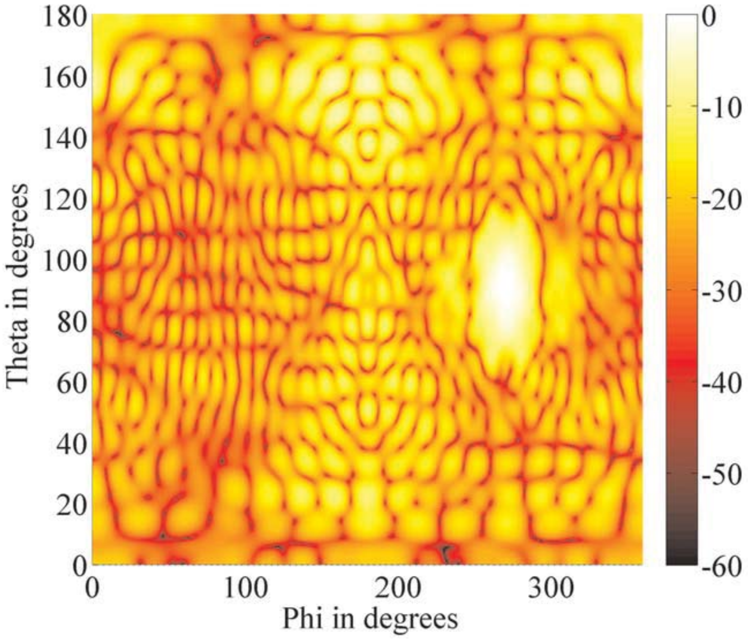

Figure 4.6: Normalized E_ϕ far-field pattern of the 3 GHz horn antenna in dB obtained from the echoic near-field data generated from the scenario in Fig. 4.5.

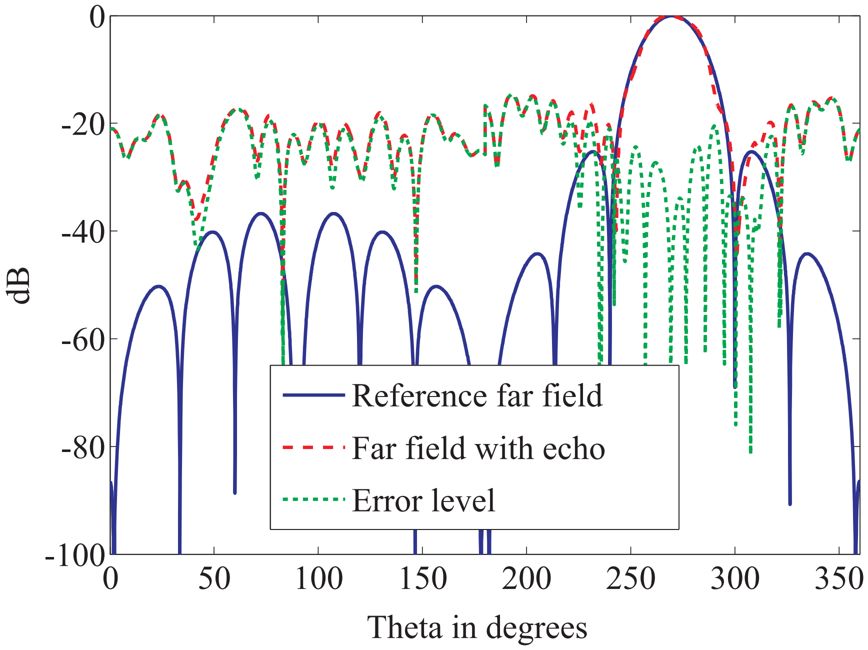

(a) E-plane pattern

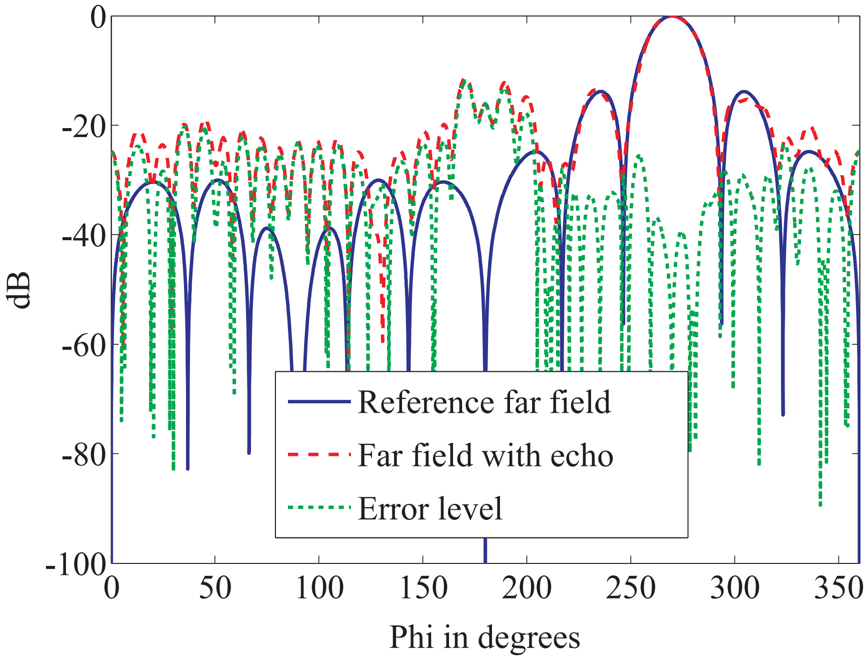

(b) H-plane pattern

Figure 4.7: Far-field main cuts obtained from Fig. 4.6.

It can be seen that the presence of echo introduced a significant difference between the reference far-field pattern and the obtained far-field pattern. The error level

$$EL = 20\log(\|\|\|E_{ref}(\phi,\theta)\| - \|E_{err}(\phi,\theta)\|\|\|) \tag{4.6}$$

is computed as the linear difference between the reference far-field E_{ref} and the obtained far-field E_{err} (both normalized to a maximum of 1) for a particular near-field data and NFFFT processing.

Echo Scenario #2

The second example involves planar measurement of a broadband double ridged horn antenna with a frequency range of between 1 GHz and 19 GHz shown in Fig. 4.8. An OEWG probe (WR90) was used to measure the near-field distribution over the measurement plane at frequencies of 8.2 GHz and 10.3 GHz in the measurement chamber where reflections are minimal. The size of the measurement plane was 1.2 m x 1.1 m and the measurement distance was 0.47 m. A sample spacing of 12 mm was chosen along both directions of the measurement plane corresponding to sample spacings of 0.33λ and 0.41λ at 8.2 GHz and 10.3 GHz, respectively. The sample spacings satisfy the Nyquist criterion of $\Delta_{x,y} \leq 0.50\lambda$ for both measurement frequencies. The obtained near-field distributions are shown in Fig. 4.11(a) and Fig. 4.12(a).

In the second stage, echoes were introduced to the measurements by means of metallic plates. The sets of near-field data were generated with two metal plates in the measurement chamber in order to introduce multipath contamination into the measurements as shown in the picture in Fig. 4.9. The schematic is shown in Fig. 4.10. The two metal plates were placed in the shown orientations in order to increase the influence of the multipath components within the valid angle. Near-field distributions obtained in presence of the metal plates are shown in Fig. 4.11(b) and Fig. 4.12(b). The ripples in the measured near-field data due to the presence of the metal plates are clearly visible. These near-field errors are carried over to the far field. The extent of the far-field errors depends on the employed NFFFT algorithm and on the post-processing efforts to remove the echo contributions.
The far-field pattern of the AUT was obtained from the non-echoic and echoic near-field data generated in this example using the classical FFT based technique. The results are shown in Fig. 4.13 and Fig. 4.14 for measurement frequencies of 8.2 GHz and 10.3 GHz, respectively. The effect of reflections from the metal plates is clearly visible in the H-plane

Figure 4.8: Double Ridged Broadband Horn Antenna DRH18 used as AUT [RF Spin, 2014].

Figure 4.9: Two metal plates were introduced to the chamber in order to generate multipath contamination into the measurement data.

far-field pattern of the AUT for both frequencies. The FFT based algorithm is particularly prone to multipath errors since it does not incorporate much a priori information about the

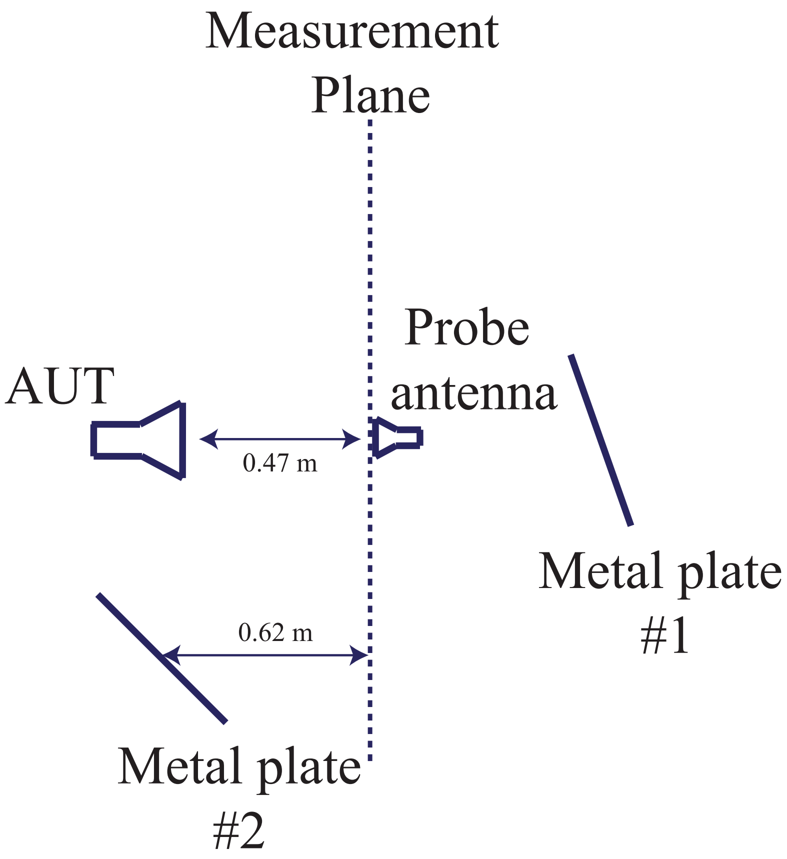

Figure 4.10: Schematic of echoic scenario.

AUT into the the NFFFT process. The plane wave spectrum (PWS) is simply obtained from the measurement data without any consideration to the size of the AUT.

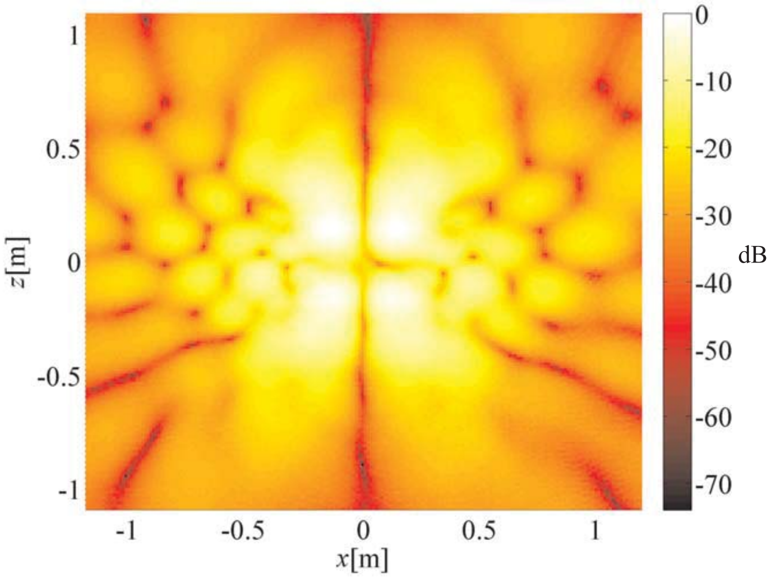

(a) Without metal plates

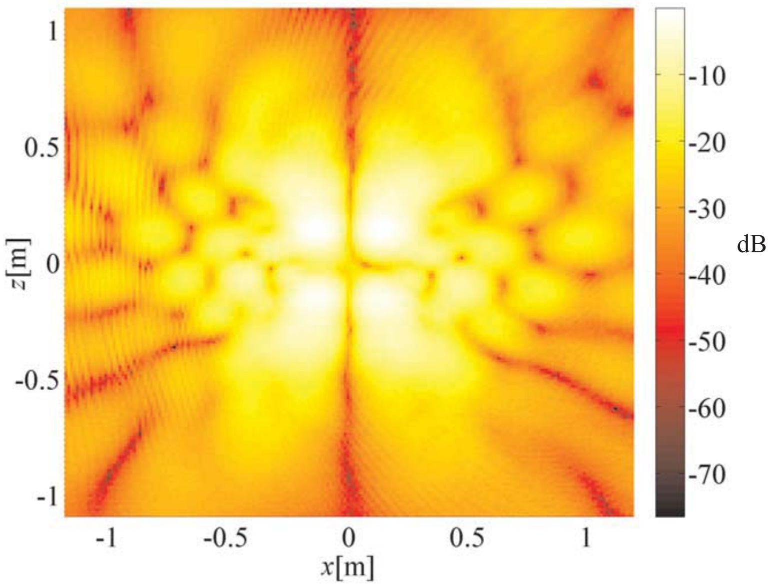

(b) With metal plates

Figure 4.11: Near field distribution of the broadband horn antenna at 10.3 GHz for the described planar measurement set-up, pol1.

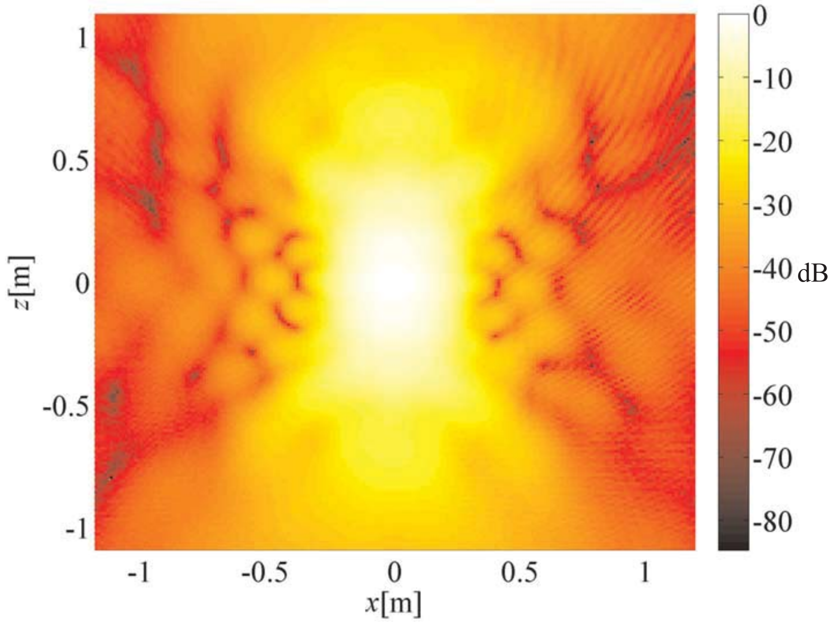

(a) Without metal plates

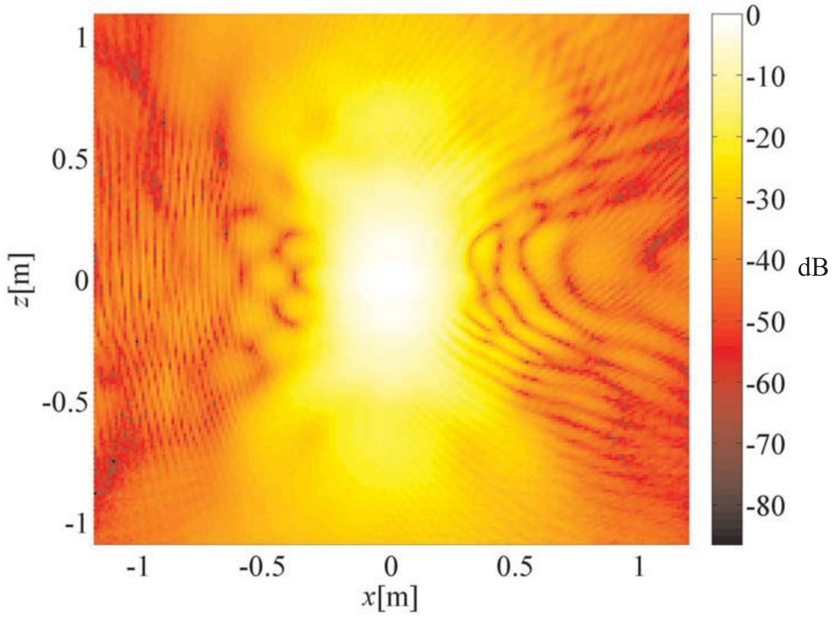

(b) With metal plates

Figure 4.12: Near-field distribution of the broadband horn antenna at 10.3 GHz for the described planar measurement set-up, pol2.

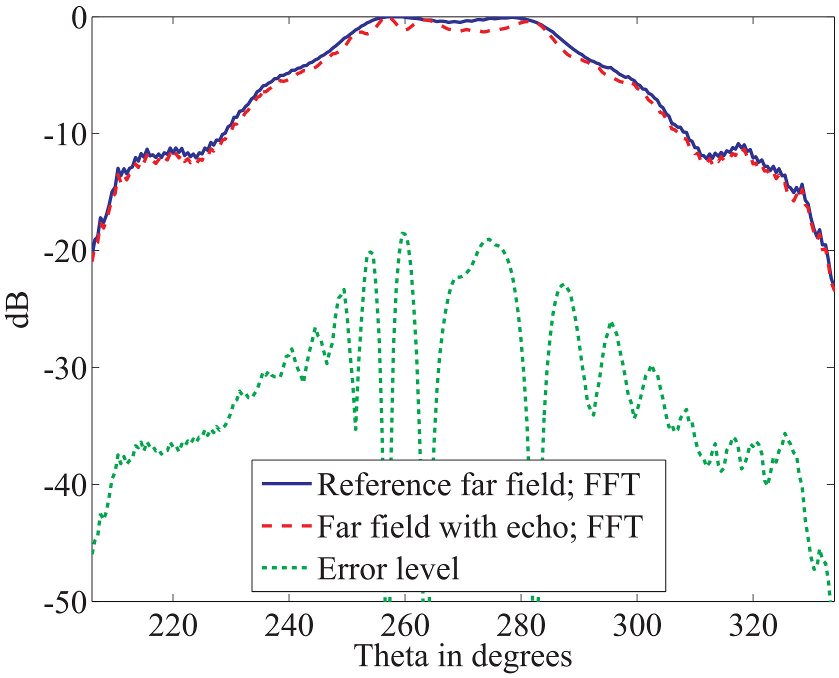

(a) E-Plane

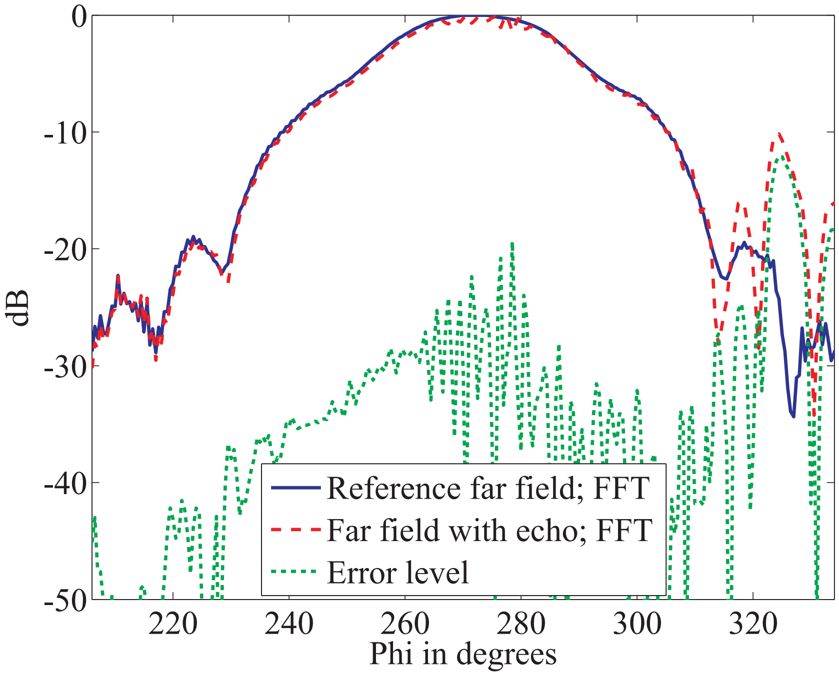

(b) H-Plane

Figure 4.13: Obtained E_θ far-field pattern cuts at 8.2 GHz with and without metal plates using the classical FFT based algorithm for the planar near-field measurement example within the valid angle. The effect of reflections from the metal plates is clearly visible in the H-plane far-field pattern of the AUT.

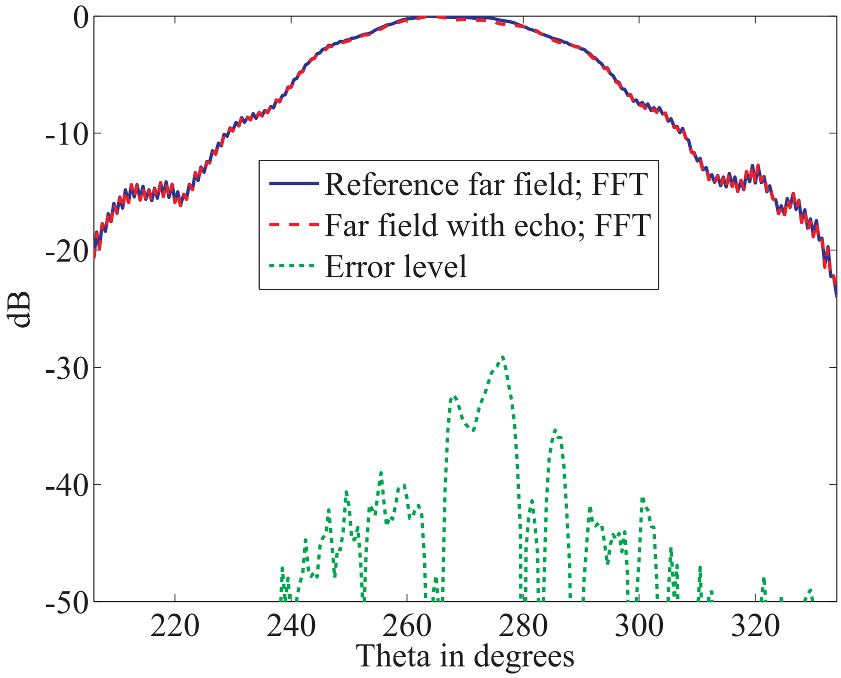

(a) E-Plane

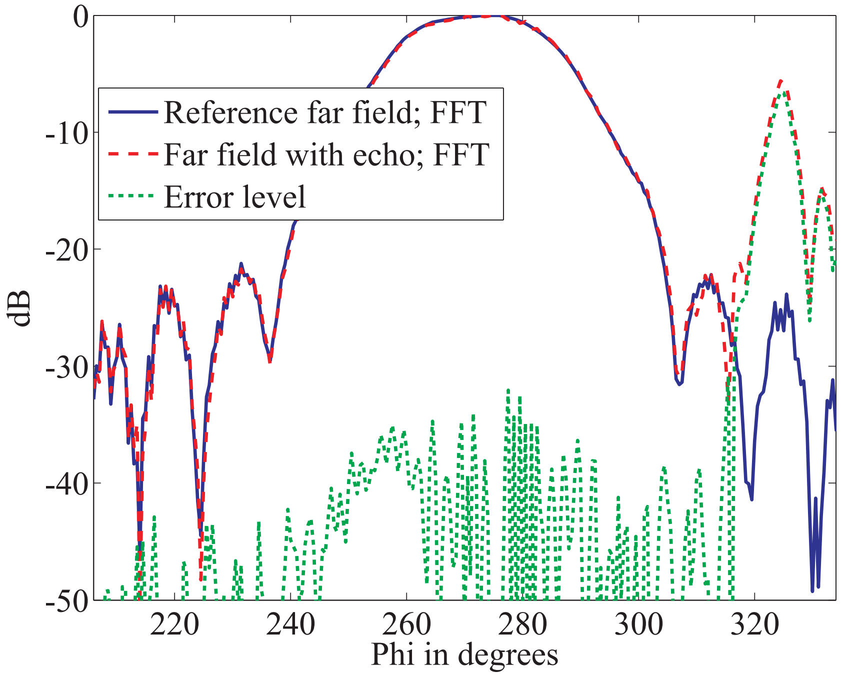

(b) H-Plane

Figure 4.14: Obtained E_θ far-field pattern cuts at 10.3 GHz with and without metal plates using the classical FFT based algorithm for the planar near-field measurement example within the valid angle. The effect of reflections from the metal plates is clearly visible in the H-plane far-field pattern of the AUT.

4.2 Scattering Centers Representation of Localized Echo Sources

In order to separate multipath signals from direct AUT signals, auxiliary sources are assumed for the contributing echo sources. Plane wave translations are thereafter performed from the AUT location and locations of the assumed sources to the measurement points. Depending upon the amount of a priori knowledge about the echo sources, different approaches to the placement of the auxiliary sources are possible. For instance, in a semi-anechoic chamber, there maybe few echo sources whose sizes and locations can be assumed to be known. However, in an outdoor environment, the number of potential echo sources may be too high for a manual input of echo locations. When echo locations are known, the translation operator from the echo sources to the measurement points can simply be computed by replacing the echo sources with auxiliary sources in the same locations. The multipole orders of the translation operator required between the echo sources and the probes depend on the size of the concerned echo source and the size of the probe antenna. Plane wave translation is then performed from the AUT and scattering centers to the measurement points which leads to an improved model of the actual interactions that led to the measured data.

4.2.1 Spherical Measurement with Fixed AUT

As an example, the three echo sources in Fig. 4.5 are represented with scattering centers. Since the echo sources are point sources, a single, small scattering center is employed to model each of the echo sources resulting in three scattering centers each with a multipole order of 4 compared to the AUT multipole order of 20. At a frequency of 3 GHz and an accuracy of 10^{-3} for the translation operator, the total number of plane waves used to represent the radiation behavior of the AUT with the dipole distribution in Fig. 4.2 is 1600 for both polarizations. The echo sources have a total number of 300 plane wave samples. It should be noted that the number of plane wave samples needed to represent an echo source does not depend on the strength of the echo but on the electrical size of the involved disturber. The GMRES solver was stopped at the 100th iteration as it did not converge to the previous 10^{-7} relative residual. The obtained far field with this representation of the echo sources as localized scattering centers is shown in Fig. 4.15 with the far-field main cuts shown in Fig. 4.16. The influence of the echo suppression effort can be seen when compared to the results in Fig. 4.6 and Fig. 4.7 as the maximum error level is reduced from about -20 dB to about -40 dB in the E_ϕ main axis.

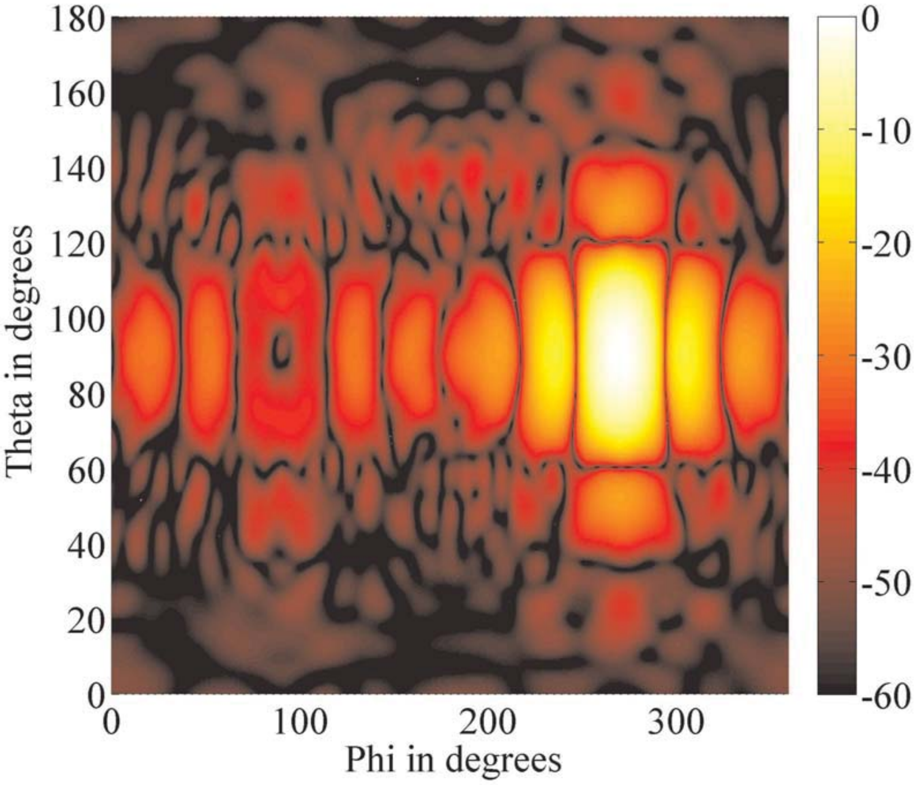

Figure 4.15: Normalized E_ϕ far-field pattern cuts of the 3 GHz horn antenna in dB obtained from the echoic near-field data generated from the scenario in Fig. 4.5. The echo sources are included in the NFFFT process by means of scattering centers at the same locations as the echo sources.

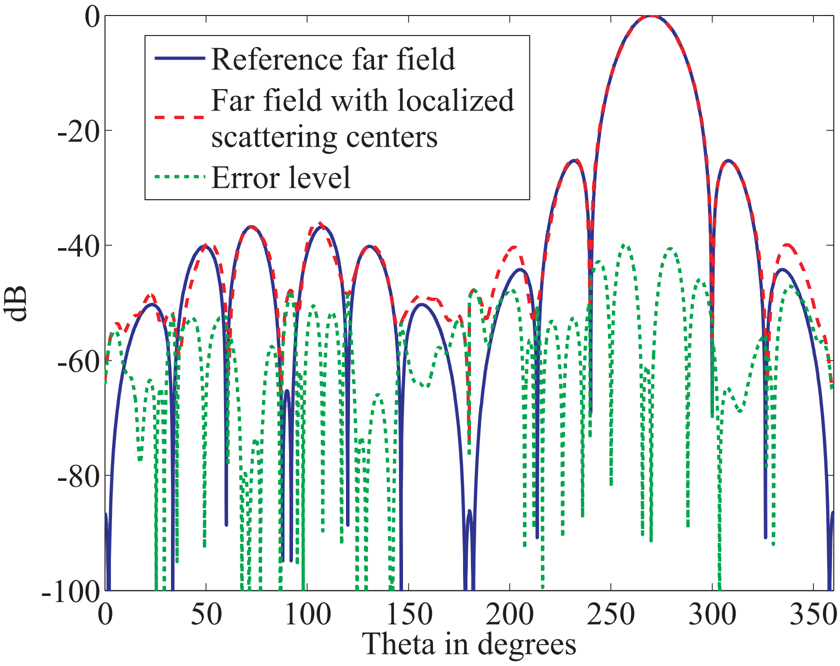

(a) E-plane pattern

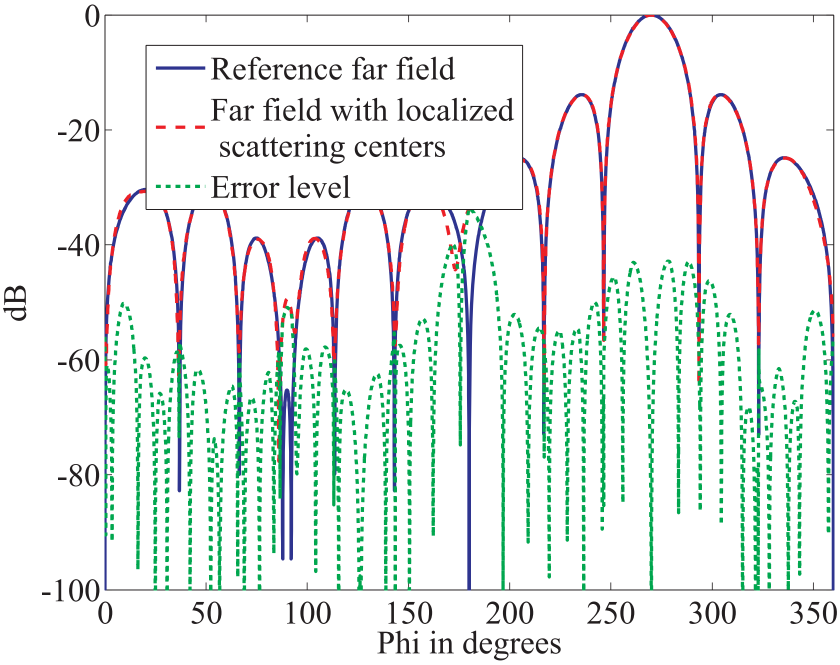

(b) H-plane pattern

Figure 4.16: Main cuts for the pattern in Fig. 4.15.

4.2.2 Cylindrical Measurement with Rotating AUT

In a typical cylindrical measurement set-up, the AUT is mounted on a positioner capable of rotating around the azimuth and the probe scans a single line vertically for each azimuthal step of the AUT. This means that the generated multipath signal resulting from a scatterer differs depending on the azimuth position of the AUT. A single scattering center in this case is not suitable to represent a single scatterer because of the change in the scattering situation when the AUT steps in Azimuth. Scattering centers representation is done in this case with many auxiliary sources, one for each of the azimuth positions. All the scattering centers are located at the position of the intended scatterer. The number of scattering centers needed to represent a single source is, therefore, equal to the number AUT angular steps in azimuth. Plane wave translations are performed from each scattering center to the corresponding measurement points sharing the same azimuth angle and no coupling is assumed between the scattering center with the remaining measurement points. The system of equations with these replicated scattering centers looks as shown in Fig. 4.17 for a cylindrical measurement set-up with four azimuthal steps. The vectors $\boldsymbol{U}_1$ to $\boldsymbol{U}_4$ are the groups of measurement points on same azimuth angle. As an example, cylindrical measurement data was generated for the 3 GHz AUT shown in Fig. 4.2 with three echo sources as shown in Fig 4.18. The AUT was rotated about its axis about the azimuth angle and the induced current on the echo sources are computed for each of the AUT orientations. Once the induced current on the echo sources are obtained, the probe scans the measurement points

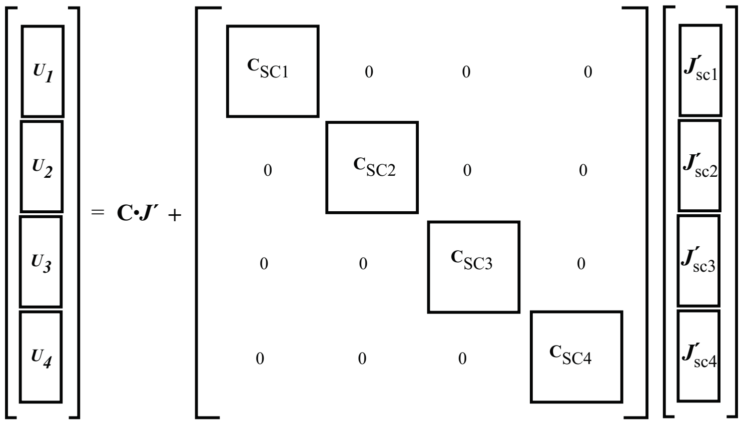

Figure 4.17: Representation of a single echo source in a cylindrical measurement geometry with rotating AUT on four azimuth points.

vertically. This procedure is repeated for all azimuth steps of the AUT in order to generate the measurement data over the measurement cylinder. The near-field data was obtained with an angular sample spacing of 8.7° and a vertical sample spacing of $\lambda/2$. The height of the measurement cylinder was 1.6 m and the measurement distance was 0.5 m resulting in a valid θ angle of about 55°. The echo sources were represented by means of replicated scattering centers as explained earlier. Plane wave translations are performed from the scattering centers to the measurement points sharing the same azimuth and all other couplings are assumed to be zero for the scattering center. The location of the echo sources are assumed to be known and since the assumed echo sources are point sources, the number of plane waves assumed for the echo sources are relatively small. This representation increases the unknown plane wave coefficients of the echo sources by a factor equaling the number of azimuth steps of the AUT. The results are shown in Fig. 4.19 and Fig. 4.20. It can be observed that representing the echo source by means of auxiliary sources resulted in a reduction in the error level of the obtained far-field pattern. The achieved echo suppression is not as good as the case with a fixed AUT because only the measurement points sharing the same azimuth angle are utilized for the scattering centers. In the previous example with a fixed AUT, all the measurement points were used to set up the system of equations for both the AUT and for the auxiliary sources.

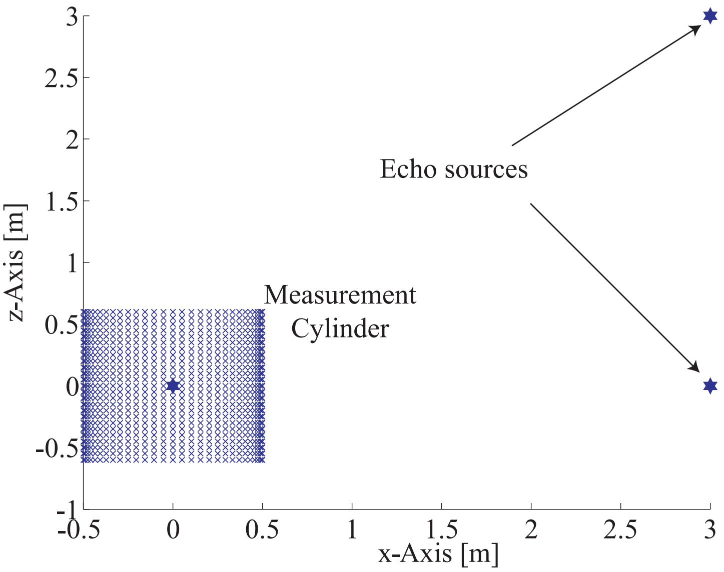

Figure 4.18: Representation of a single echo source in a cylindrical measurement geometry with rotating AUT on four azimuth points.

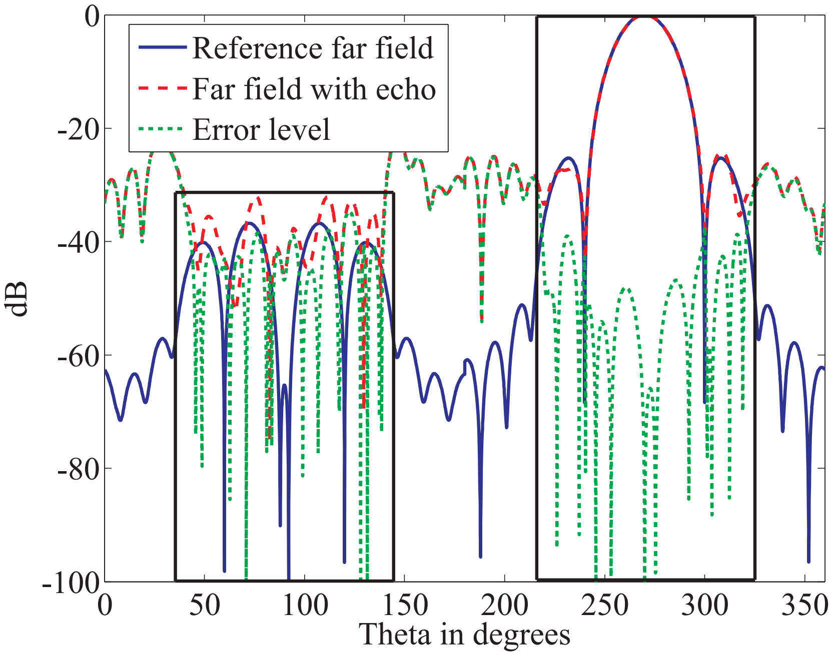

(a) E-plane pattern

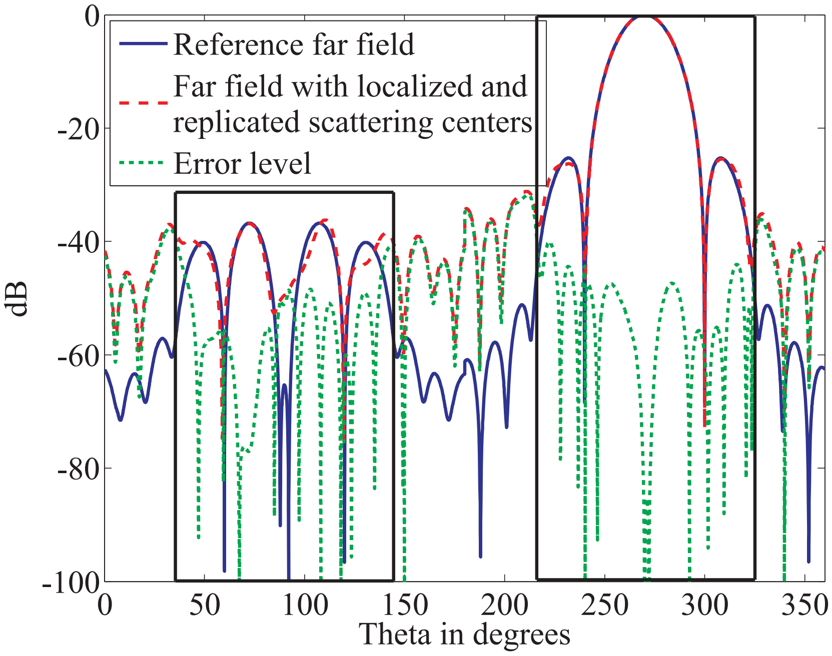

(b) H-plane pattern

Figure 4.19: Main cuts for cylindrical. The rectangular boxes demarcate the valid angles.

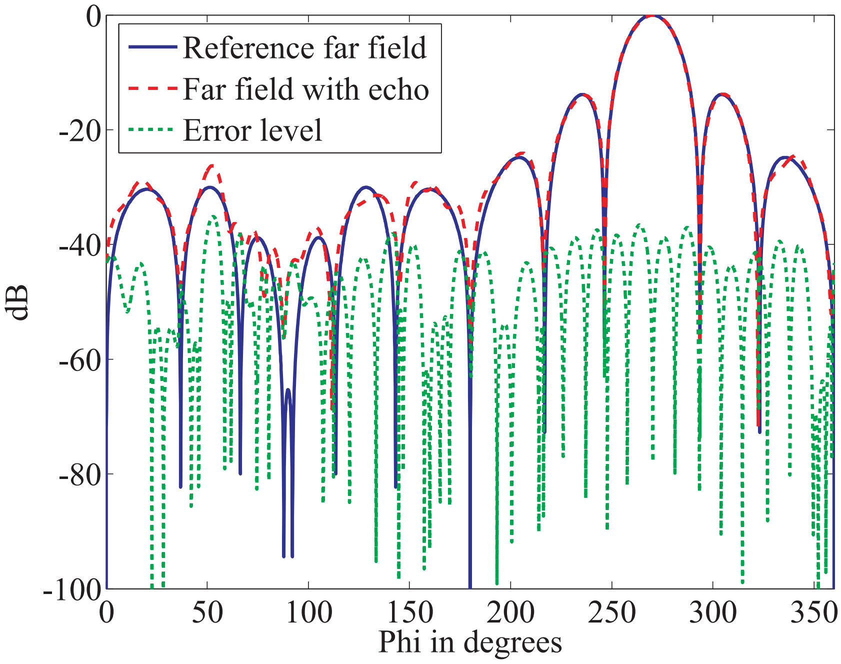

(a) E-plane pattern

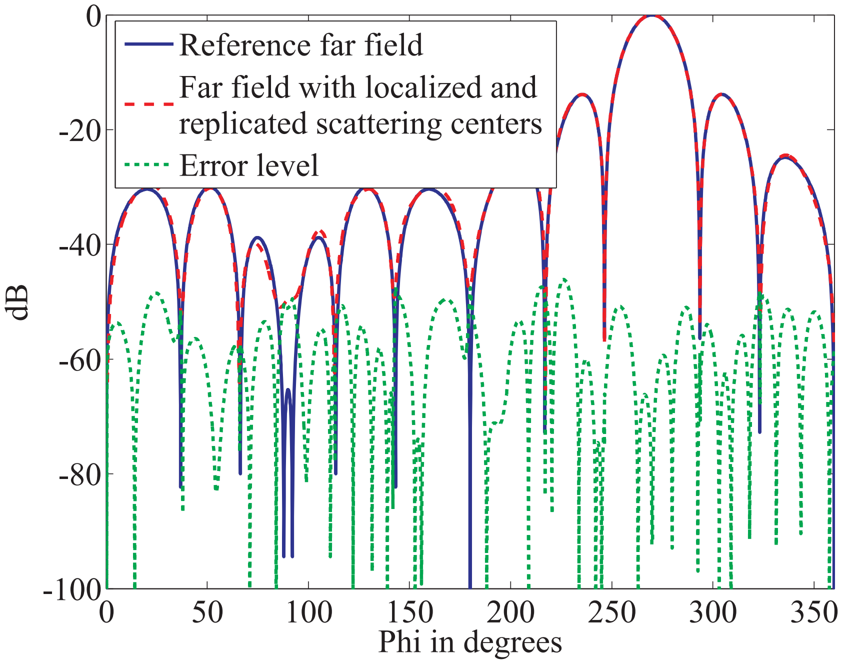

(b) H-plane pattern

Figure 4.20: Main cuts for cylindrical.

Result for DRH18 at 8.2 GHz

The effects of multipath contributions on the obtained far-field pattern of the AUT shown in the measurement set-up in Fig. 4.9 can be clearly seen in Fig. 4.13. The error level varied from about -50 dB to -10 dB. The direct AUT signals were contaminated by multipath signals arising from the metal plates. In that result, the far-field pattern was obtained using the classical FFT technique. In the FFT technique, the far-field pattern of the AUT is obtained directly from the measurement data without utilizing any a priori information about the AUT. In this section, the plane wave based NFFFT algorithm was utilized first to observe its performance in the presence of echo contributions and to further improve the performance by integrating the echo sources within the NFFFT process. Unlike the FFT based algorithm, the plane wave based NFFFT algorithm shows a better performance in presence of echo signals due to its inherent spatial filtering capability. Sources are assumed within the minimum sphere enclosing the AUT as demonstrated in Fig. 4.21. This allows the algorithm to utilize the size and location of the AUT and to automatically exclude sources that are outside the minimum sphere. Once the equivalent sources within the minimum sphere are obtained, the far-field pattern of the AUT can be computed using those equivalent sources. The reference far-field pattern of the DRH18 antenna obtained by the plane wave based NFFFT algorithm from measurements without the metal plates is shown in

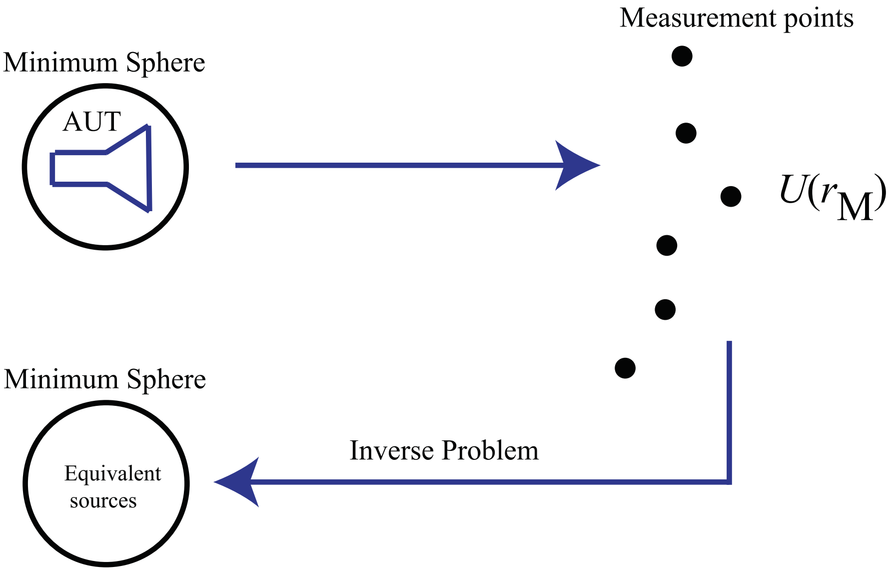

Figure 4.21: Near-field data is related to equivalent sources with-in the minimum sphere enclosing the AUT.

Fig. 4.22. The far-field pattern is also evaluated from the echoic data obtained in presence of the metal plates through the same algorithm and the result is shown in Fig. 4.23. In order to compensate for the effect of the metal plates in Fig. 4.9, the second metal plate which produces the significant portion of the multipath components is represented with scattering centers. The scattering centers are placed on a discretized surface covering the metal plate. A total number of 144 small scattering centers each with a multipole order of 3 were employed to model the metal plate. The plane wave coefficients attributed to both the AUT and the scattering centers were obtained from the inverse problem solution. Once the solution was obtained, the far field with echo suppression was computed with the plane wave coefficients of the AUT alone. The obtained far-field pattern with the metal plates represented by means of auxiliary sources is shown in Fig. 4.24. A closer observation of the results can be achieved through the main pattern cuts in Fig. 4.25 and Fig. 4.26. Two observations can

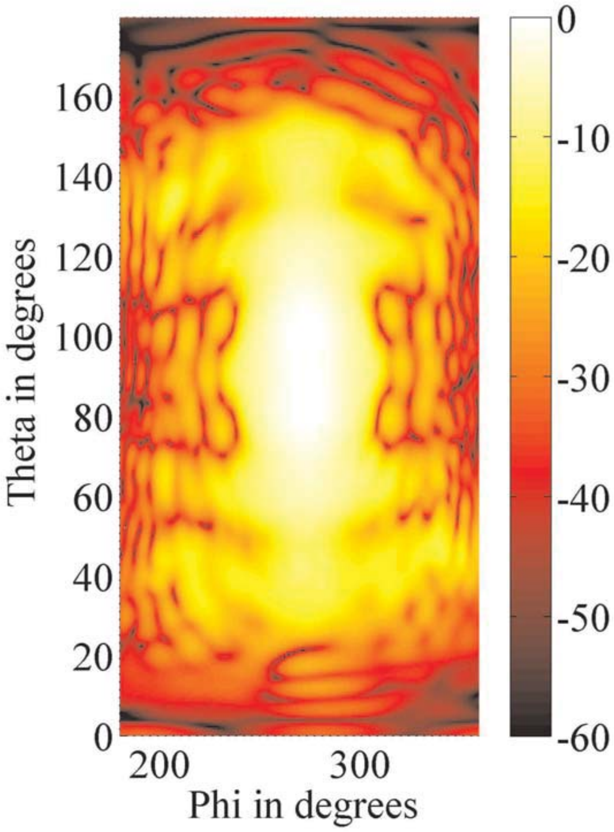

Figure 4.22: Normalized E_ϕ far-field pattern of the DRH18 broadband antenna at 8.2 GHz in dB obtained without the metal plates.

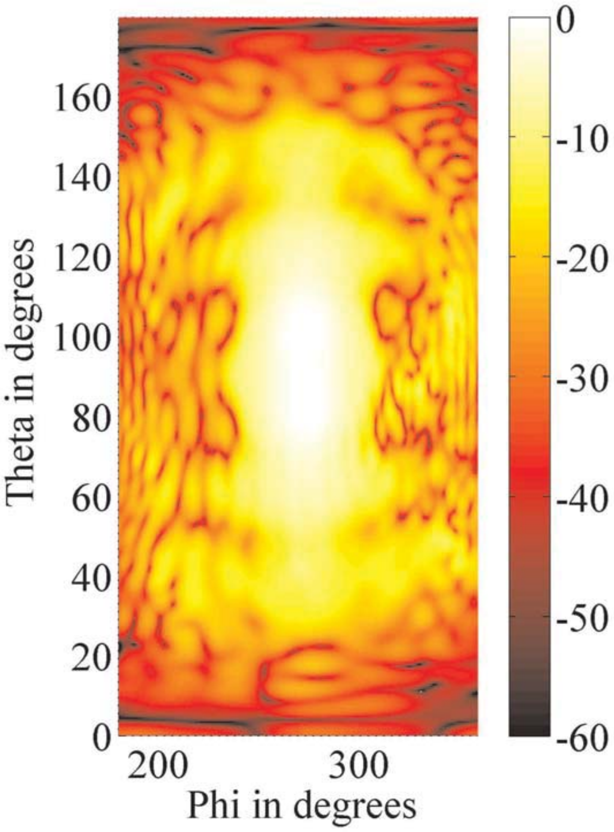

Figure 4.23: Normalized E_ϕ far-field pattern of the DRH18 broadband antenna at 8.2 GHz in dB obtained from near-field data in presence of echoes from the metal plates.

be made about the results: the results with echo from the metal plates without scattering centers representation shown in Fig. 4.25(a) and Fig. 4.26(a) are not significantly degraded when compared to the reference far-field pattern. Secondly, scattering centers representation of the echo sources leads to a further reduction in the error levels arising due to the echo signals. The first observation can be attributed to the utilization of certain a priori knowledge regarding the size and location of the AUT in the plane wave based NFFFT algorithm. This was not the case for the results obtained with the FFT based algorithm shown in Fig. 4.13. The achieved improvement in the far-field pattern of the AUT when scattering centers are utilized is due to the more accurate source model as previously explained. The source model with scattering centers is closer to the actual source geometry from which the near-field data was obtained. The translations of plane waves from the auxiliary sources to the measurement points can implemented in a multilevel fashion. Neigbhouring scattering

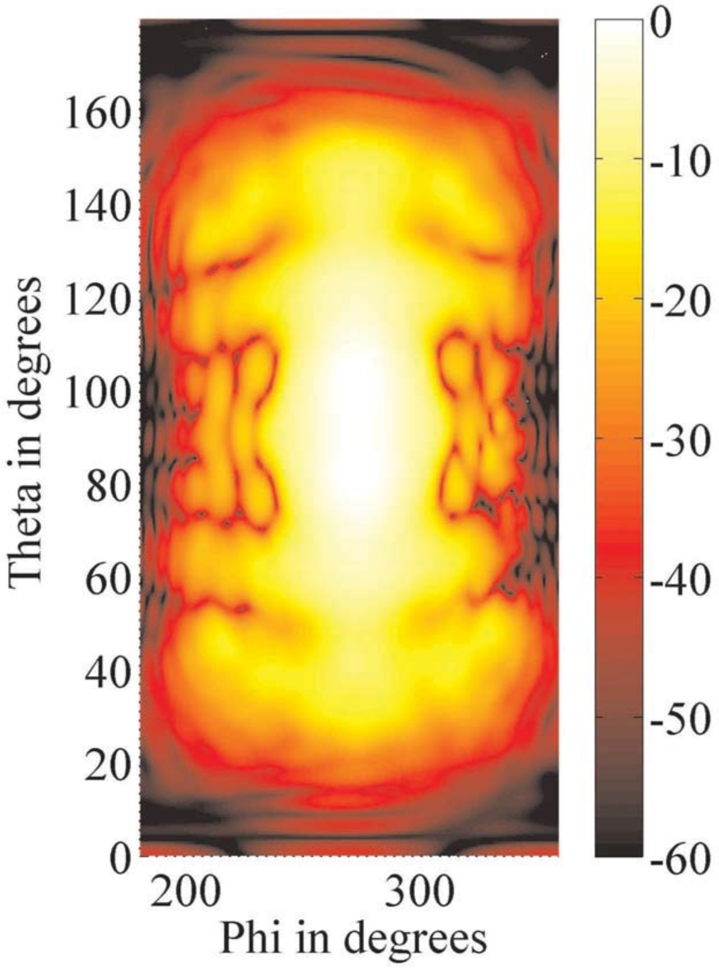

Figure 4.24: Normalized E_ϕ far-field pattern of the DRH18 broadband antenna at 8.2 GHz in dB obtained from near-field data in presence of echoes from the metal plates. The echo sources are included in the NFFFT process by means of localized scattering centers.

centers are combined and plane wave translation is done from the groups of scattering centers to the measurement points similar to the multilevel FMM [Schmidt and Eibert, 2009]. In this way, the number of plane wave translations can be reduced.

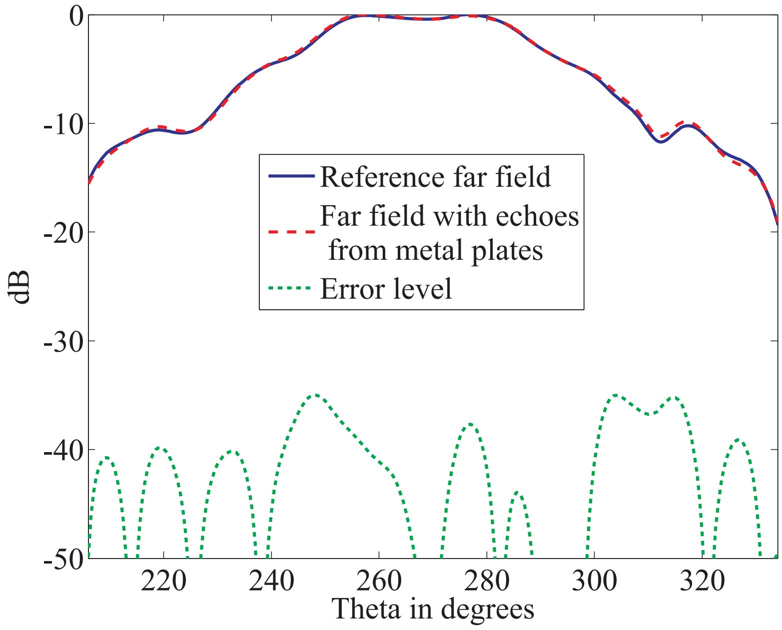

(a) Without scattering centers representation

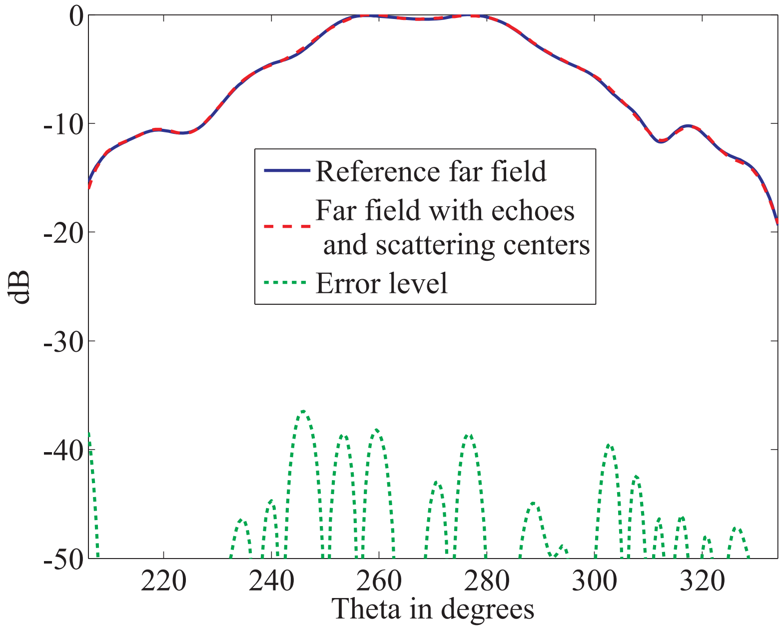

(b) With scattering centers representation

Figure 4.25: E_ϕ E-Plane pattern cuts with and without scattering centers representation for the planar near-field measurement example within the valid angle.

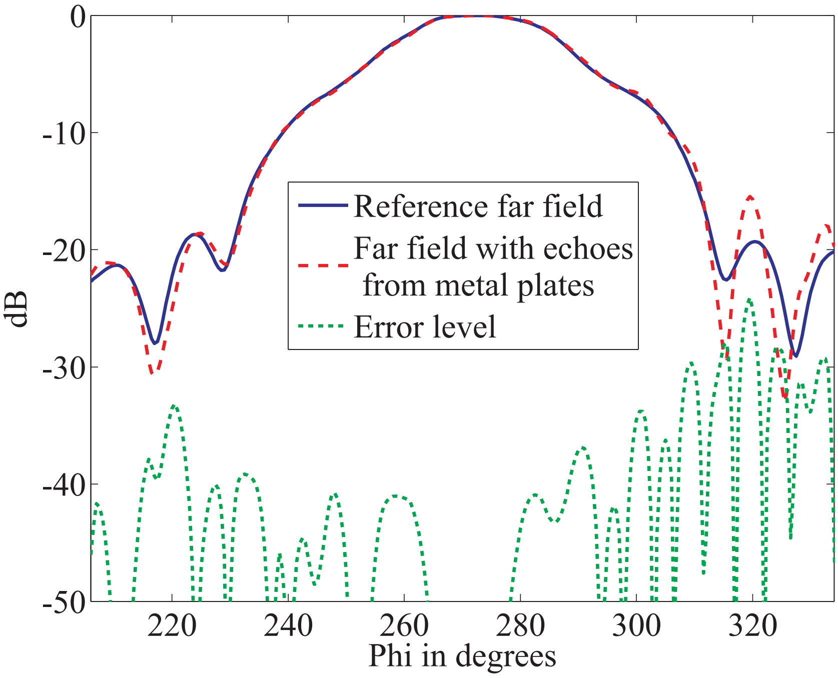

(a) Without scattering centers representation

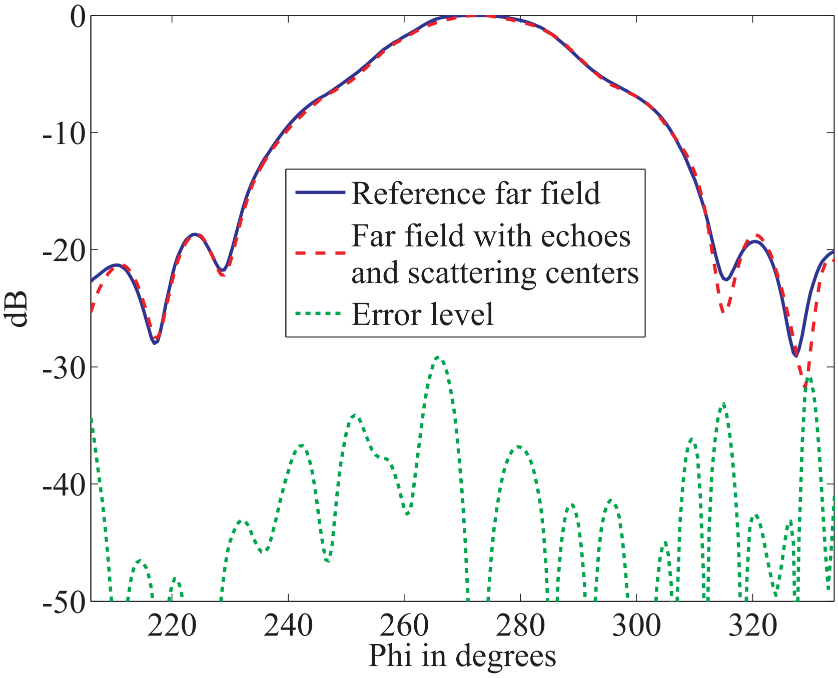

(b) With scattering centers representation

Figure 4.26: E_ϕ H-Plane pattern cuts with and without scattering centers representation for the planar near-field measurement example within the valid angle.

Result for DRH18 at 10.3 GHz

The result is also obtained for a measurement at 10.3 GHz.

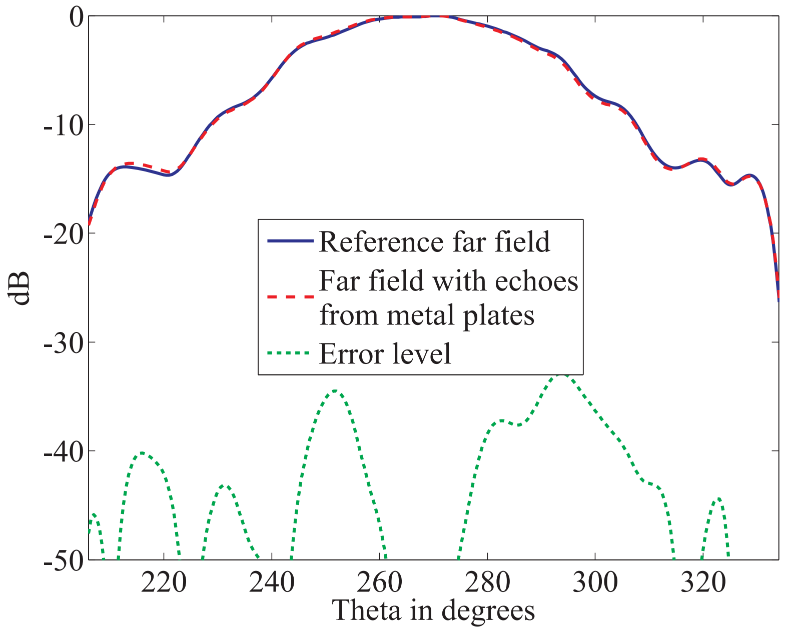

(a) E-Plane

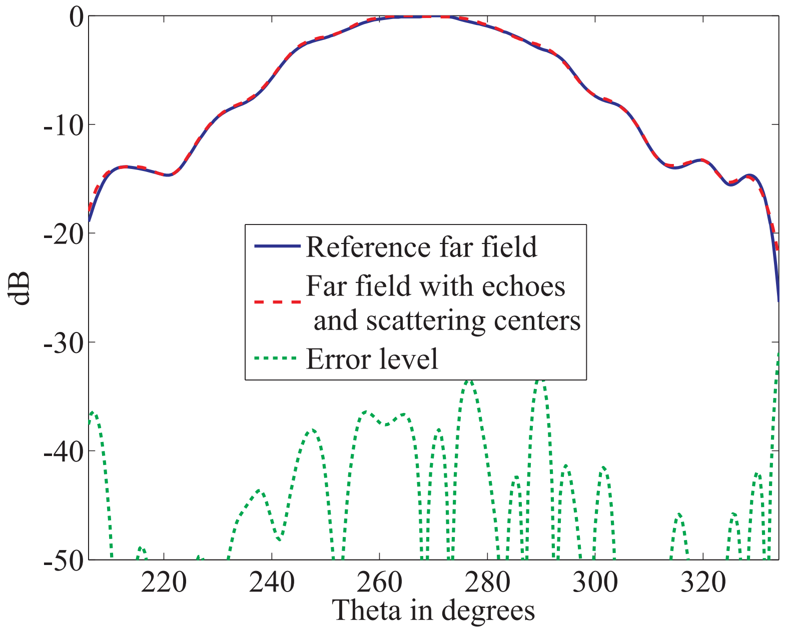

(b) H-Plane

Figure 4.27: H-Plane pattern with and without scattering centers representation for the planar near-field measurement example within the valid angle.

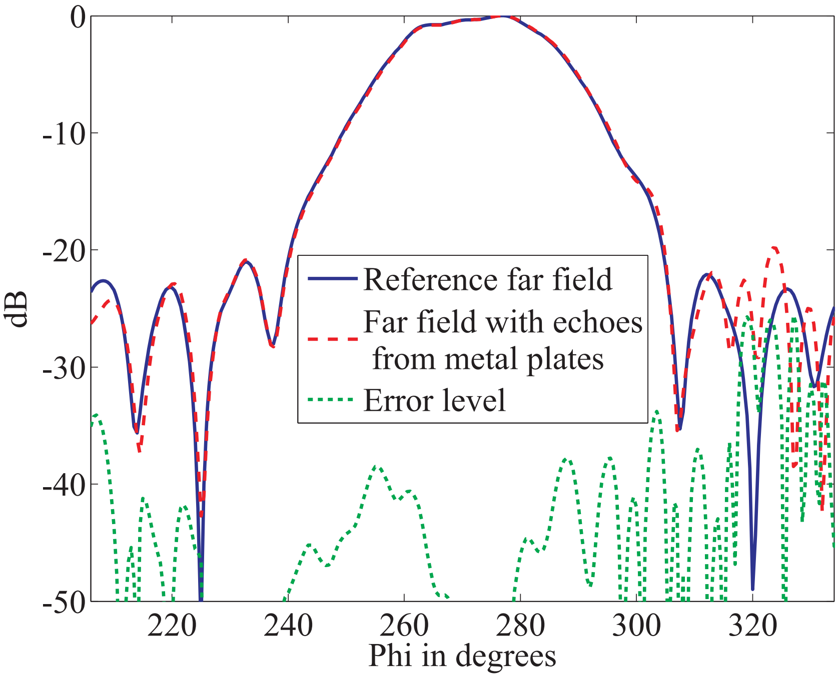

(a) E-Plane

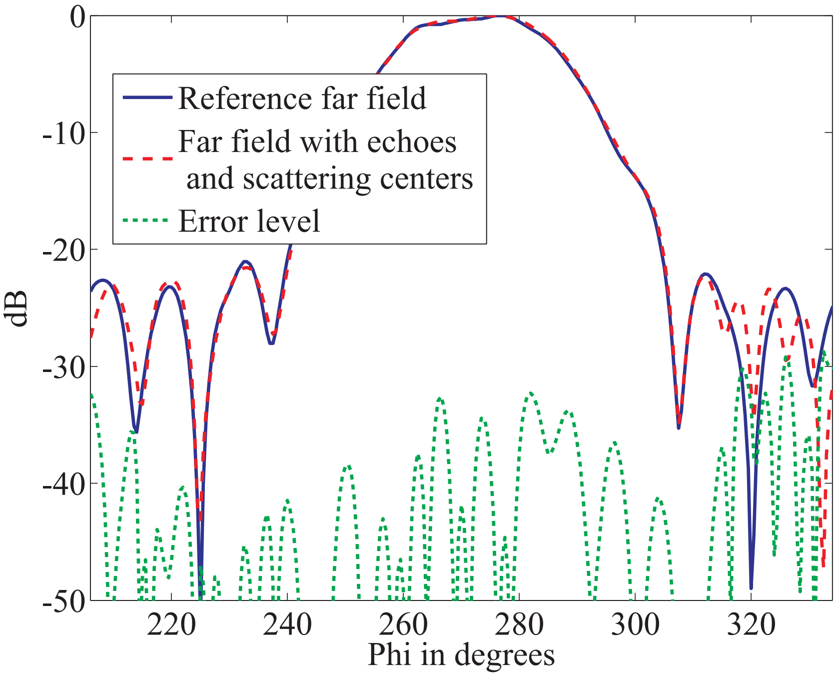

(b) H-Plane

Figure 4.28: E-Plane pattern with and without scattering centers representation for the planar near-field measurement example within the valid angle.

4.3 Scattering Centers Representation of Partially Localized Echo Sources

The previously described placement of auxiliary sources assumes the knowledge of the exact location of the echo sources. Such knowledge is, however, often not available. For instance, in an outdoor measurement facility the number of echo sources may be too large for manual input of all the echo sources. Also, in a semi-anechoic chamber the process of manually computing the echo location in the measurement coordinate system may be time consuming. In these situations, it is useful to find a technique to derive some partial knowledge about the echo sources and to use such limited knowledge for echo suppression. Such partial knowledge that can be derived from the measurement data is the directions of arrival of the echo signals. The distance between the echo sources and the measurement surface will, however, remain unknown. Fortunately, results from scattering centers placement is not sensitive to the distance, as will be shown in the following sections.

4.3.1 Echo Localization

In the absence of echoes and electromagnetic interference, the measured near-field data is completely attributed to the AUT. It has been shown that random measurement errors as encountered in antenna measurements do not introduce significant errors to the solution [Qureshi et al., 2012b]. Therefore, when the measurement is done in an anechoic chamber, Eq. (2.42) is solved using GMRES with enough iterations until the minimum residual is achieved depending on the desired accuracy. A typical convergence of the GMRES algorithm in scenarios where the input source geometry matches the actual source geometry is shown in Fig. 4.29. GMRES converges quickly to a solution with the desired relative residual. However, when the data is perturbed by multipath signals, there can be a significant difference between the solution having the minimum residual and the desired solution corresponding to the AUT plane wave coefficients. The convergence behavior in this case, as shown in Fig. 4.30, is such that the relative residual reduces very slowly and much more iterations are needed to reach the same relative residual as compared to the non-echoic case. Moreover, in presence of multipath signals, the minimum residual solution can be very different from the desired AUT plane wave coefficients. In order to localize the echo sources, an initial low-pass estimate of the AUT far-field pattern is obtained. This can be done by replacing the coupling matrix $\mathbf{C}$ in Eq. (4.1) with a low-rank approximation

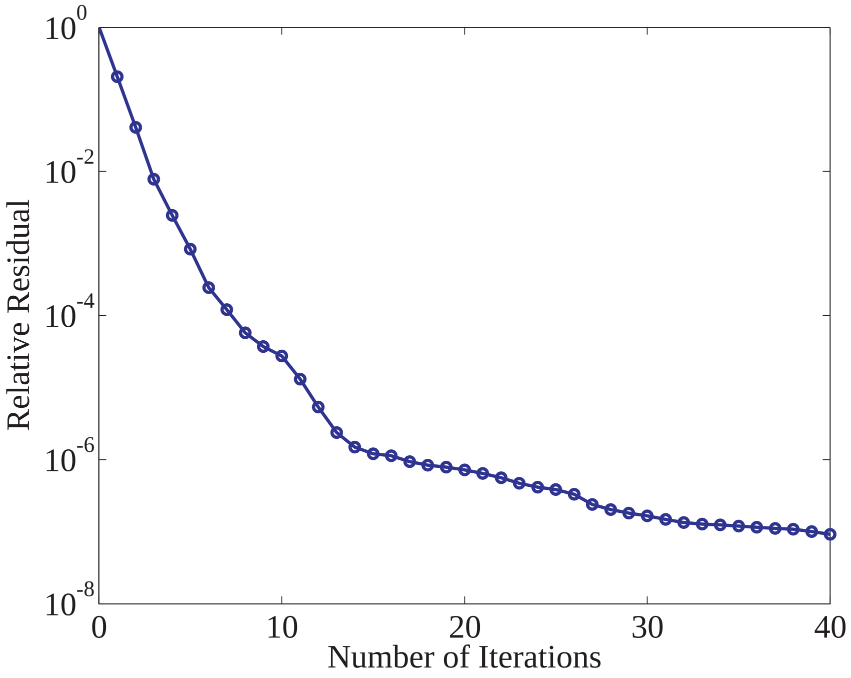

Figure 4.29: When all the information about the source locations are known, GMRES converges to the solution with a decrease in the relative residual for every iteration. In example 1, GMRES converged to a relative residual of 10^{-7} in 40 iterations.

$\mathbf{C}_k = \mathbf{U}\mathbf{\Sigma}_k\mathbf{V}^H$, where $\mathbf{U}$ and $\mathbf{V}$ coincide with the left-singular and right-singular vectors obtained from the singular value decomposition (SVD) of the matrix $\mathbf{C}$, respectively, and $(\cdot)^H$ denotes complex conjugate transpose. The diagonal matrix $\mathbf{\Sigma}_k$ contains the singular values of $\mathbf{C}$ with values less or equal to the k-th singular value set to zero [Manning et al., 2009]. By obtaining the solution over a restricted singular value spectrum, the obtained solution is less sensitive to noise and the effect of the echo contribution is restricted. The result is, however, a poor approximation of the desired final result as high-pass components of the AUT are also restricted. The computation of the SVD can be computationally costly due to the size of the involved matrix. However, due to the regularization properties of the GMRES algorithm [Calvetti et al., 2002b], a similar low-rank solution can be obtained by terminating the GMRES algorithm after a few iterations. The result, $\tilde{\boldsymbol{J}}'_{\boldsymbol{k}}$, obtained at this stage from the normal system of equations,

$$\mathbf{C}_k^H \cdot \boldsymbol{U}' = -\mathrm{j}\frac{\omega\mu}{4\pi}\mathbf{C}_k^H\mathbf{C}_k \cdot \tilde{\boldsymbol{J}}'_k, \tag{4.7}$$

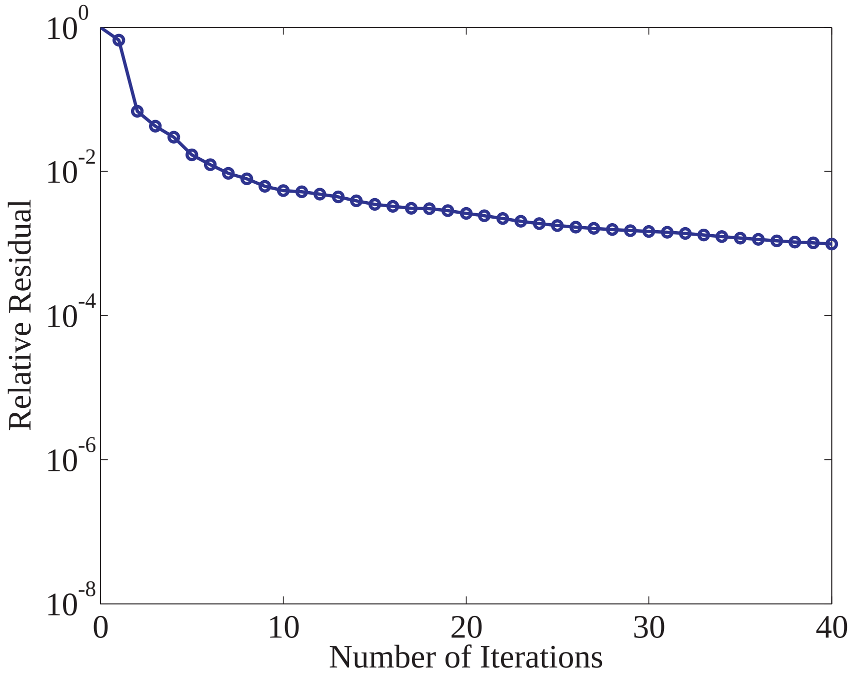

Figure 4.30: Convergence behavior of the GMRES algorithm for the echoic scenario in Fig. 4.5. The solution did not converge to the desired 10^{-7} in 40 iterations.

is associated with a relatively large residual mainly composed of the multipath contributions. In the second stage, the far-field residual

$$\boldsymbol{r} = \mathbf{C}_k^H \cdot \boldsymbol{U}' + \mathrm{j}\frac{\omega\mu}{4\pi}\mathbf{C}_k^H \mathbf{C}_k \cdot \tilde{\boldsymbol{J}}_k', \tag{4.8}$$

is evaluated and the directions of the echo sources are identifiable from the peaks in the far-field pattern. This localization procedure is particularly effective for echo sources having a relatively high contribution in the measured near-field data. For relatively lower-level echo sources, the retrieval of the echo locations can be performed iteratively. This means that the high-level echo sources are retrieved first and the locations of the remaining echo sources are retrieved from the residuals.

Echo Localization Example

The effectiveness of the echo localization technique using far-field residual is demonstrated using the synthetic near-field data generated from the scenario in Fig. 4.5. In order to find the directions of the echo sources, an initial estimate of the AUT plane wave coefficients is obtained by an early termination of the GMRES algorithm as previously described. The obtained far-field from the residual after five iterations for the echo scenario in Fig. 4.5 is shown in Fig. 4.31. The direction of the three echo sources can be seen clearly from the figure. The obtained information from the above procedure can be combined with any a priori knowledge, such as the room dimensions to fix the scattering centers locations.

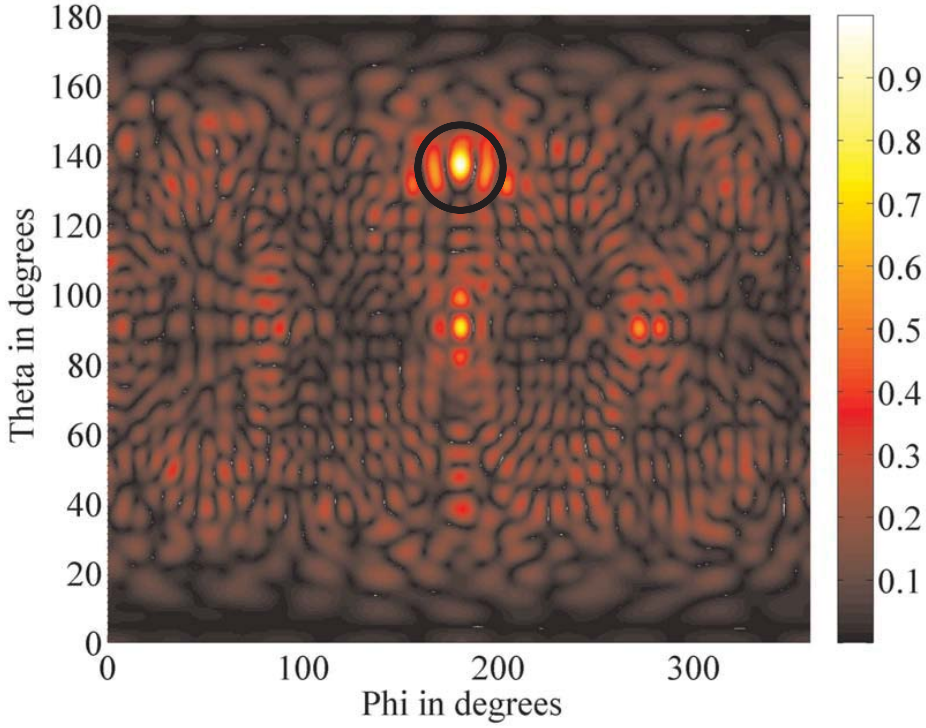

Figure 4.31: Normalized far-field in linear scale obtained by the residual from an early termination of GMRES for the 3 GHz horn antenna. The echo locations correspond to the peaks in the far-field pattern.

Iterative Echo Localization

Large dynamic range between the different echo sources can make it difficult for a simultaneous localization of high-level and low-level echo sources. The localization procedure can be implemented in an iterative manner such that the directions of the strongest echo sources are obtained first. The residual is then obtained for the remaining echo sources and the process is repeated until the direction of the weakest echo source is determined. The sequence of echo localization by signal strength for the scenario in Fig. 4.5 is shown in Fig. 4.31 and Fig. 4.32. In Fig. 4.31, the echo location marked within the circle is the strongest. This strong echo source may influence the determination of other echo directions from the same far-field residual as the weaker are more difficult to identify. However, as it can be seen in Fig. 4.32, the weaker echo sources become more visible once the strongest echo sources are removed. Removal of echo sources is performed by assuming an auxiliary source in the obtained location and solving for the plane wave coefficient of that auxiliary source in the inverse problem solution. Once the plane wave spectrum of the source is obtained, the far-field residual excluding the source can be obtained similar to Eq. (4.8). The stronger echo sources can be further removed from Fig. 4.32 in order to easily recognized the remaining echo sources and the iteration continues as necessary.

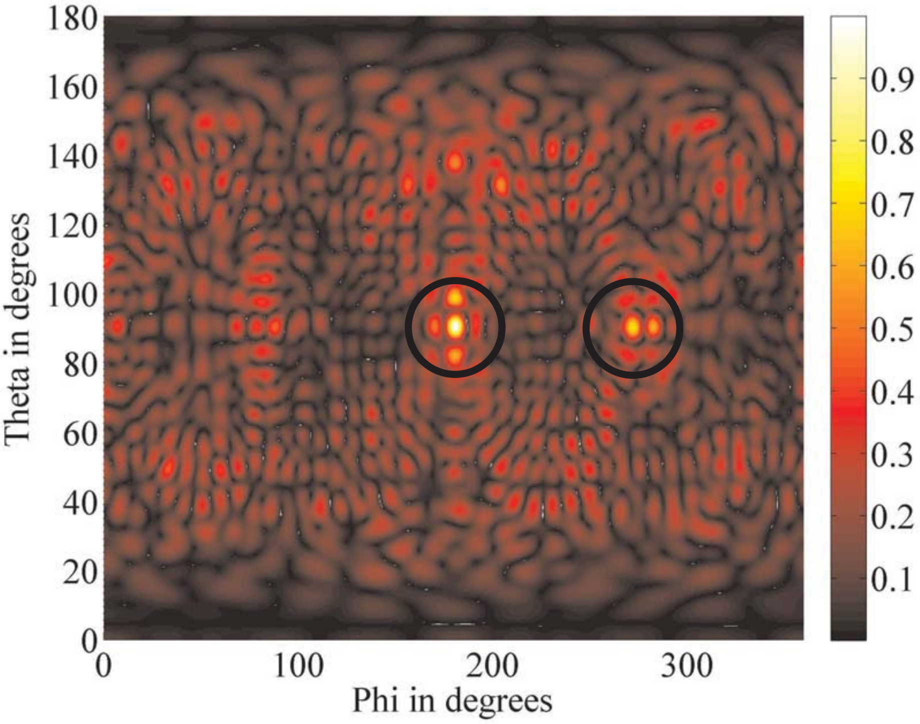

Figure 4.32: Normalized far-field in linear scale obtained by the residual from an early termination of GMRES for the 3 GHz horn antenna. In this figure, the remaining echo sources within the circles are enhanced once the stronger echo source was removed during the previous iteration.

4.3.2 Sensitivity to Errors in Scattering Centers Placement

Echo localization using the far-field residual finds only the directions of the echo sources. The radial distance of the scattering centers can be chosen according to the room dimensions or other a priori information regarding the echo sources. Since the exact knowledge about the echo sources may not always be available, it is important to investigate the robustness of the scattering centers modeling to errors in scattering centers placement. The errors can be in the radial distance of the scattering centers or in the angular placement of the scattering centers. The two types of errors are investigated for the three echo sources modeled in the echo scenario of Fig. 4.5. In Fig. 4.33 the mean error in the H-plane E_ϕ pattern is plotted against errors in the radial placement of the scattering centers. The variable d is the ratio between the scattering centers distances to the true echo locations, i.e. $d = 1$ corresponds to the case where the scattering centers are perfectly placed. It can be seen that the error level in the far-field pattern is still reduced even with errors in the radial placement of scattering centers compared to the far field where no scattering centers are employed. The result for errors in the angular placement of the scattering centers is shown in Fig. 4.34. In this figure, the x axis is the amount of error introduced in the θ and ϕ angu-

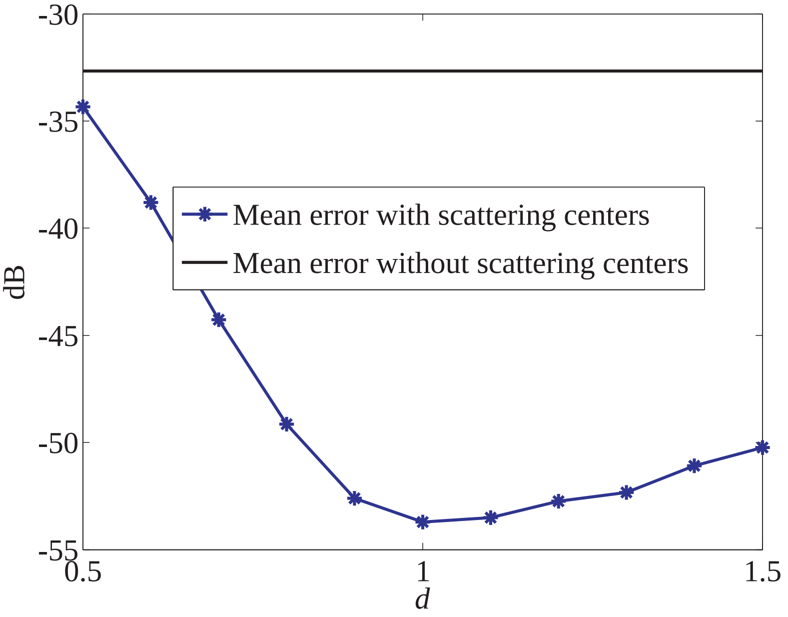

Figure 4.33: H-plane average error for the 3 GHz horn antenna plotted against errors in the scattering centers radial placement, d is the ratio between the scattering centers distances to the true echo locations.

lar placement of the auxiliary sources. It can be observed that the placement of scattering centers to represent the echo sources results in a reduction of the error level even when the locations of the echo sources are only partially known.

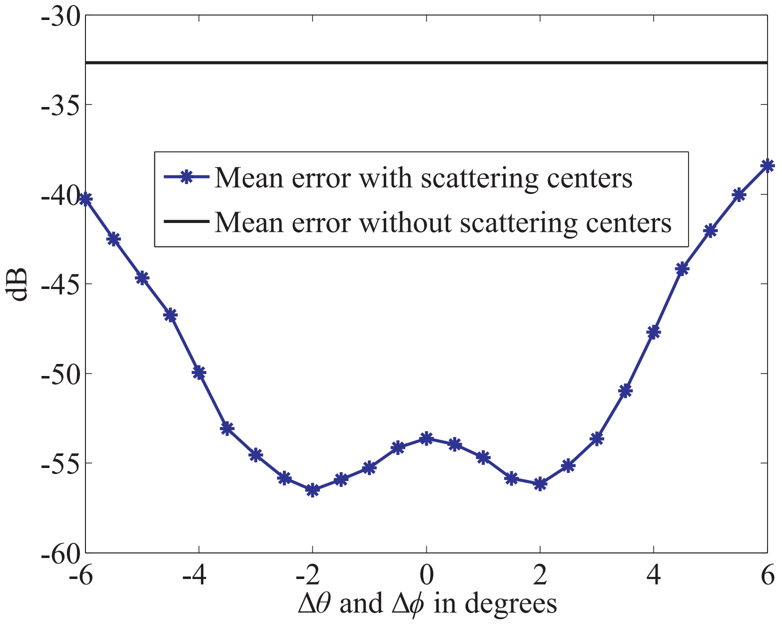

Figure 4.34: H-plane average error for the 3 GHz horn antenna plotted against errors in the scattering centers angular placement. The same amount of error is introduced in both θ and ϕ placements of the scattering centers.

4.4 Scattering Centers Representation without Echo Localization

In some situations, either due to the number of echo sources or because of the dynamic range of the involved sources, echo locations are unknown and echo localization is not feasible. Scattering centers placement in these situations can still be performed in order to represent the unlocalized echo sources. To improve the achievable echo suppression without knowledge of the echo locations, the scattering centers placement are optimized by searching for locations where the least amount of error is introduced by location mismatch between the echo sources and the auxiliary sources. To this end, an echo free measurement is made and a single scattering center is placed at a particular location during the NFFFT process. The NFFFT is repeated several times with the scattering center at varying locations and the attributed energy is recorded. The optimal placement of scattering centers in this situation is found to be along the plane containing the AUT aperture but restricted to the regions outside the measurement sphere as shown in Fig. 4.35. This placement of the scattering centers is similar to the spatial filtering echo suppression technique presented in [Cano-Fácila et al., 2011]. In that technique, the PWS of the AUT is obtained over an extended aperture to obtain the image sources due to reflections from the floor, ceiling and walls of the measurement room. The PWS is then spatially filtered such that the far-field pattern of the AUT is computed only with the PWS over the AUT aperture. The spacing between the scattering centers and the multipole orders of the scattering centers must be chosen carefully so that the minimum spheres enclosing the auxiliary sources do not intersect with each other. The placement of scattering centers over the plane containing the AUT aperture is implemented for the echoic data generated from the scenario depicted in Fig. 4.5. A total of 200 scattering centers are placed over a square outside the measurement sphere each with a multipole order of 4 to represent the three echo sources whose locations are assumed to be unknown. Plane waves are assumed for the AUT and for each of the scattering centers. Once the plane wave coefficients for all the sources are obtained, the far-field pattern of the AUT is evaluated using the plane wave coefficients of the AUT. The obtained results with the representation in Fig. 4.35 is shown in Fig. 4.36 and Fig. 4.37.

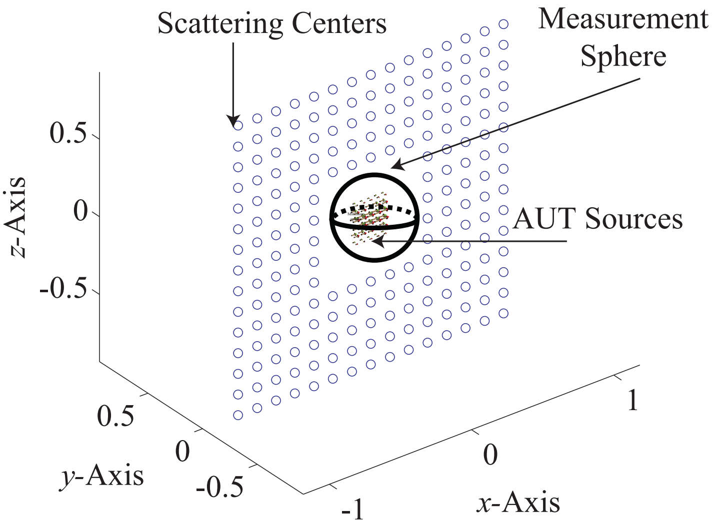

Figure 4.35: When the echo locations are unknown, the auxiliary sources are placed on the same plane as the AUT aperture but limited to the region outside the measurement sphere.

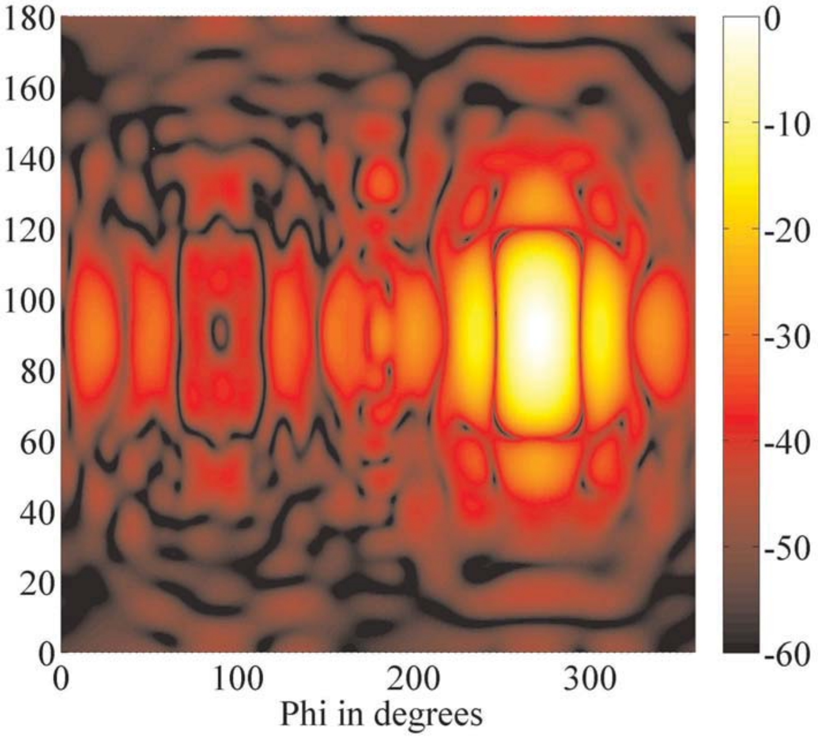

Figure 4.36: Normalized E_ϕ far-field pattern of the 3 GHz horn antenna in dB obtained from the echoic near-field data generated from the scenario in Fig. 4.5. The echo sources are included in the NFFFT process by scattering centers on the AUT aperture plane.

The results show an improvement in the obtained far-field pattern with echo signals compared to when no echo suppression was applied. However, the result is not as good as the ones obtained when exact or partial knowledge of the echo source locations are used during scattering centers placements.

4.5 Summary

In this chapter, techniques were presented to improve the scattering model for the plane wave based near-field far-field transformation algorithm when measurements are acquired in echoic environments. This is done by representing the echo sources by means of auxiliary sources and integrating them during the NFFFT process. Sets of plane wave sources are assumed for the auxiliary sources and these plane waves are translated to the measurement points in the same way plane wave translations are performed from the AUT. The

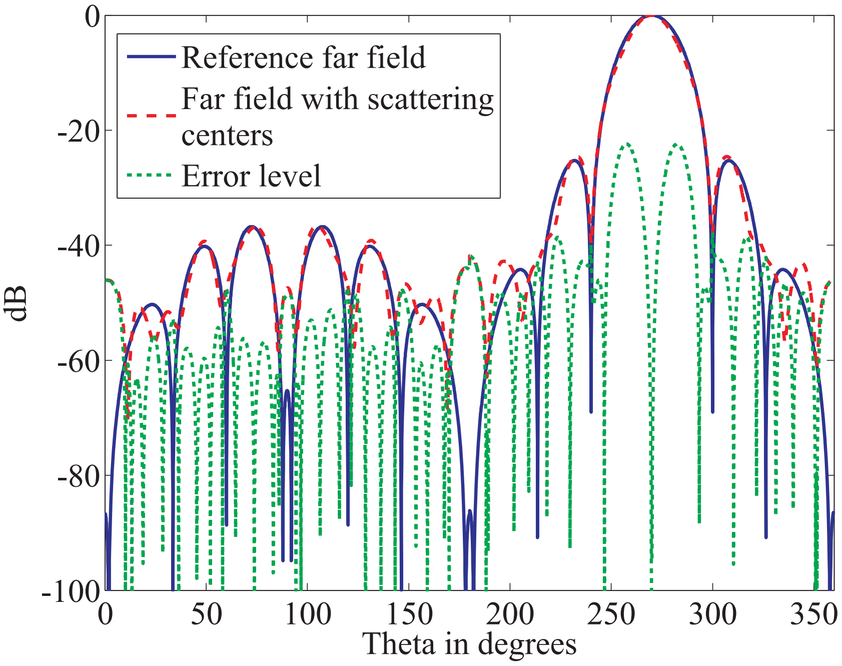

(a) E-plane pattern

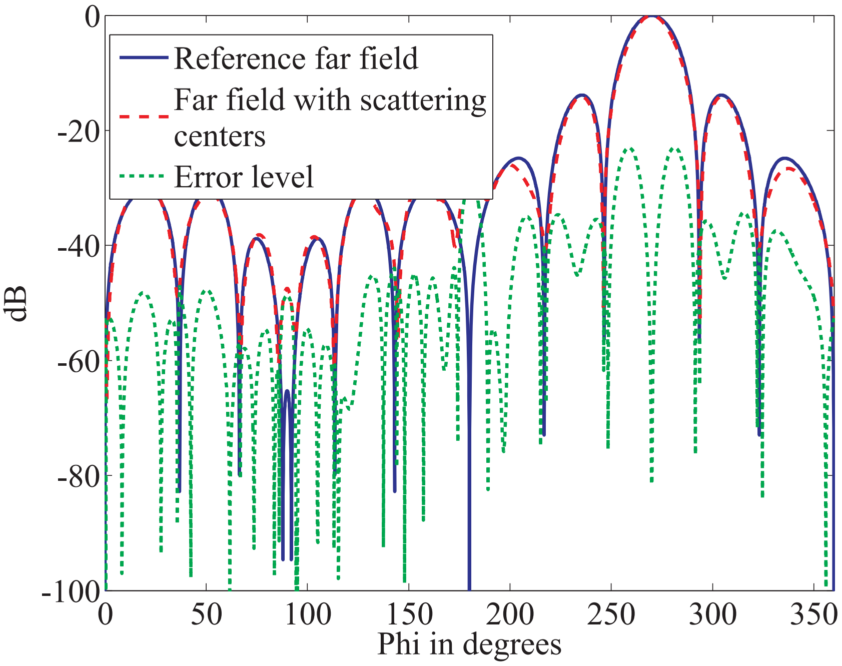

(b) H-plane pattern

Figure 4.37: Far-field pattern cuts obtained by placing scattering centers on the plane containing the AUT aperture.

equivalent sources for all the contributing sources are then obtained in an inverse problem solution. When the locations of the echo sources are unknown, techniques for determining the echo directions as well as techniques for scattering centers placement without echo localization were presented. These techniques ensure that the inverse problem is set-up with a source geometry that is closer to the actual source geometry from which the near-field data is obtained.

Chapter 5

Multi-probe Antenna Measurement Technique

Reducing the influence of multipath propagation in antenna measurements usually takes the form of post-processing of acquired echoic data, a particular echo aware acquisition approach or a combination of both. Measurement approaches involve the use of specialized hardware or acquiring the field such that the possible removal of the echo signals is enhanced. Measurement approaches that facilitate the removal of multipath signals lead to near-field data that incorporates more information about the echo sources than the usual measurement procedures. In Chapter 4, techniques were presented to improve the model of the inverse problem from which the AUT far-field pattern is obtained. The techniques involved the assumption of auxiliary sources for the echo sources such that the model of the scattering situation is closer to the actual echoic environment. In this way, additional unknowns are introduced due to the echo sources. In this chapter, a measurement technique is described which enhances the extraction of multipath components during data post-processing such as near-field far-field transformations. This is achieved by taking several independent near-field measurements with multiple probe antennas such that adequate information is available to resolve the direct contributions of the AUT and the contributions of the echo sources [Yinusa and Eibert, 2013a,b,c]. Particularly useful for this purpose are measurements with probe antennas looking towards and away from the AUT. The echo contributions are then retrieved by means of auxiliary sources during the NFFFT process. The

AUT is assumed to be fixed during the measurement campaign. Therefore, the technique is not suitable for the standard roll-over-azimuth scanners but it works for any measurement set-up with a fixed AUT. Also, more advanced positioners such as those equipped with robotic arms [Francis et al., 2014] will allow for more flexibility regarding the probe orientation during near-field measurements which will make inward and outward looking probes easily achievable. In [Hill, 1998] and [Hill, 1997], Hill proposed ideal Huygens' probes or an approximation by means of inward and outward probes with spherical wave expansion when sources are present inside and outside the measurement sphere. However, no results have been presented for real probes with or without probe correction. The multi-probe antenna measurement technique when applied in near-field measurements results in near-field data that contains more information about the various sources, such as the AUT and the echo sources, contributing to the measurement signal.

5.1 Theory

In order to illustrate the concept of multi-probe antenna measurements, consider the transmission line set-up with the AUT located inside the transmission line as shown in Fig. 5.1. The AUT is assumed to generate single mode transmission line waves with wave amplitudes b_{10} and b_{20}. Assuming that there are no reflections on the transmission line, i.e. $r_1 = 0$ and $r_2 = 0$, the wave amplitudes generated by the AUT, b_{10} and b_{20}, can be retrieved independently from a single measurement at each port if the coupling factors between the waves and the assumed probes are known. Possible probes for this 1D scenario include, for example, directional couplers which measure the wave in a particular direction on a transmission line. If $r_1 \neq 0$ and $r_2 \neq 0$, however, the measured signal is corrupted, i.e. it is not attributable only to the AUT. Additional information is therefore needed in this case to separate the direct AUT contributions from that of the echo sources. For the scenario shown in Fig. 5.1, four independent measurements, two at each port, are sufficient to set up a system of equations for the four unknown wave coefficients of the incoming waves, a_1 and a_2, and the outgoing waves, b_1 and b_2, at each port. The first and second measurements required at each port can then be obtained, for example, by utilizing directional couplers coupled to the waves in the forward and reverse directions, respectively, at each port. An alternative approach providing an equal amount of information is to measure the currents and voltages at the two ports. The incoming and outgoing wave coefficients can then be

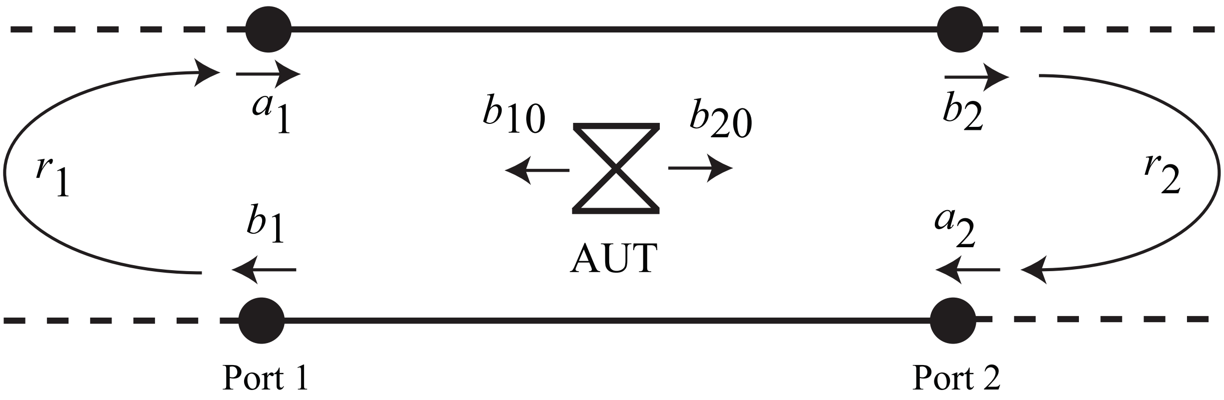

Figure 5.1: 1D antenna measurement scenario as transmission line. Copyright ©2013, IEEE.

obtained by simultaneously solving the well known voltage and current equations for the transmission line. In both approaches, however, it is assumed that there are no multiple interactions between the AUT and the disturbers i.e. no additional currents are induced on the AUT as a result of the scattered signals.

Next, the consideration is extended to a general 3D measurement set-up, e.g. a spherical measurement set-up with the AUT at the origin as shown in Fig. 5.2. The probe an-

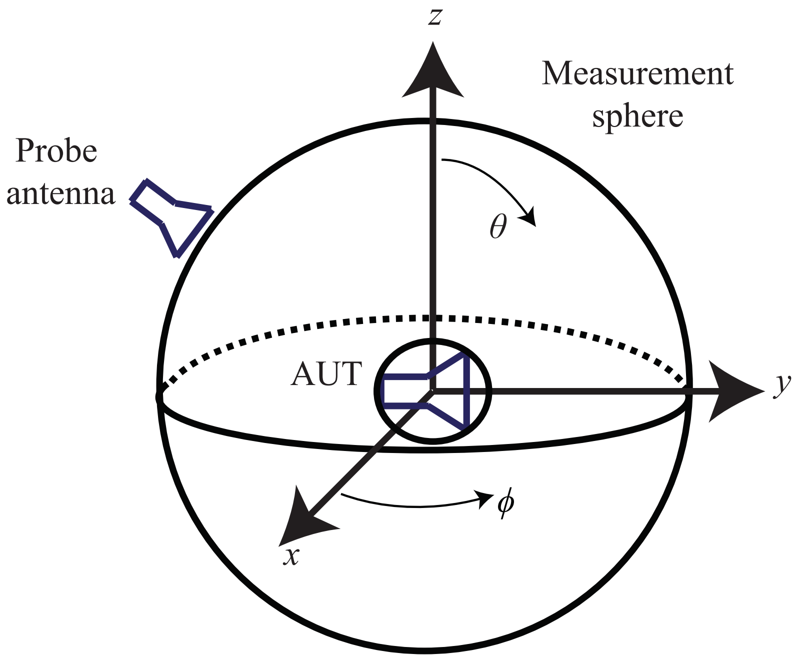

Figure 5.2: Spherical measurement setup.

tenna measures the near-field distribution on the chosen measurement surface. Due to the band limited nature of the radiated field, measurements are done at discrete points over the surface following an appropriate sampling criteria. Regarding the probe antennas, the advantages of directive probes in avoiding multipath signals have been studied in [Hansen and Larsen, 1984]. The idea there was to improve the signal to echo ratio by amplifying the line-of-sight signals and by attenuating the echo signals at the probes. The effect of the probe patterns was then corrected during the NFFFT. The drawbacks of this approach include the need for highly directive probe antennas and the possible multiple interactions between the AUT and the probes. Also, there are still individual measurement points which can be strongly corrupted by multipath signals.

A rather theoretical approach, corresponding to the voltage and current measurement in the 1D transmission line example, is to measure both the electric field and the magnetic field distribution on the measurement surface by utilizing electric and magnetic dipoles, respectively, as probes. This has been proven in [Hansen, 1988] to provide adequate information sufficient to differentiate between incoming and outgoing waves with respect to the volume enclosed by the measurement surface. Furthermore, linear combinations of the electric field and the magnetic field could be measured by means of Huygens' source probes. A Huygens' source is realizable with an electric and a magnetic dipole perpendicularly oriented with respect to each other [Best, 2010]. By measuring the field with two particular orientations of the Huygens' source, two linear combinations of the electric field and of the magnetic field are obtained. By this consideration, it is clear that a measurement with inward and outward looking probes provides also sufficient information to distinguish between incoming and outgoing waves with respect to the measurement volume. Following this logic and given the challenges in implementing Huygens' sources, we propose a measurement technique where the AUT is measured with two sets of probe antennas, one set radiating mainly towards the AUT and the other set radiating mainly away from the AUT as illustrated in Fig. 5.3. This can be achieved by probes used twice with different orientations to produce the desired effect or with a multiple probe setup. Every set of the above mentioned probes contains a probe for each of the measured polarizations. This measurement technique, as opposed to avoiding multipath signals, measures more multipath contributions and aids a subsequent integration of those sources into the NFFFT, which can however be separated from the AUT signals.

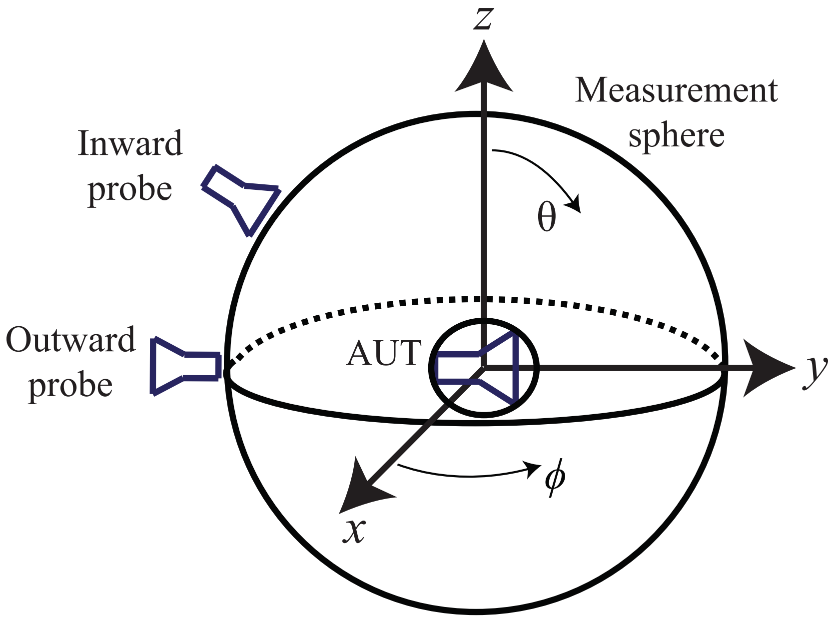

Figure 5.3: Multi-probe measurement set-up. This measurement set-up consists of two sets of probes, one directed towards the AUT and the other directed away from the AUT. Each set contains typically probes for two independent polarizations.

5.2 Integration with Plane Wave Expansion

The near-field measurement procedure with the multi-probe approach results in two pairs of near-field data for each measurement point; two orthogonal polarizations for the inward looking and for the outward looking probes. Outgoing plane waves are assumed for the AUT and plane wave translations are done from the AUT to the measurement points as previously described. The computation of the translation operator remains unchanged and is performed only once for each measurement point. The plane waves are weighted with the far-field pattern of the corresponding probe which now has four degrees of freedom instead of two. This leads to twice the number of equations in the linear system of equations in Eq. (2.42) as more measurement samples are available from the outward looking probe.

The coupling matrix in this case

$$\mathbf{C} = \begin{pmatrix} C_\phi^{1i}(k_{\phi 1}, k_{\theta 1}, \phi_1, \theta_1) & \cdots & C_\theta^{1i}(k_{\phi P}, k_{\theta Q}, \phi_1, \theta_1) \\ C_\phi^{1o}(k_{\phi 1}, k_{\theta 1}, \phi_1, \theta_1) & \cdots & C_\theta^{1o}(k_{\phi P}, k_{\theta Q}, \phi_1, \theta_1) \\ \vdots & \ddots & \vdots \\ C_\phi^{1i}(k_{\phi 1}, k_{\theta 1}, \phi_M, \theta_N) & \cdots & C_\theta^{1i}(k_{\phi P}, k_{\theta Q}, \phi_M, \theta_N) \\ C_\phi^{1o}(k_{\phi 1}, k_{\theta 1}, \phi_M, \theta_N) & \cdots & C_\theta^{1o}(k_{\phi P}, k_{\theta Q}, \phi_M, \theta_N) \\ C_\phi^{2i}(k_{\phi 1}, k_{\theta 1}, \phi_1, \theta_1) & \cdots & C_\theta^{2i}(k_{\phi P}, k_{\theta Q}, \phi_1, \theta_1) \\ C_\phi^{2o}(k_{\phi 1}, k_{\theta 1}, \phi_1, \theta_1) & \cdots & C_\theta^{2o}(k_{\phi P}, k_{\theta Q}, \phi_1, \theta_1) \\ \vdots & \ddots & \vdots \\ C_\phi^{2i}(k_{\phi 1}, k_{\theta 1}, \phi_M, \theta_N) & \cdots & C_\theta^{2i}(k_{\phi P}, k_{\theta Q}, \phi_M, \theta_N) \\ C_\phi^{2o}(k_{\phi 1}, k_{\theta 1}, \phi_M, \theta_N) & \cdots & C_\theta^{2o}(k_{\phi P}, k_{\theta Q}, \phi_M, \theta_N) \end{pmatrix}, \qquad (5.1)$$

as usual, relates the measured probe signals

$$\boldsymbol{U'} = \begin{pmatrix} U^{1i}(\phi_1, \theta_1) \\ U^{1o}(\phi_1, \theta_1) \\ \vdots \\ U^{1i}(\phi_M, \theta_N) \\ U^{1o}(\phi_M, \theta_N) \\ U^{2i}(\phi_1, \theta_1) \\ U^{2o}(\phi_1, \theta_1) \\ \vdots \\ U^{2i}(\phi_M, \theta_N) \\ U^{2o}(\phi_M, \theta_N) \end{pmatrix}$$

to the plane wave coefficients of the AUT

$$\tilde{\boldsymbol{J}}' = \begin{pmatrix} \tilde{J}_\phi(k_{\phi 1}, k_{\theta 1}) \\ \tilde{J}_\theta(k_{\phi 1}, k_{\theta 1}) \\ . \\ . \\ . \\ \tilde{J}_\phi(k_{\phi P}, k_{\theta Q}) \\ \tilde{J}_\theta(k_{\phi P}, k_{\theta Q}) \end{pmatrix}. \tag{5.2}$$

The elements of the coupling matrix,

$$C^{(1,2)(i,o)}_{\phi,\theta}(k_{\phi p}, k_{\theta q}, \phi_m, \theta_n) = T_L(\hat{k}, \hat{r}_\mathrm{M}) W(k_{\theta_q}) P^{(1,2)(i,o)}_{\phi,\theta}(k_{\phi p}, k_{\theta q}, \phi_m, \theta_n), \tag{5.3}$$

take into account plane wave translations, weighting of the plane waves with the far-field pattern of the corresponding probe, and the weights needed for integration over the sphere. The superscripts i and o refer to the inward and outward looking probes, respectively. Echo sources are integrated into the near-field far-field transformation process by means of auxiliary sources. Outgoing plane waves are assumed for the auxiliary sources as described in Chapter 4. Similar to the AUT, the outgoing plane waves from the auxiliary sources are translated to incoming plane waves at the probes. The incoming planes waves are thereafter weighted by the far-field pattern of the inward and outward looking probes. The resulting linear system of equations is solved iteratively to retrieve the plane wave coefficients of the AUT and those of the auxiliary sources representing the echo sources. The multi-probe measurement technique is tested with the echoic scenario depicted in Fig. 4.5. The sampling criteria are the same as with the single probe measurement only that additional measurement samples are acquired with an outward looking probe. Auxiliary sources each with a multipole order of 4 are used to represent the echo sources. The result of the NFFFT process with localized auxiliary sources are shown in Fig. 5.4 and Fig. 5.5. It can be observed that the obtained far-field pattern is closer to the reference far-field compared to the case of the single probe measurement in Fig. 4.15 and Fig. 4.16. This is because the scattering centers approach provides the information to set-up the additional unknowns through the assumption of auxiliary sources and the multi-probe data provide the information needed to determine those additional unknowns.

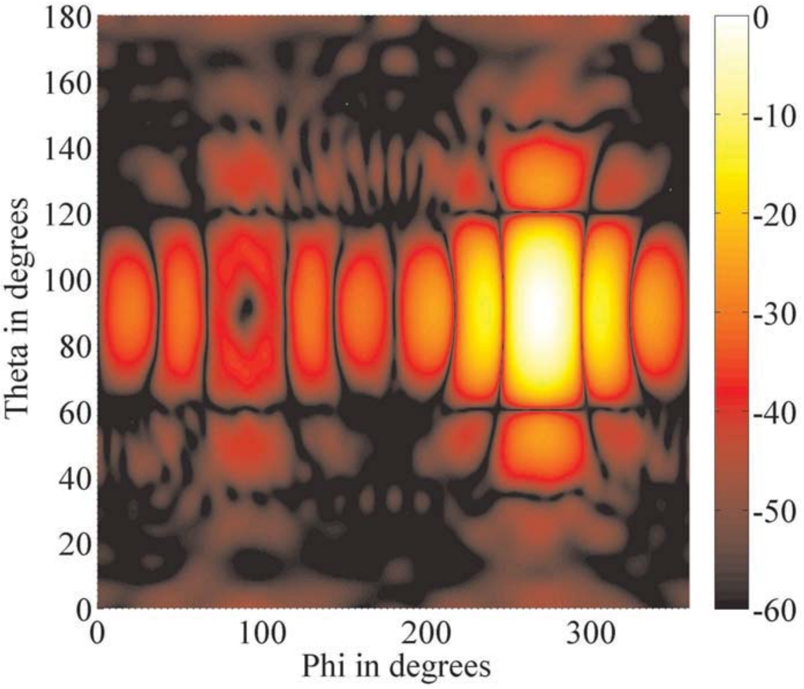

Figure 5.4: Normalized E_ϕ far-field pattern of the 3 GHz horn antenna in dB obtained from the echoic near-field data generated from the scenario in Fig. 4.5. The near-field data is acquired by the multi-probe technique and the echo sources are included in the NFFFT process by means of localized scattering centers.

Sensitivity to scattering centers placement

When the exact locations of the echo sources are not known, the directions of the echo sources can be found using the technique based on the far-field residual described in section 4.3.1. The auxiliary sources are then placed along the line of sight between the target echo source and the AUT. This approach to scattering centers placement introduces an error to the distance between the measurement surface and the auxiliary sources representing the echo sources. In order to further study the robustness of the measurement technique to errors in the scattering centers placement, the NFFFT was performed several times with the auxiliary sources placed at various locations along the lines connecting the origin and the target echo source, i.e. the errors are introduced in the radial distances of the auxiliary sources. The mean values of the error between the reference far-field and far-field obtained from echoic near-field data are plotted in Fig. 5.6 for the main cuts, where d is the ratio between the scattering centers distances to the true echo locations, i.e. $d = 1$ corresponds

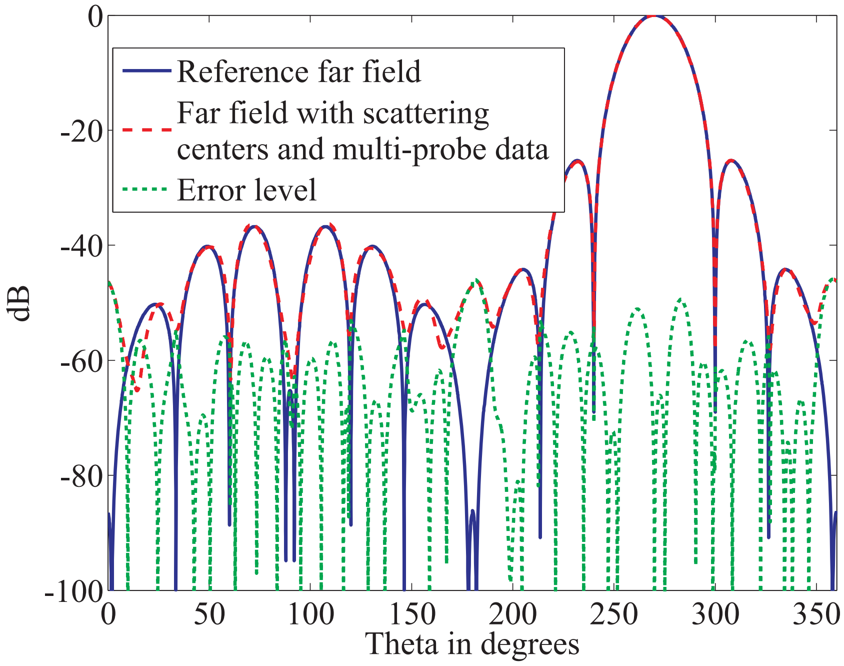

(a) E-plane pattern

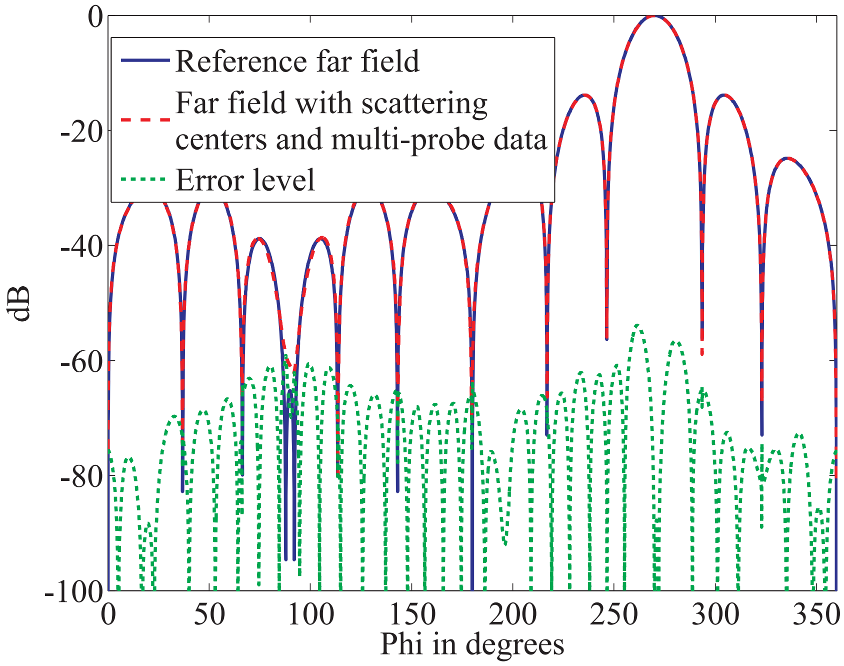

(b) H-plane pattern

Figure 5.5: Far-field cuts for the result in Fig. 5.4.

to the case where the scattering centers are perfectly placed. A similar study is performed for errors in the angular placement of the scattering centers. To this end, the radial distance of the scattering centers are kept accurate and an equal amount of errors are introduced in the phi and theta angles of the scattering centers during the NFFFT process. The mean values of the error for this case is plotted in Fig. 5.7. It is clear that the echo suppression capability does not degrade with some errors in the scattering centers placement when the measurement is acquired using the multi-probe measurement approach.

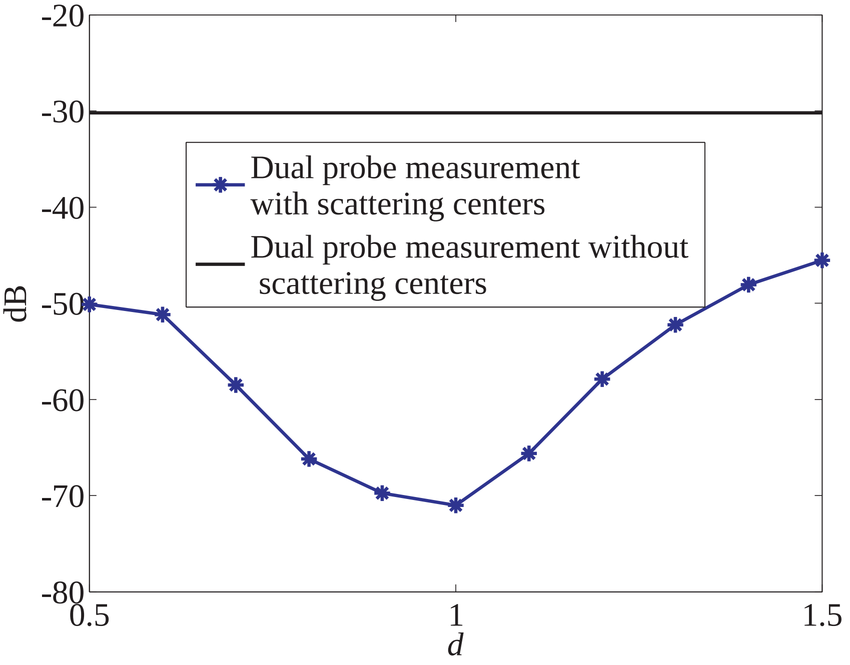

Figure 5.6: H-plane average error for the 3 GHz horn antenna plotted against errors in the scattering centers radial placement, d is the ratio between the scattering centers distances to the true echo locations.

Synthetic data as used in the previous example allows the isolation of the intended type of measurement error, in this case, the effect of multipath propagation and the impact of the proposed technique in mitigating such an effect. Since actual measurements might contain other forms of errors apart from multipath propagation, it is important to demonstrate how the proposed measurement technique performs in such situations. A second example is therefore provided utilizing data measured in an anechoic chamber. The AUT is a 1.92 GHz base station antenna with a minimum sphere radius of 0.7 m similar to the one shown in Fig. 5.8. A sample spacing of 4° is utilized along both the ϕ and θ directions at a measurement radius of 2.7 m. The probe antenna in this case is an open-ended waveguide. Data for a single echo source located on the x-axis, 7.0 m away from the origin is generated synthetically using the coupling matrices for the outward and inward probes. The synthetic

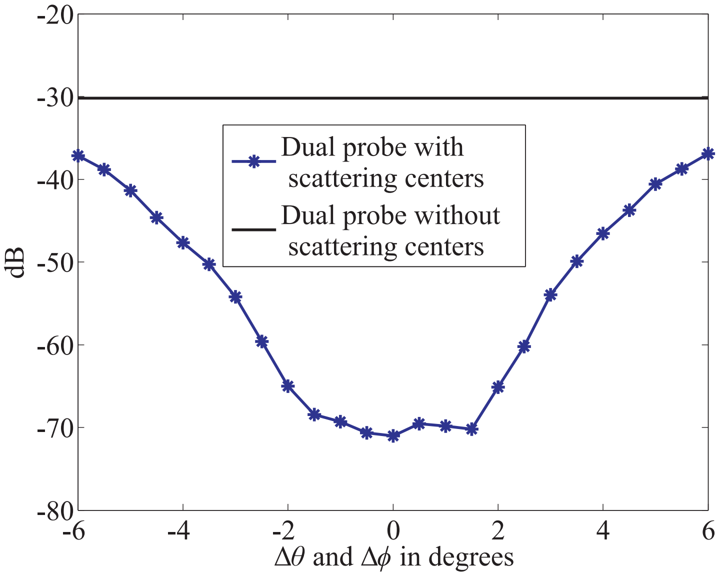

Figure 5.7: H-plane average error for the 3 GHz horn antenna plotted against errors in the scattering centers angular placement. The same amount of error is introduced in both θ and ϕ placements of the scattering centers.

data for the echo source is then superimposed on the measured AUT signal to generate the echoic data employed in the NFFFT. Fig. 5.9 and Fig. 5.10 show the result for measurements with multiple probes with a scattering center placed at the echo location during the NFFFT. Fig. 5.11 shows the sensitivity to errors in the placement of the scattering center.

Figure 5.8: A base station antenna [UVSAR].

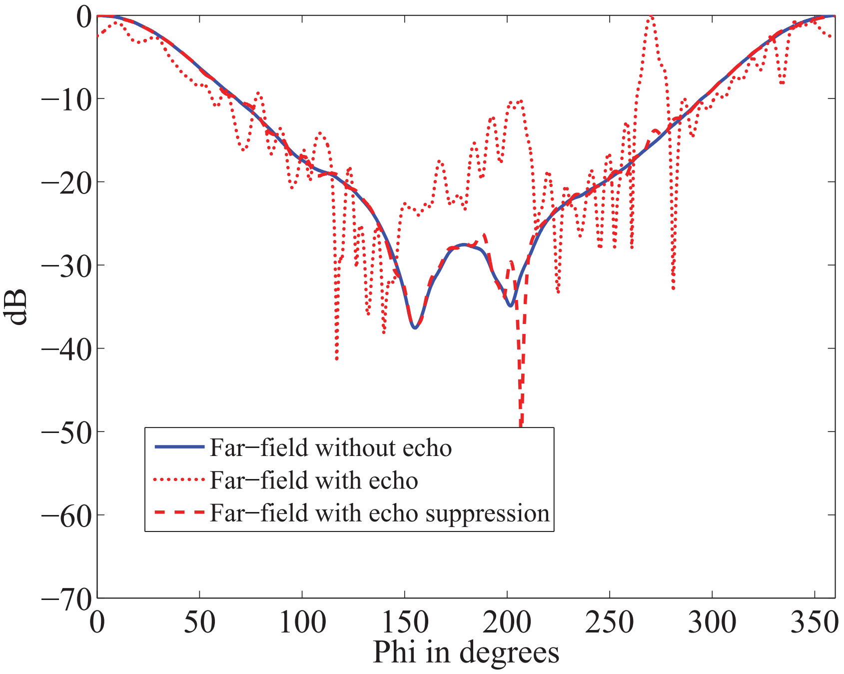

Figure 5.9: H-plane ($\theta = 90°$) cut through the reference far-field, far-field with echo and the far-field with echo suppression for the base station antenna.

Planar Measurement Set-up

For the planar measurement set-up, a scan plane of 4.0 m by 4.0 m is chosen at a measurement distance of 0.5 m resulting in a valid angle of about 75° around boresight. The sample spacing is $\lambda/2$ with the same probe antenna with the far-field pattern shown in Fig. 4.3. The multi-probe measurement is done with one set of probes radiating mainly towards the plane containing the AUT aperture and a second set of probes radiating away from it. Echo localization as described in Sec. 4.3.1 is limited to echo sources within the valid angle but the technique is also applicable with manual input of the echo source locations. A single echo source is introduced at a distance of 0.5 m on the y-axis behind the scan plane and two sets of near-field data are generated with the shown probe orientations in Fig. 5.12. Auxiliary sources are introduced during the NFFFT to retrieve the multipath components as earlier described. Fig. 5.13 and Fig. 5.14 show the far-field with and without echo suppression for the H-plane and E-plane, respectively.

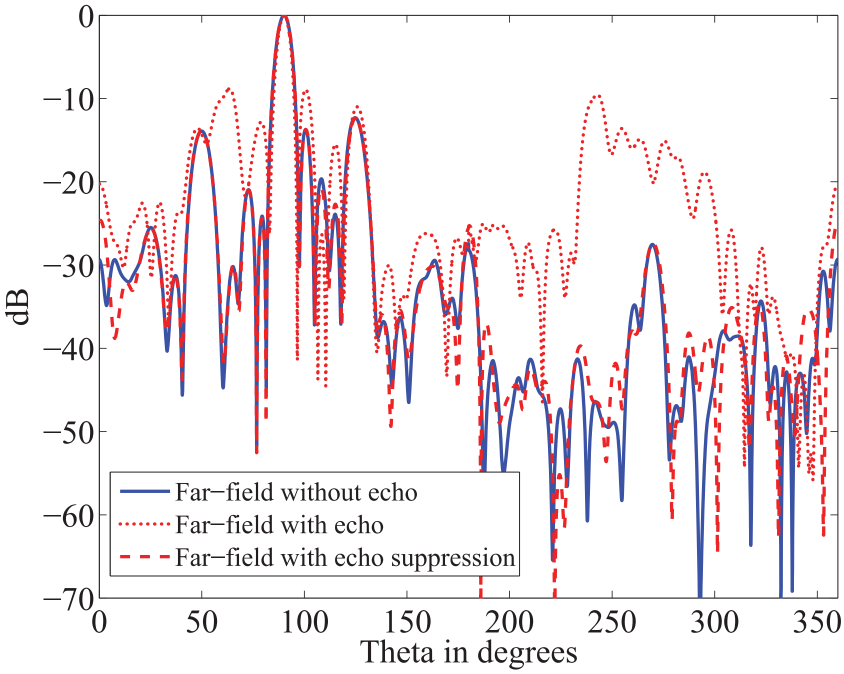

Figure 5.10: E-plane ($\phi = 0°$) cut through the reference far-field, far-field with echo and the far-field with echo suppression for the base station antenna.

5.3 Integration with Spherical Wave Expansion

The multi-probe measurement technique is also integrated with the spherical wave expansion procedure described in [Hansen, 1988] utilizing the discrete Fourier transform (DFT) with first order probe correction. The transmission formula,

$$w(A,\chi,\theta,\phi) = \sum_{\substack{smn\\ \mu}} vT_{smn}e^{im\phi}d^n_{\mu m}(\theta)e^{i\mu\chi}P_{s\mu n}(kA), \tag{5.4}$$

relates the received probe signal, $w(A,\chi,\theta,\phi)$ at the probe location (A,χ,θ,ϕ) to the unknown expansion coefficients, T_{smn}, of the AUT. The probe response constants,

$$P_{s\mu n}(kA) = \frac{1}{2}\sum_{\sigma v} C^{sn(3)}_{\sigma\mu v}(kA)R^p_{\sigma\mu v}, \tag{5.5}$$

take into account the response of the probe to outgoing spherical waves from the AUT, where $C^{sn(3)}_{\sigma\mu v}(kA)$ are the translation coefficients and $R^p_{\sigma\mu v}$ are the receiving coefficients of the probe antenna. Following a series of DFTs for the χ, ϕ and θ integrals and choosing

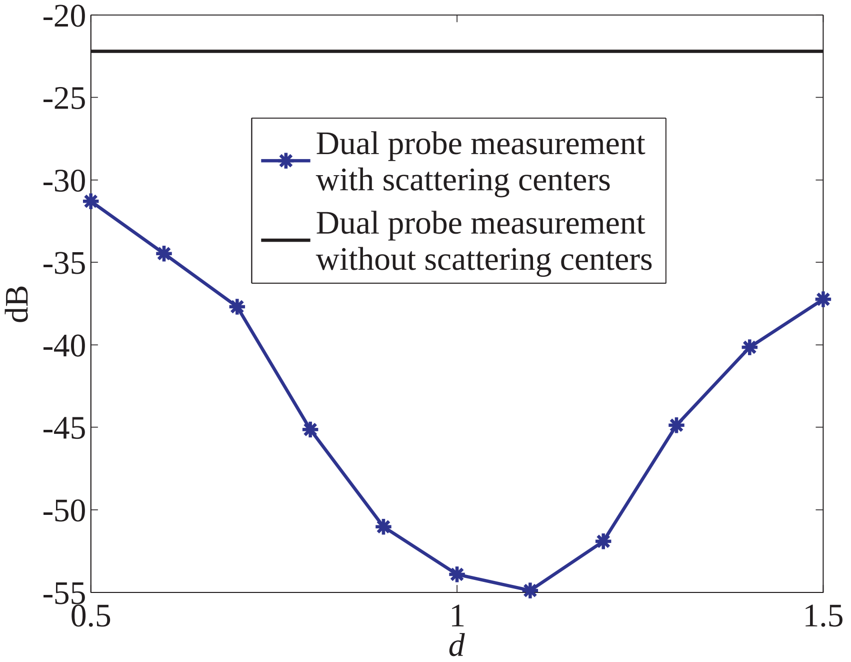

Figure 5.11: H-plane average error in the far field for the base station antenna plotted against errors in the scattering center placement, *d* is the ratio between the scattering centers distances to the true echo locations.

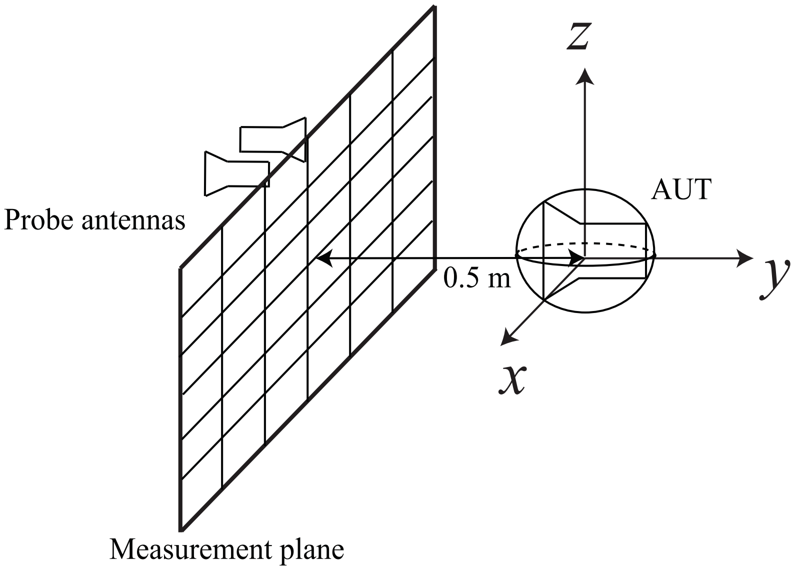

Figure 5.12: Multi-probe measurement for planar set-up. The echo sources should be located behind the measurement plane for the shown measurement technique to be effective. Copyright ©2013, IEEE.

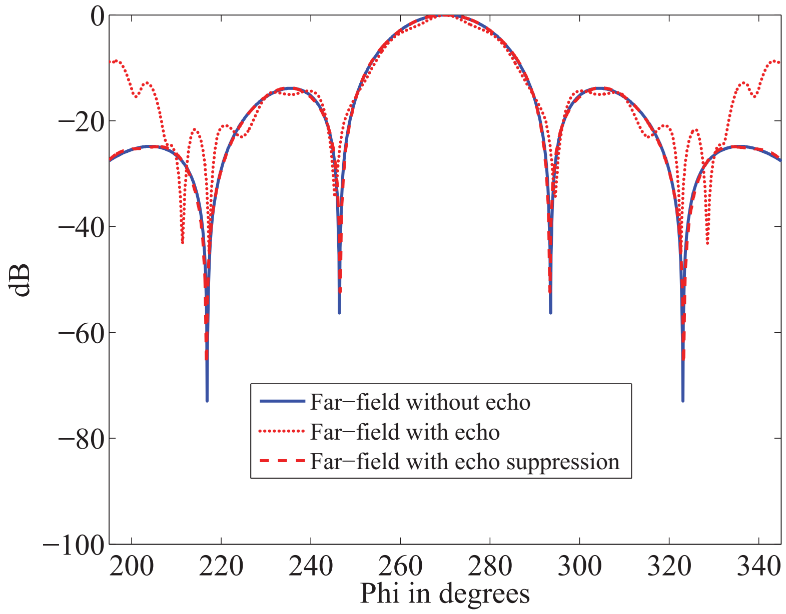

Figure 5.13: H-plane ($\theta = 90^\circ$) cut through the reference far-field and the far-field with and without echo suppression within the valid angle for the 3GHz horn antenna with planar scan geometry.

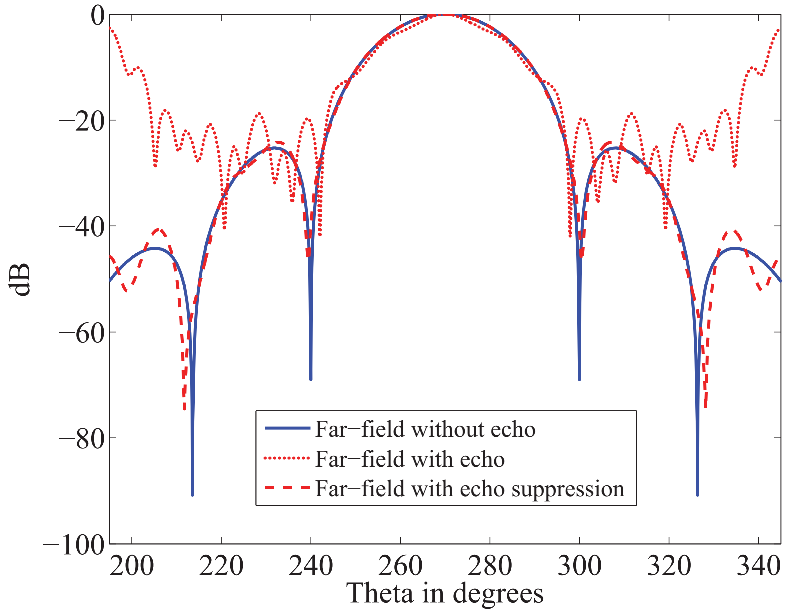

Figure 5.14: E-plane ($\phi = 90^\circ$) cut through the reference far-field and the far-field with and without echo suppression within the valid angle for the 3GHz horn antenna with planar scan geometry.

$\mu = \pm 1$, a system of equations,

$$w^{n}_{\mu m}(A) = v \sum_{s=1}^{2} T_{smn} P_{s\mu n}(kA), \tag{5.6}$$

is set up for the expansion coefficients of the AUT (see section 2.5). In order to integrate the data obtained using the multiprobe measurement procedure, we rewrite Eq. (5.6) with more unknowns,

$$w^{n}_{\mu m}(A) = v \sum_{s=1}^{2} T^{(3)}_{smn} P^{(3)}_{s\mu n}(kA) + v \sum_{s=1}^{2} T^{(4)}_{smn} P^{(4)}_{s\mu n}(kA), \tag{5.7}$$

due to the assumption of incident and outgoing waves. In Eq. (5.7), the coefficients of the outgoing waves, $T^{(3)}_{smn}$ are due to both the AUT and the echo sources whereas the incident waves, $T^{(4)}_{smn}$, are only due to the echo sources. Setting $\mu = \pm 1$ for the received signals from the inward and outward probes results in four equations in four unknown expansion coefficients, i.e. the TE $(s = 1)$ and TM $(s = 2)$ modes of the incident and outgoing spherical waves. In Eq. (5.7), $P^{(3)}_{s\mu n}(kA)$ is as written in Eq. (5.5) and

$$P^{(4)}_{s\mu n}(kA) = \frac{1}{2} \sum C^{sn(4)}_{\sigma\mu\nu}(kA) R^{p}_{\sigma\mu\nu}, \tag{5.8}$$

with

$$[C^{sn(3)}_{\sigma\mu\nu}(kA)]^{*} = (-1)^{s+\sigma} C^{sn(4)}_{\sigma\mu\nu}(kA), \tag{5.9}$$

being the relationship between the translation operators in Eq. (5.5) and Eq. (5.8) [Hansen, 1988]. Since parts of the echo signal are also present in the outgoing waves, the coefficients of the incident waves obtained by solving Eq. (5.7) are subtracted from the coefficients of the outgoing waves to obtain the expansion coefficients of the AUT, i.e.

$$T_{smn} = T^{3}_{smn} - T^{4}_{smn}. \tag{5.10}$$

The performance of the multi-probe technique with spherical wave expansion is tested with the echoic scenario depicted in Fig. 4.5. Near-field data generation is according to the previously described steps concerning the use of inward looking and outward looking probes. However, For the SWE technique, an angular sample spacing of 5.5° is employed along both ϕ and θ directions corresponding to a multipole number of 32. This is because the echo sources removed from the measurement volume increase the field variation over the measurement surface and consequently lead to the field having a higher multipole order. Since the measurement volume serves as a band-limiting filter itself, the size of the measurement volume is used to determine the highest order of the spherical waves to consider. Therefore, when there are no sources outside the measurement sphere, the sampling criteria is determined according to the size of the AUT. However, when there are sources outside the measurement volume, sample spacing should be chosen according to the size of the measurement sphere in order to avoid aliasing. The sampling density is not increased for the plane wave expansion technique since the transformation technique does not need to resolve the individual field modes but determines directly the AUT and the scattering centers plane wave samples. Also, the flexibility to specify various source locations from which plane wave translations are performed, allows the number of unknowns due to these localized sources to remain minimal. SWE is done with respect to the origin for all sources since an efficient implementation for localized sources with SWE has not be reported yet. The advantage of the SWE is that the echo locations are not required for echo suppression. The echo suppression results with multi-probe measurements and SWE are shown in Fig. 5.15 with the main pattern cuts in Fig. 5.16.

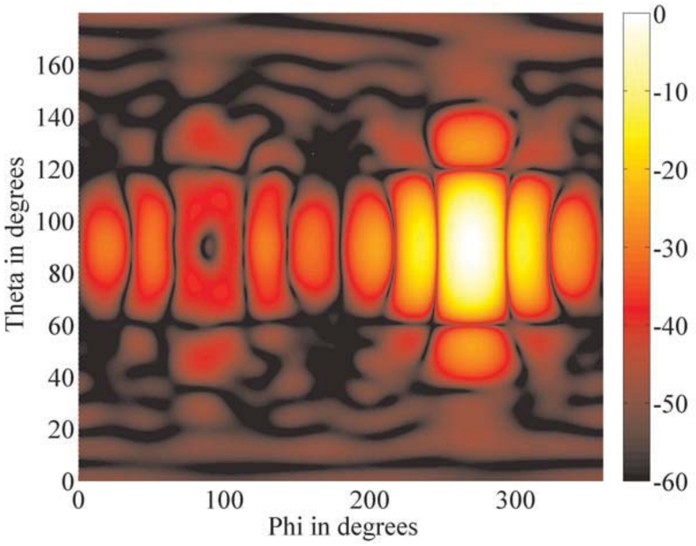

Figure 5.15: Normalized E_ϕ far-field pattern of the 3 GHz horn antenna in dB obtained from the echoic near-field data generated from the scenario in Fig. 4.5. The near-field data is acquired by the multi-probe technique and spherical wave expansion is employed to obtain the far-field pattern.

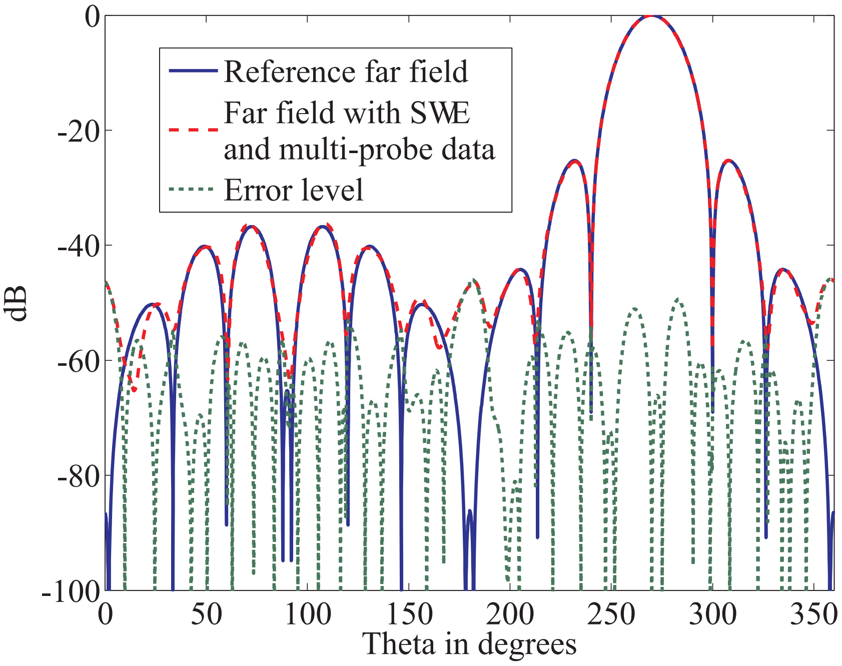

(a) E-plane pattern

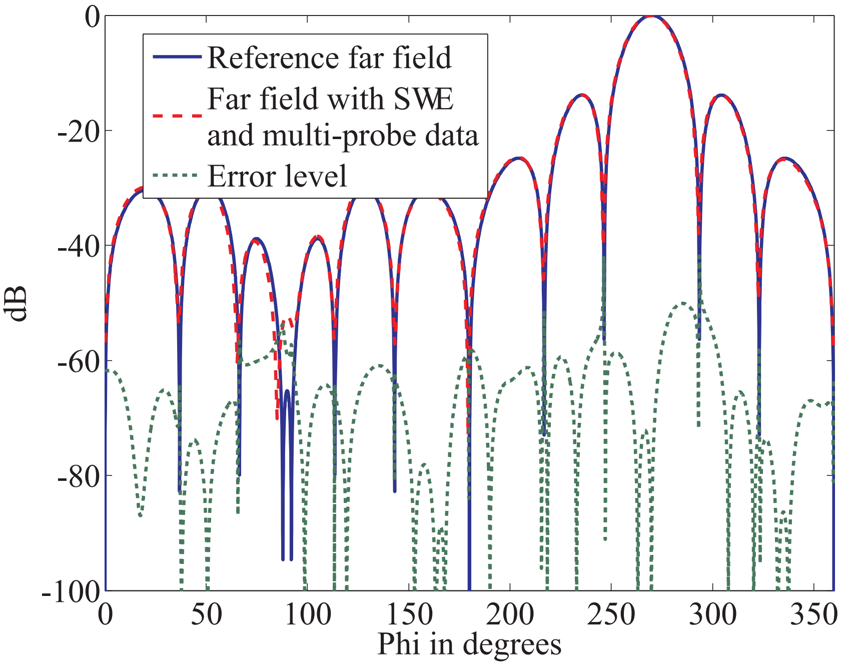

(b) H-plane pattern

Figure 5.16: Far-field cuts for the result of multi-probe measurements with SWE shown Fig. 5.15.

5.4 Summary

In this chapter, a measurement technique for improving the quality of far-field patterns obtained when antennas are measured in non-anechoic environments was presented. The technique involves measuring the AUT with two sets of probe antennas, namely, inward and outward sets of probes. This ensures that enough information is gathered to resolve both the incident and outgoing waves from the measurement volume. The measured echoic near-field data was transformed using the plane wave based NFFFT with the effect of the echo sources integrated by means of auxiliary sources. A method to process multi-probe data with the spherical wave expansion NFFFT was also presented. In this case, incident and outgoing spherical waves are assumed for the involved sources in the inverse problem. The proposed techniques result in a substantial improvement in the far-field pattern obtained from echoic near-field data. Additional measurement samples are required due to the new sets of probe antennas but the technique does not require an increase in the measurement distance or in the sampling density and it is not restricted to canonical measurement geometries. The method is restricted to measurements with a fixed AUT. A great advantage is the adaptability of the scattering centers e.g. in planar measurements the scattering centers amplitude can adapt to the varying echo contributions due to the influence of moving scanner parts.

Chapter 6

Beamforming Filtering of Near-Field Data

Probe antennas operate as a spatial filter on the near-field phase front as well as an angular filter of the far-field [Schejbal et al., 2008, Slater, 1985]. Directive probes reduce the influence of multipath signals by filtering of off-axis signals. In this chapter, a beamforming technique for echo suppression is presented [Yinusa et al., 2014]. The technique is based on combining neighboring near-field signals in order to generate the signal as it would be measured by a probe array. The filtered near-field data is transformed into the far-field by means of the plane wave based NFFFT algorithm. The flexibility of the algorithm allows for probe correction with the far-field pattern of the original probe such that there are no nulls in the utilized probe far-field. A related concept has been investigated in [Hansen and Larsen, 1984] where near-field data was acquired using a directive near-field probe. The motivation there was to suppress echo signals arriving away from the boresight axis by the choice of directive probe antennas in spherical near-field measurements. The authors concluded that probe correction in spherical wave expansion does not amplify signals originating from outside the minimum sphere. The use of such directive probes can, however, lead to higher order interactions between the AUT and the probe. Also, probe nulls may lead to errors either due to probe insensitivity in certain directions in the forward hemisphere or due to numerical errors during probe correction. The latter is true especially for planar and cylindrical near-field measurements [Gregson et al., 2007]. The present technique avoids such limitations since the near-field probe does not have to be particularly directive. It simply generates the near-field data for a large probe by combining signals from a small probe at different positions. Probe correction does not reverse the reduction in multipath signals achieved by the use of a directive probe or beamforming since sources are assumed only within the minimum sphere enclosing the AUT. The benefits of using a directive probe antenna in near-field measurements includes the opportunity to reduce the sampling rate and the reduction of multipath effects on the measurement result because the probe spatially prefilters the measurements [Schejbal et al., 2008, Slater, 1985]. For instance, a sampling rate of 5λ was reported in [Slater, 1985] with high-gain probes. These advantages can, however, be overshadowed by the resulting multiple interaction between the AUT and the probe and errors arising due to the probe insensitivity in certain directions in the forward hemisphere especially for planar and cylindrical measurement.

6.1 Effects of Directive Probes in Planar Near-Field Measurements

In order to highlight the disadvantages of directive probes in planar near-field measurements, the 3 GHz AUT with the dipole distribution shown in Fig. 4.2 is measured with a probe modeled with the dipole distribution shown in Fig. 6.1. The probe has a minimum sphere radius of 0.16 m which is the same as the minimum sphere enclosing the AUT. Simulations are carried out for both spherical and planar measurement geometries. The measurement distance for the spherical set-up is 0.5 m with an angular sample spacing of 5.5° along ϕ and θ directions. Following Eq. (2.41), the multipole order of the translation operator from the AUT to the measurement points was computed as 31 as opposed to 19 given the relatively large size of the probe antenna. The obtained far-field pattern for the 3 GHz AUT using the large probe antenna is shown in Fig. 6.2 and the main far-field cuts in Fig. 6.3. It is observed that the obtained far-field pattern has very low error level because it is close to the AUT reference pattern. For spherical measurements, nulls in the forward hemisphere of the probe do not lead to errors since the main beam of the probe is always focused on the AUT at the origin.

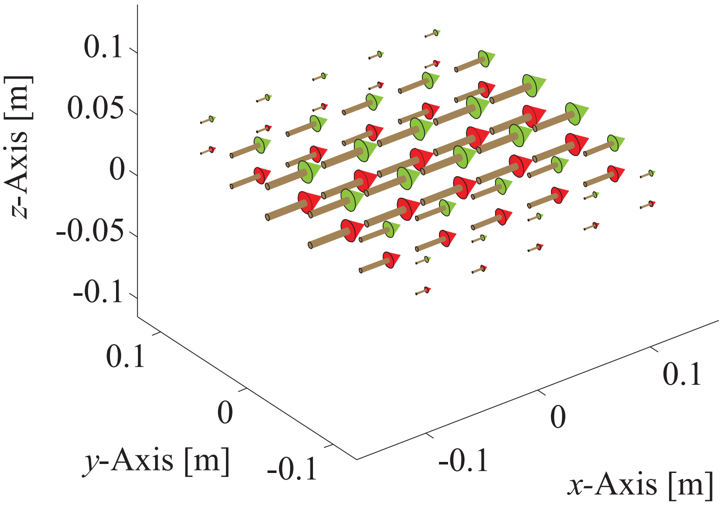

Figure 6.1: Electric dipole distribution used to model the electrically large probe antenna. The length and color of the dipoles represent the relative amplitude excitation and phase, respectively.

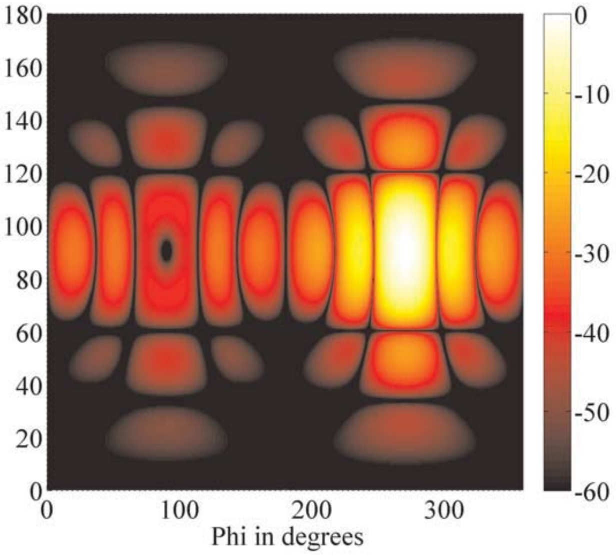

Figure 6.2: Normalized E_ϕ far-field pattern of the 3 GHz horn antenna in dB obtained from a spherical near-field measurement and plane wave based NFFFT. The near-field data has been acquired using the probe antenna shown in Fig. 6.1.

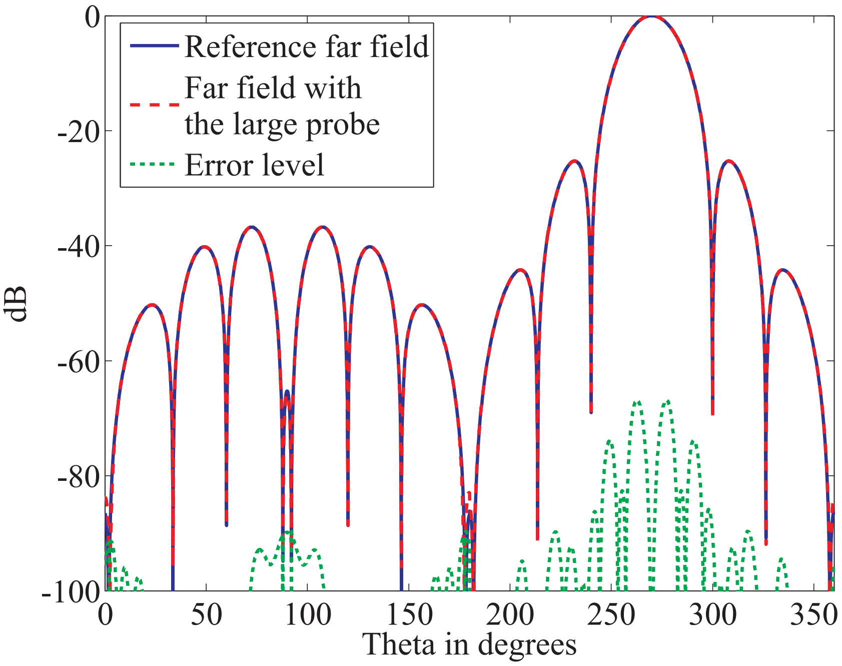

(a) E-plane pattern

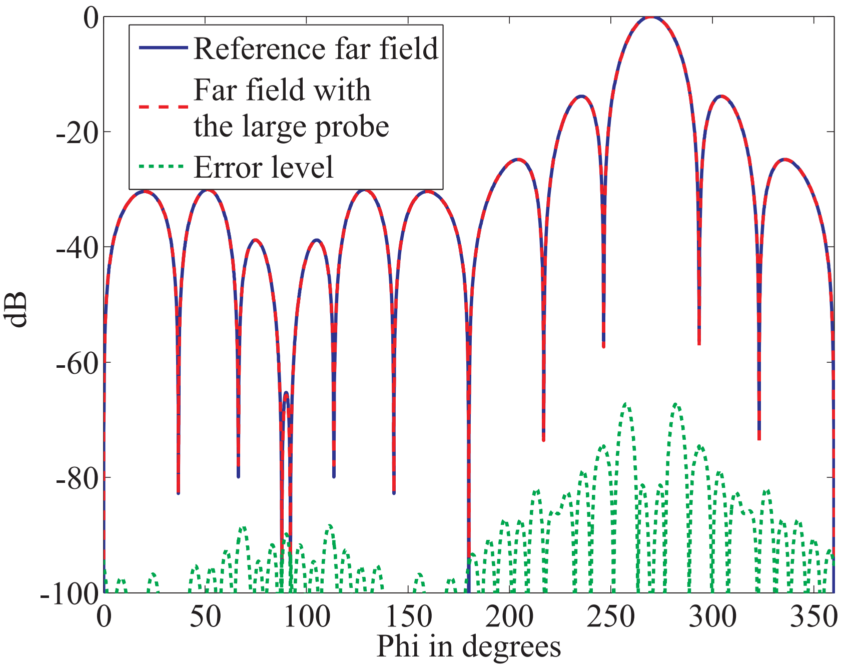

(b) H-plane pattern

Figure 6.3: Far-field cuts for the result shown in Fig. 6.2.

6.2 Beamforming for Planar Near-Field Measurements

For planar measurements, the measurement distance of 0.5 m is chosen with a sample spacing of $\lambda/2$ and a measurement plane size of 4 m x 4 m. The measurement distance is large enough to ensure that the minimum spheres enclosing the AUT and the one enclosing the probe do not overlap. The size of the probe is also considered in the computation of the translation operator similar to the case of a spherical measurement. The probe orientation is fixed throughout the measurement campaign such that the boresight of the probe is always perpendicular to the measurement plane as is common practice in planar measurements. The obtained far-field pattern with the directive probe is shown in Fig. 6.4 and Fig. 6.5.

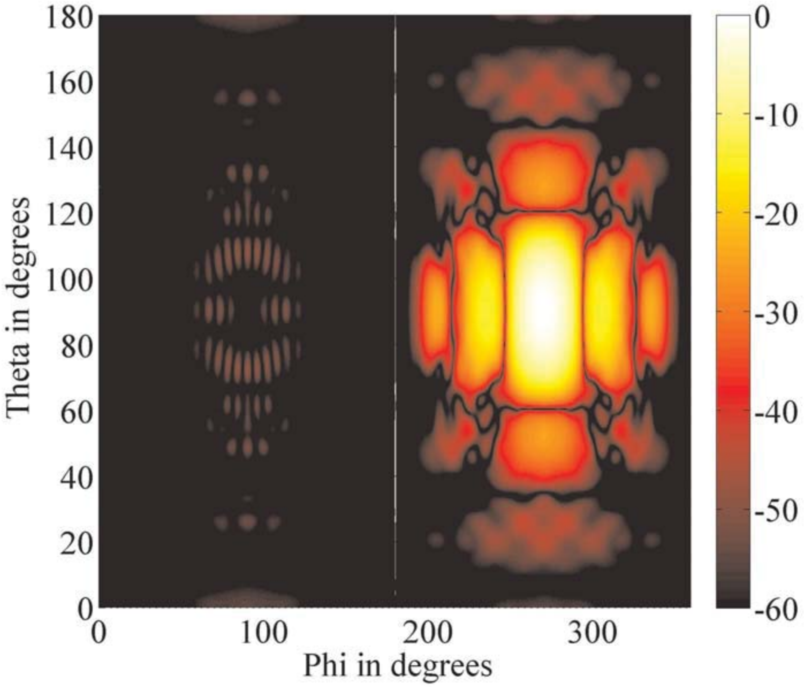

Figure 6.4: Normalized E_ϕ far-field pattern of the 3 GHz horn antenna in dB obtained from a planar near-field measurement and by plane wave based NFFFT. The near-field data is acquired using the probe antenna shown in Fig. 6.1.

It can be observed from the obtained far-field pattern with planar measurement using the directive probe that the error level increased also within the valid angle. This is because of the probe's insensitivity in the directions corresponding to the probe nulls which becomes more significant as the probe moves away from the middle of the measurement plane. The planar measurement is repeated with a smaller probe modeled with the dipole distribution

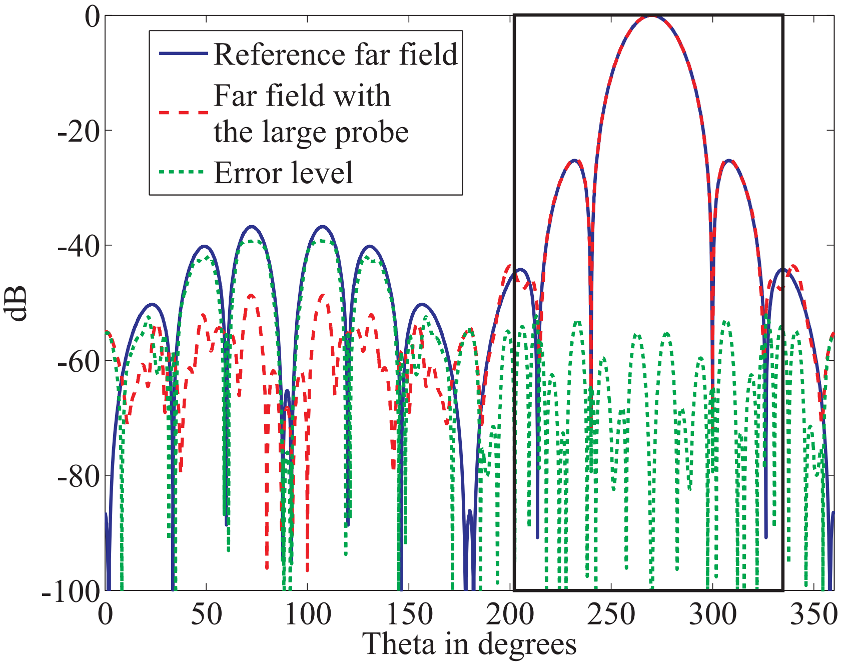

(a) E-plane pattern

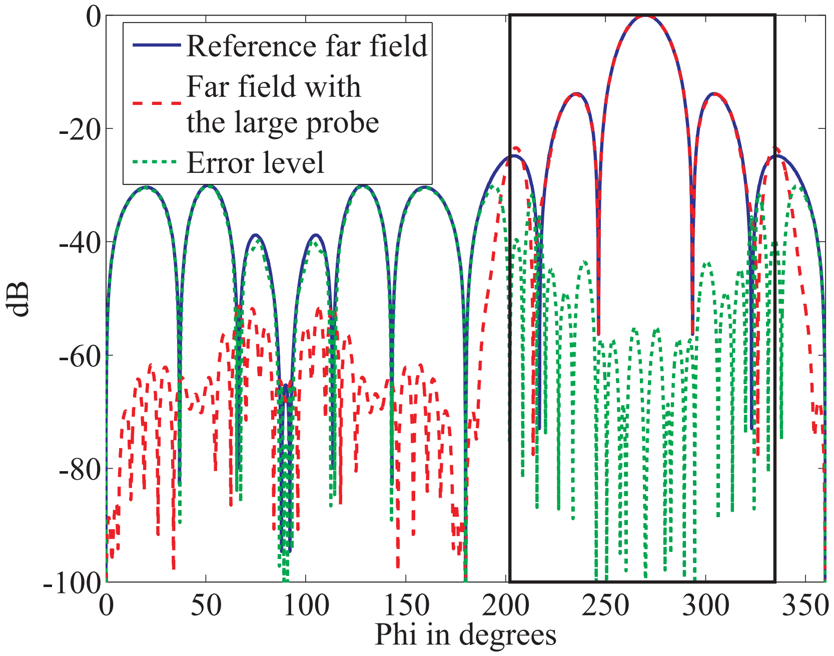

(b) H-plane pattern

Figure 6.5: Far-field cuts of the result shown in Fig. 6.4 with the valid angle shown within the rectangle.

shown in Fig. 6.6 having a minimum sphere radius of 4.67 cm. The obtained far-field in this case is shown in Fig. 6.7 and Fig. 6.8 with relatively low error levels. In order to obtain the spatial filtering advantages of a large probe without the accompanying penalties earlier pointed out, the near-field measurement is done with a small probe. This also has the advantage of reducing the multiple interactions between the AUT and the probe. The signal from the individual measurement points are thereafter combined in a moving average manner such that a signal is generated similar to the signal measured by a larger probe antenna. The individual probe signals are weighted appropriately such that the resulting probe is steered towards the AUT. Fig. 6.9 shows an example of how probe signal combination is performed for two points for planar measurement with 13 points in each direction. In this way, the direct AUT signals are combined constructively while the multipath signals are attenuated. The effect of probe combination is then resolved during probe correction. In order to demonstrate the improvement in SNR due to probe combination, synthetic data is generated using the technique described in [Schmidt et al., 2011] involving electric dipole

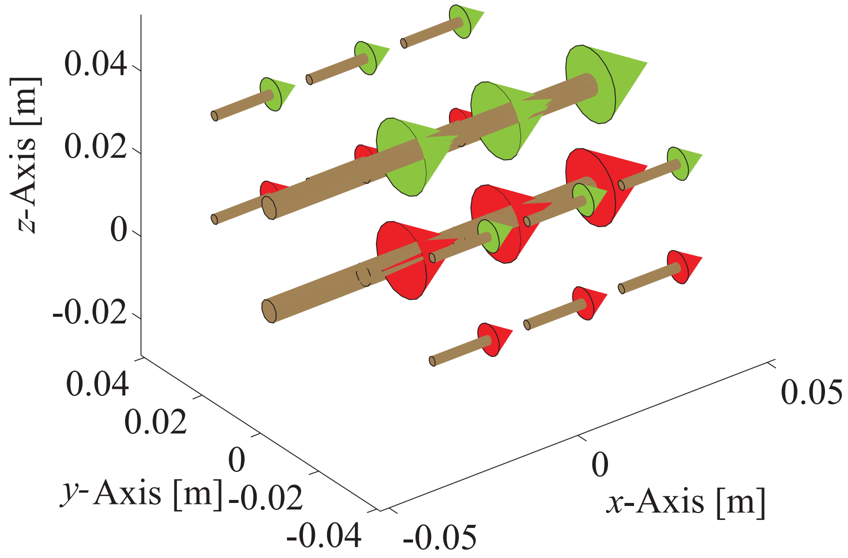

Figure 6.6: Electric dipole distribution used to model the electrically small probe antenna. The length and color of the dipoles represent the relative amplitude excitation and phase, respectively.

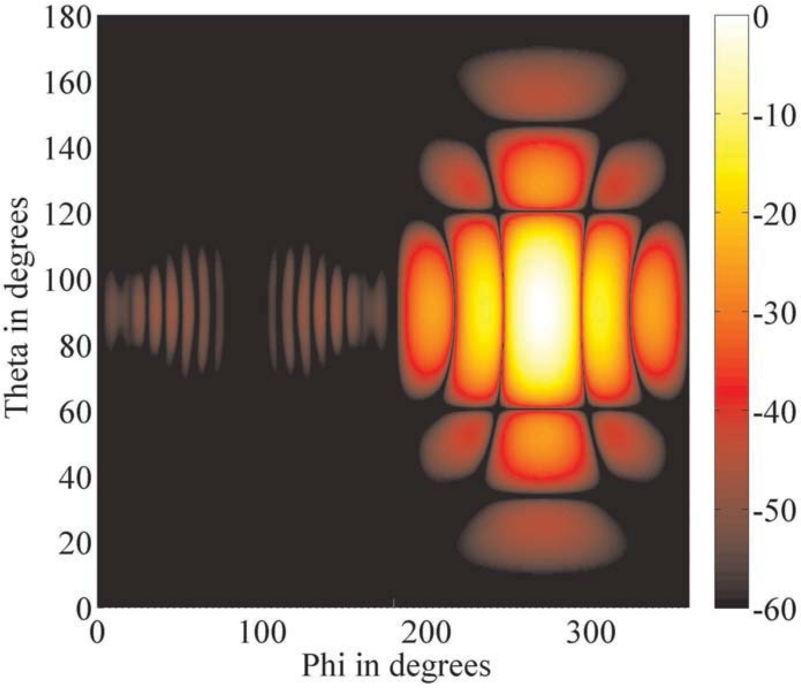

Figure 6.7: Normalized E_ϕ far-field pattern of the 3 GHz horn antenna in dB obtained from a planar near-field measurement and plane wave based NFFFT. The near-field data is acquired using the small probe antenna shown in Fig. 6.6.

distributions for the 3 GHz AUT shown in Fig. 4.2. The scan plane is along the x-z plane at $y = 0.5$ m with a dimension of 4 m x 4 m and a sampling rate of $\lambda/2$. The contributions from the AUT and echo sources towards the measured signal are then computed. For the following example, two echo sources are assumed at locations shown in Fig. 6.10. The signals from the AUT and both echo sources are evaluated for each measurement point including the effect of the measurement probe. The signal-to-echo ratio

$$\mathrm{SER}(x,y,z) = 20\log_{10}\frac{\|U_{\mathrm{AUT}}(x,y,z)\|}{\|U_{\mathrm{Echo}}(x,y,z)\|} \tag{6.1}$$

is computed by taking the ratio of the direct AUT signal at each measurement point to the echo signals. The SER is computed with and without beamforming and the SER gain over the measurement plane for the scenario depicted in Fig. 6.10 is shown in Fig. 6.11. The filtered near-field data is transformed into the far field by means of the plane-wave based NFFFT algorithm described in Chapter 2. The formulation of the algorithm does not assume any particular measurement geometry or probe order. Moreover, in line with

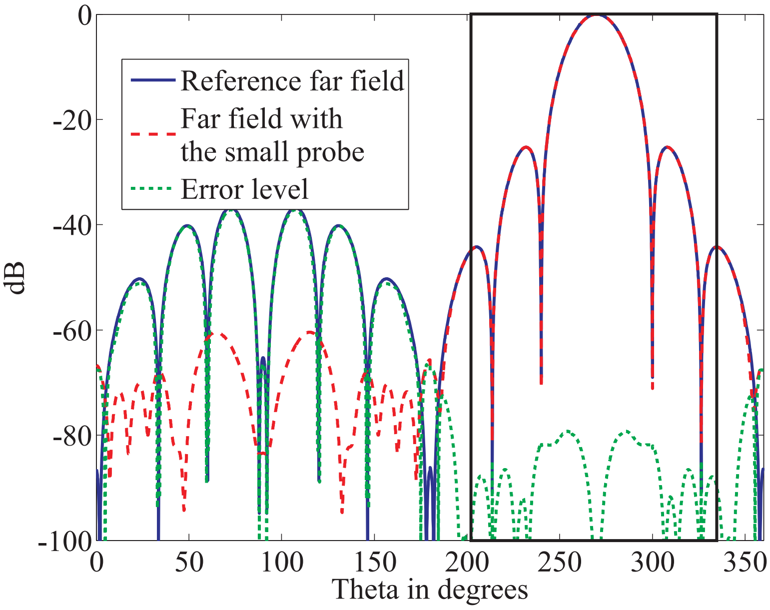

(a) E-plane pattern

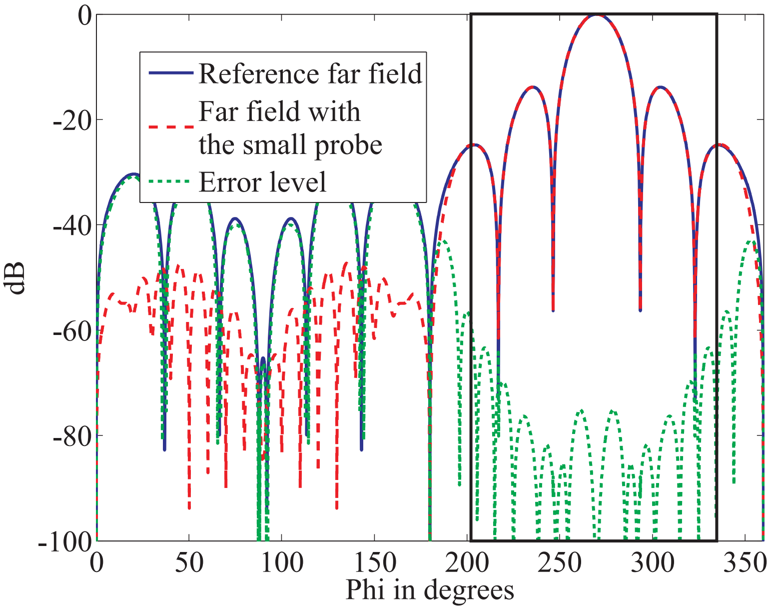

(b) H-plane pattern

Figure 6.8: Far-field cuts of the pattern in Fig. 6.7 with the valid angle shown within the rectangle. The improvement in the error levels as compared to the results in Fig. 6.5 is due to the sizes of the utilized probes.

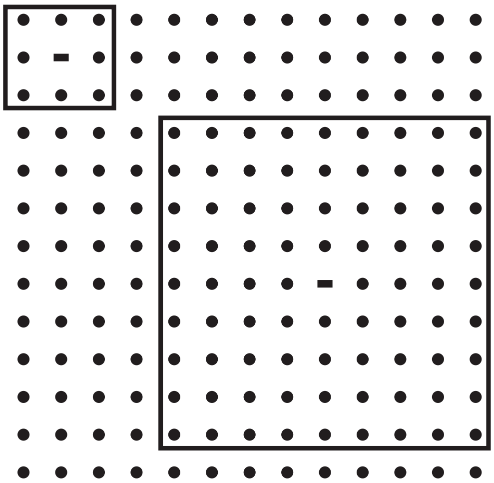

Figure 6.9: Scheme of measurement point combinations. The new signals for points denoted with a line are obtained by a weighted sum of the signals at the points denoted with the same color.

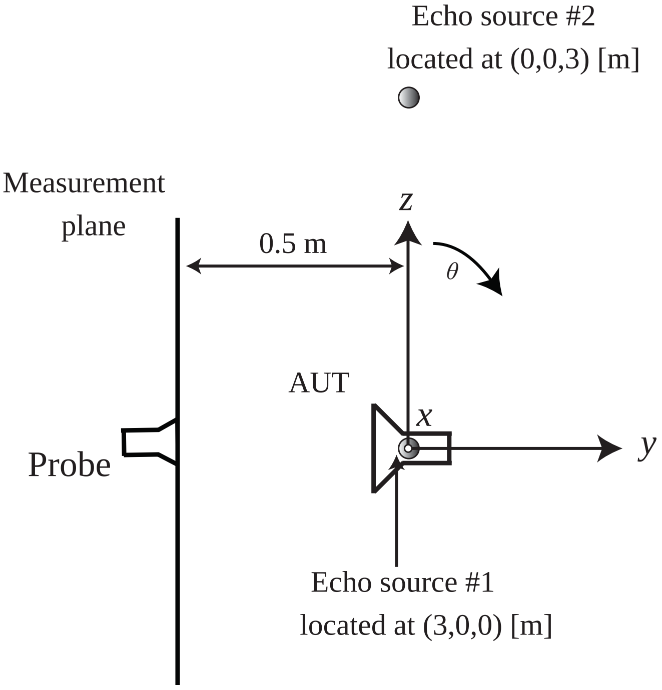

Figure 6.10: Set-up for planar echoic scenario.

Eq. (2.39), different probes with arbitrary probe orientations can be used for different measurement points within the same data set. These features allow for a near-field far-field transformation of the data obtained by combining neighboring measurement points. Plane wave translations and probe correction are performed with respect to the individual data

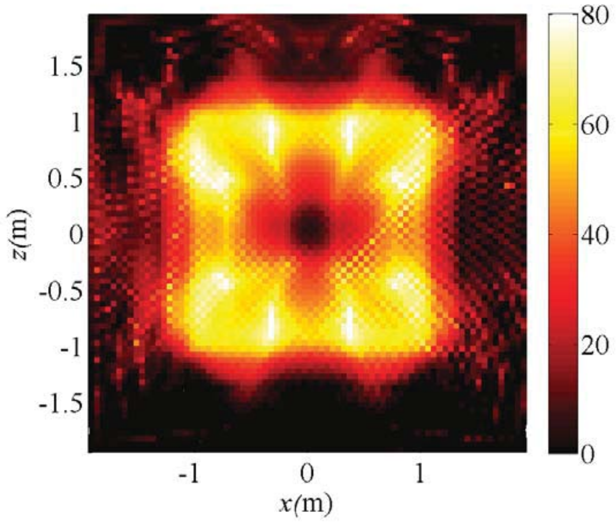

Figure 6.11: SER gain in dB over the measurement plane between the data with probe combination and the data without probe combination.

points and signal combination is done at the lowest level i.e. after probe correction. This means that the utilized probe pattern is that of the actual small probe and not the pattern of the combined probe. In this way, the spatial filtering advantages of using a directive probe are obtained without the penalty of dealing with numerical errors due to nulls in the probe far-field pattern. One would think that probe correction would reverse the gains in echo suppression by amplifying the off-axis signals but this is not the case since sources are assumed only within the minimum sphere enclosing the AUT. The linear system of equations in Eq. (4.1) can be rewritten in this case as

$$\mathbf{P}^{-1}\boldsymbol{U}'_{\mathrm{AUT}}+\mathbf{P}^{-1}\boldsymbol{U}'_{\mathrm{echo}} = -\mathrm{j}\frac{\omega\mu}{4\pi}\mathbf{P}^{-1}\mathbf{C}\cdot\tilde{\boldsymbol{J}}', \tag{6.2}$$

where each row of the matrix $\mathbf{P}^{-1}$ specifies the filtering function for the corresponding measurement point. The idea of applying $\mathbf{P}^{-1}$ to the measurement data is that it reduces the ratio of $\boldsymbol{U}'_{\mathrm{echo}}$ to $\boldsymbol{U}'_{\mathrm{AUT}}$ when carefully chosen to utilize the a priori knowledge about the configuration of the sources. This means that the combined points in $\boldsymbol{U}'_{\mathrm{echo}}$ combine destructively and $\boldsymbol{U}'_{\mathrm{AUT}}$ combine constructively. The destructive combination in $\boldsymbol{U}'_{\mathrm{echo}}$ is not recovered by the application of $\mathbf{P}^{-1}$ to $\mathbf{C}$ on the right hand side. This is because the matrix $\mathbf{C}$ contains a spatial filter due to the integration of a minimum sphere enclosing the AUT in its formulation. The obtained far field with echo and the far field with beamforming obtained for the scenario in Fig. 6.10 are shown in Fig. 6.12 and Fig. 6.13, respectively. The results with beamforming show a lower error level when compared to the far field obtained from non echoic near-field data.

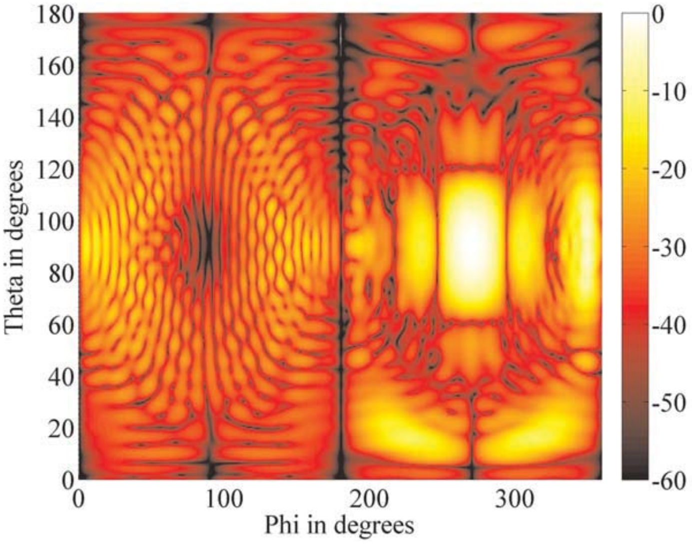

Figure 6.12: Normalized E_ϕ far-field pattern of the 3 GHz horn antenna in dB obtained from the echoic near-field data generated from the scenario in Fig. 6.10.

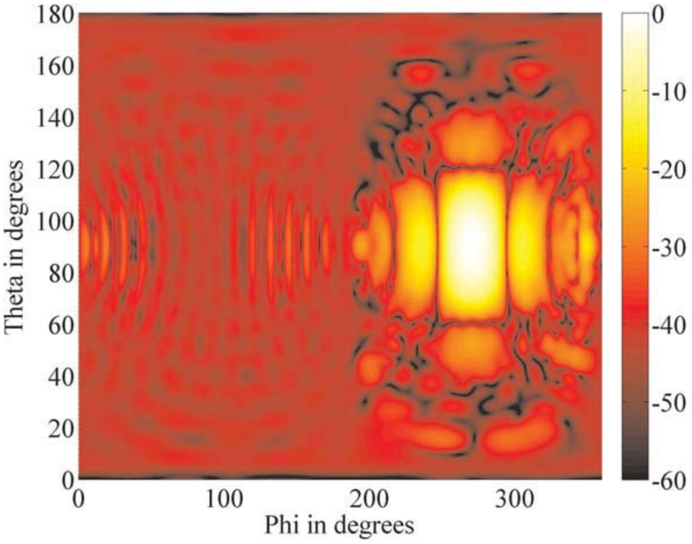

Figure 6.13: Normalized E_ϕ far-field pattern of the 3 GHz horn antenna in dB obtained from the echoic near-field data generated from the scenario in Fig. 6.10. The signals are combined before applying the NFFFT algorithm.

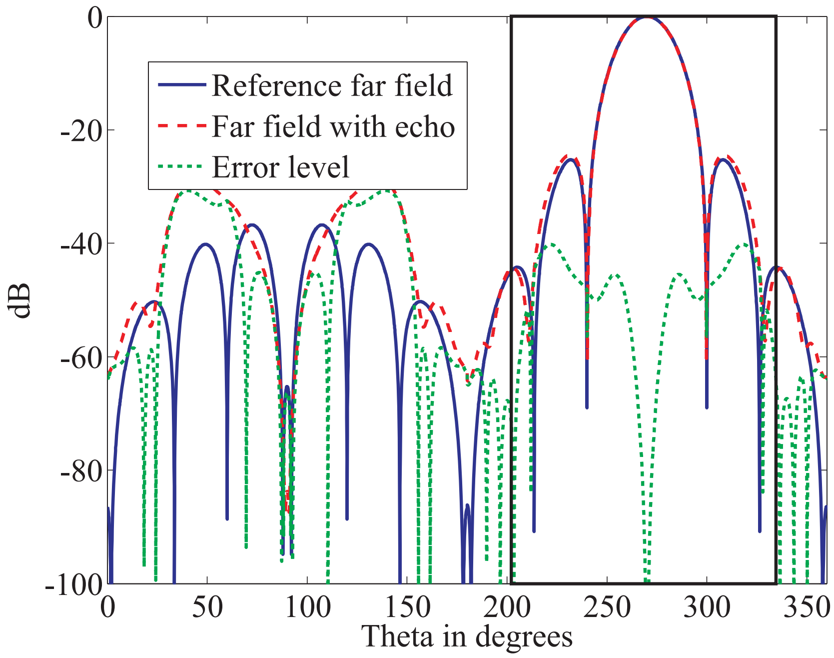

(a) Without beamforming

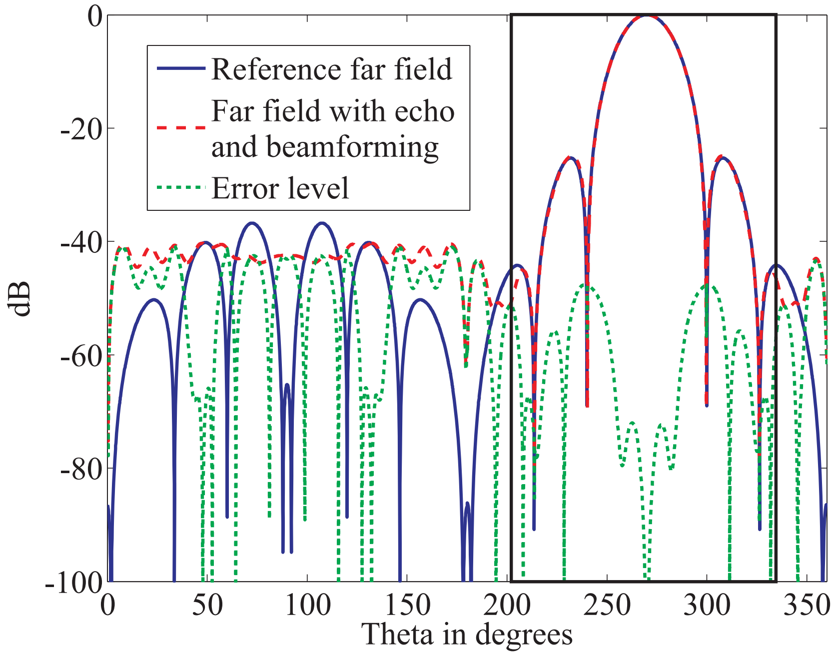

(b) With beamforming

Figure 6.14: E_ϕ E-plane pattern of the 3 GHz AUT from the echoic near-field data generated from the scenario in Fig. 6.10.

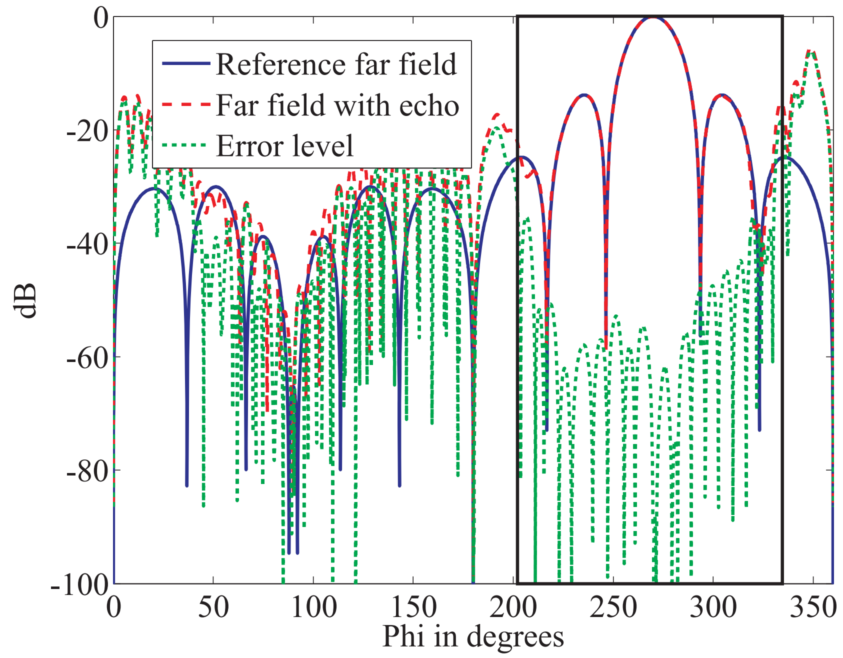

(a) Without beamforming

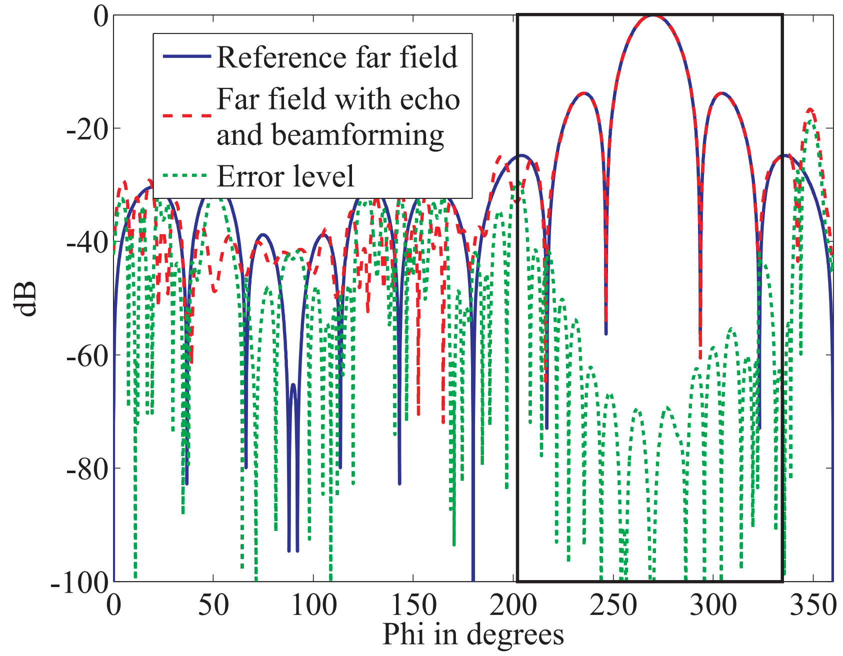

(b) With beamforming

Figure 6.15: E_ϕ H-plane pattern of the 3 GHz AUT from the echoic near-field data generated from the scenario in Fig. 6.10.

6.3 Summary

In this chapter, a beamforming technique for echo suppression in near-field measurements was presented. The technique depends on the combination of neighboring measurement signals to generate signals with lower echo contributions. Combination of measured signals has the spatial filtering advantages of a highly directive probes without the disadvantages of multiple interactions between the AUT and the probe. The far field obtained from the combined signals show a better accuracy when compared to the far field obtained by a direct application NFFFT algorithm on echoic measurement data.

Chapter 7

Statistical Techniques

Time domain techniques for echo suppression in antenna measurements were introduced in Chapter 3. They depend on a broadband measurement of the AUT to obtain a frequency domain characterization of the multipath environment. Echo suppression is accomplished in those techniques by going back and forth between time and frequency domains and recognizing the difference in propagation time between the direct AUT signal and multipath signals. Two major drawbacks for such techniques include the increase in measurement time needed for an accurate broadband measurement and the need for a broadband AUT and probe. The latter can be solved by using averaging techniques whereby the AUT is measured at several different measurement distances. In planar measurements, for example, a well-known averaging technique used to reduce multiple reflection between the AUT and the probe is to perform the planar measurement on two to five closely spaced planes over a distance of $\lambda/2$. The measurements on the planes are then averaged in order to obtain near-field data with reduced contributions from multiple reflections [Newell, 1988]. Similar techniques can also be used to improve the quality of far-field patterns obtained from echoic near-field measurements.

7.1 Multiple Measurement Distances

For closed measurement surfaces such as the spherical measurement geometry, the obtained far-field pattern from near-field data on the measurement surface is independent of the measurement distance when factors such as multiple reflections are not taken into account. In other words, once the minimum sphere enclosing the AUT and the one enclosing the probe are separated, the same far-field pattern of the AUT can be obtained from the near-field measurement regardless of the choice of the measurement distance. However, for sources outside the measurement volume, the measured components vary depending on the measurement distance. Typically, the larger a measurement volume, the higher the number of modes that are captured by a measurement over that measurement surface for sources outside the volume. This is because the measurement volume itself acts as a spatial filter for the radiated field from the source. For sources within the measurement volume, it is clear that the measurement is able to capture all the modes generated by the sources. Measurement on several measurement spheres, therefore, measures the same spectral components of the AUT but different components of the echo sources. For spherical measurement, for example, the AUT is measured over several concentric spheres as shown in Fig. 7.1. This can be accomplished by repeating the measurement with the probe at different radial distances for the traditional roll-over-azimuth positioners where the AUT is rotating and the probe is usu-

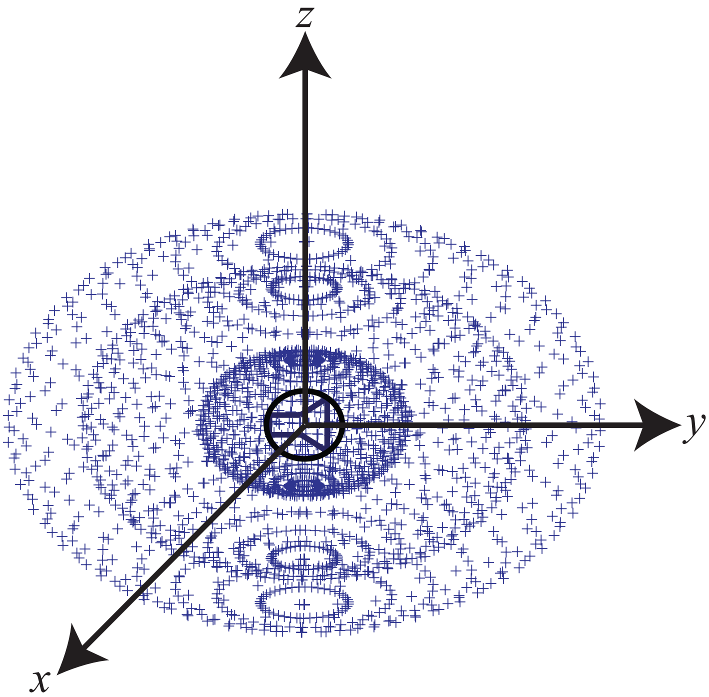

Figure 7.1: Near-field measurements on several spheres obtain varying modal contents of the echo signals. Averaging the obtained far-field pattern results in echo suppression as the echo signals vary depending on the measurement radius.

ally fixed. This naturally increases the required measurement time. Once the near-field data on these concentric spheres are measured, NFFFT is performed on the resulting data with the plane wave based NFFFT algorithm to obtain the far-field pattern. Since the resulting measurement data is on an arbitrary measurement surface, traditional modal transformation techniques are not well suited for the transformation process. For non-closed measurement geometries, the far-field pattern obtained from a particular near-field measurement usually depends on certain choices made during the near-field acquisition. For example, in planar near-field measurement, the valid angle depends on the size of the measurement plane and on the measurement distance. In cylindrical measurements, the valid angle depends on the radius and the height of the cylindrical surface over which the near field is acquired. In these two cases, the measurement distance and the extent of the measurement surface would have to be optimized for each measurement set-up such that the valid angle is the same for each of the multiple measurements. The averaging technique was tested using echoic measurement data with a Rohde & Schwarz HF906 double-ridged waveguide horn antenna shown in Fig. 7.2 as the AUT [Rohde & Schwarz, 2014]. The measurement was carried out at a frequency of 5.9 GHz. The AUT was mounted on a standard roll-over-azimuth positioner such that the movements during the measurement duration of a single polarization is done by the AUT and the probe remains fixed. The only movement involving the probe is the rotation of 90° to generate a second independent measurement. The measurement distance is 2.7 m with an equal sample spacing of 2.5° along θ and ϕ directions. The radius of the minimum sphere enclosing the AUT is 30 cm which corresponds to a multipole order of 50

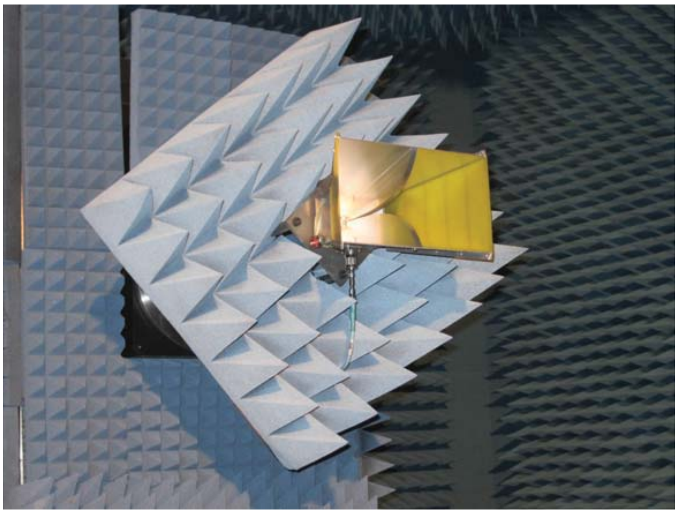

Figure 7.2: Double-Ridged Waveguide Horn Antenna HF906 as AUT.

for the translation operator between the AUT and the measurement points at an accuracy of 10^{-3} for the translation operator. This configuration is shown in Fig. 7.3. The normal system of equations resulting from the plane wave translations was solved using the GMRES algorithm until a relative residual of 10^{-5} was reached. The convergence is shown in Fig. 7.4 and the obtained far-field pattern which is also used as reference for subsequent echoic measurements is shown in Fig. 7.5.

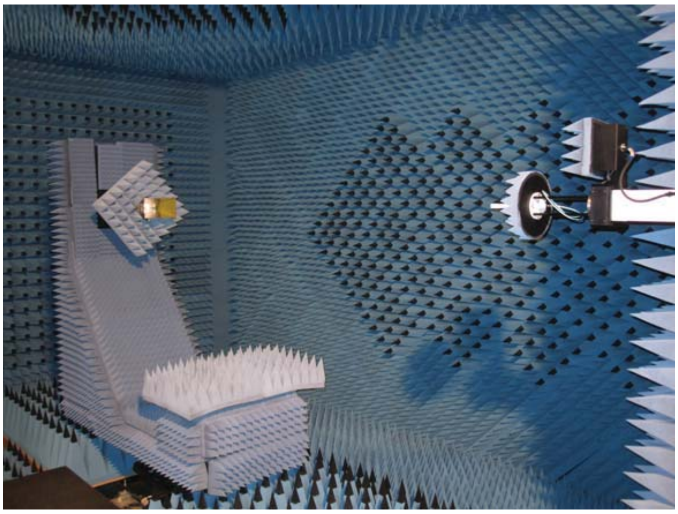

Figure 7.3: Spherical measurement set-up with the double ridged broadband horn antenna HF906 used as AUT. Rotation over the complete measurement sphere is achieved by movements of the AUT and the measurement radius is tuned by moving the probe.

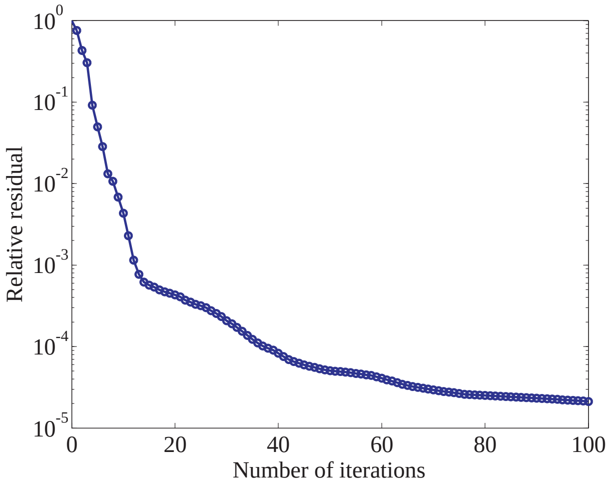

Figure 7.4: Convergence of the GMRES algorithm for the measurement set-up in Fig. 7.3.

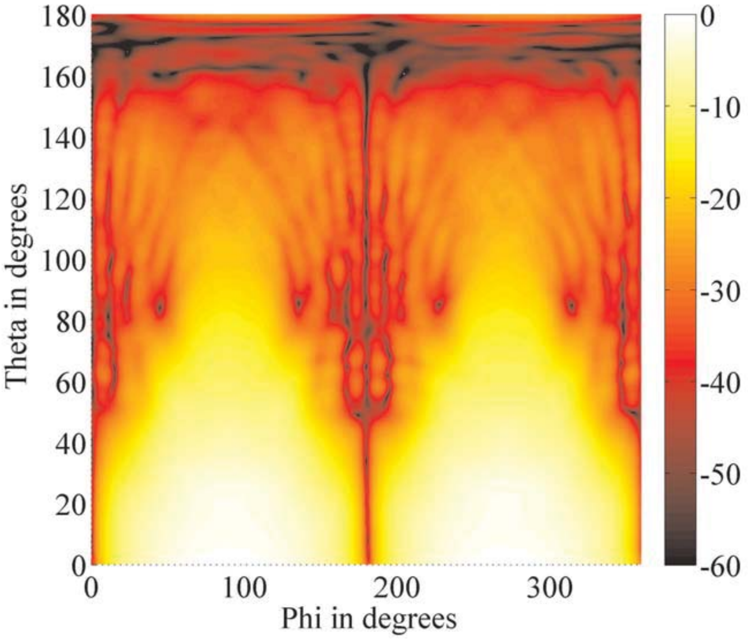

(a) E_θ pattern of the HF906 AUT at 5.9 GHz.

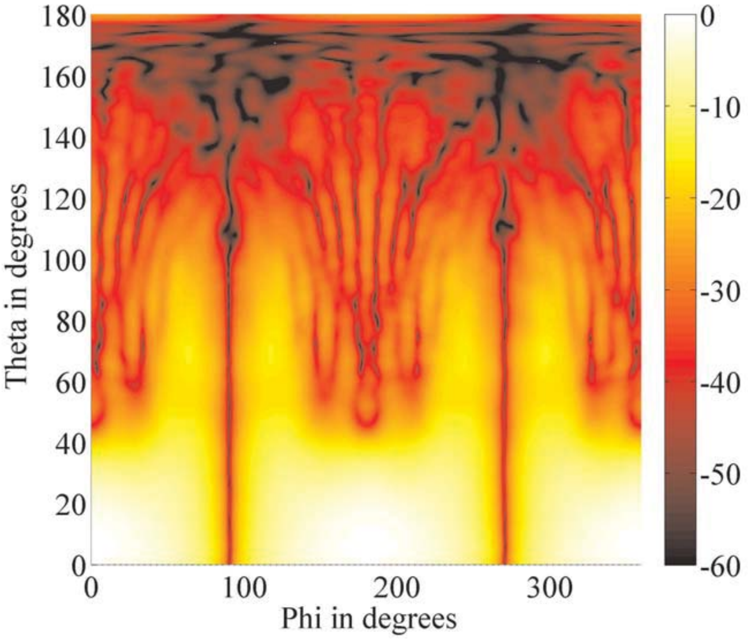

(b) E_ϕ pattern of the HF906 AUT at 5.9 GHz.

Figure 7.5: Far-field patterns of the HF906 AUT at 5.9 GHz obtained from the near-field data measured with the set-up in Fig. 7.3.

To generate the near-field data with echo signals, a metallic bucket was introduced into the measurement room as shown in Fig. 7.6 and the near-field data with echo signals was obtained. The probe is moved farther away from the AUT and another scanning was carried out to produce the measurement data for a second measurement sphere. This process is repeated for five different positions of the probe antenna with an increment of 0.05 m (1.0λ) in the measurement distance such that measurement data is obtained for five concentric spheres. The sampling criteria is fulfilled for each of the measurement spheres such that the number of samples is increased by a multiple of the number of measurement radii. NFFFT is then performed for the data on the five concentric spheres. The number of measurements is dictated by several factors such as measurement time and maximum distance over which the probe can be displaced. Since the additional measurements serve as additional constraints for the NFFFT, more radial observations provide a better echo suppression performance. The far-field result with the metallic bucket for near-field measurement on a single measurement sphere with radius of 2.7 m is shown in Fig. 7.7(a) and Fig. 7.8(a) where the effects of echoes from the metallic bucket are clearly visible. Fig. 7.7(b) and Fig. 7.8(b) show the corresponding results for the far-field obtained from near-field mea-

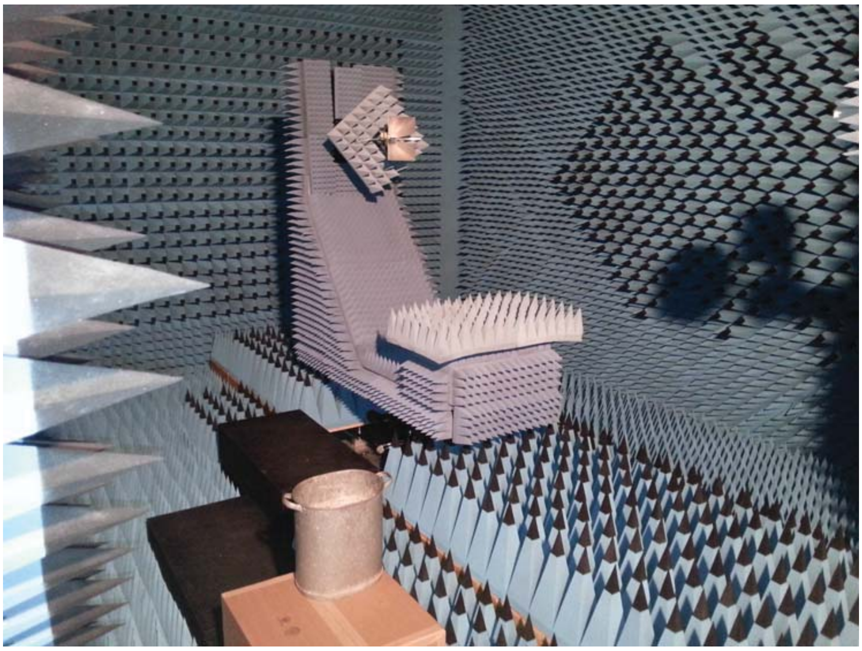

Figure 7.6: Metallic bucket used to generate echo signals.

surements on five concentric spheres. It can be seen that the multiple measurement resulted in a lower error level when compared to the results from a single sphere. The echo suppression improved with increasing number of measurement spheres but the measurement was limited to five due to positioner constraints.

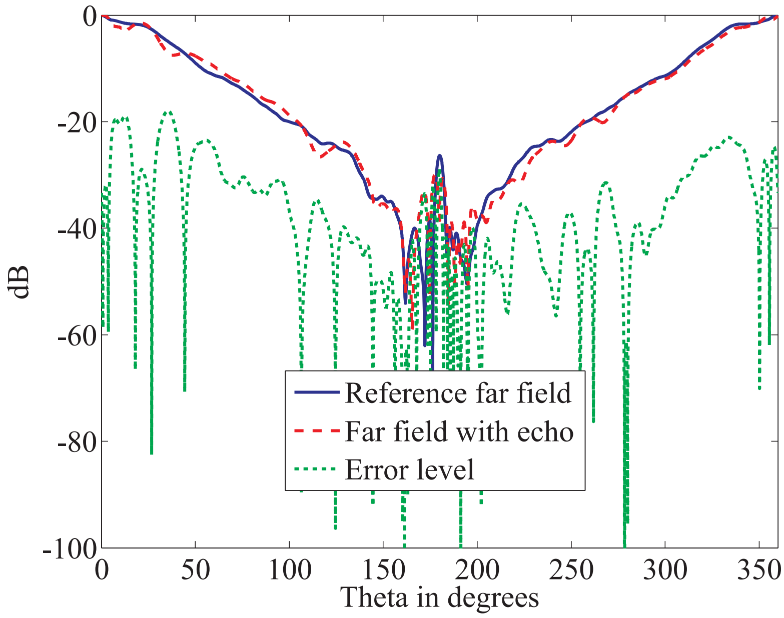

(a) Obtained from near field data on a single measurement sphere.

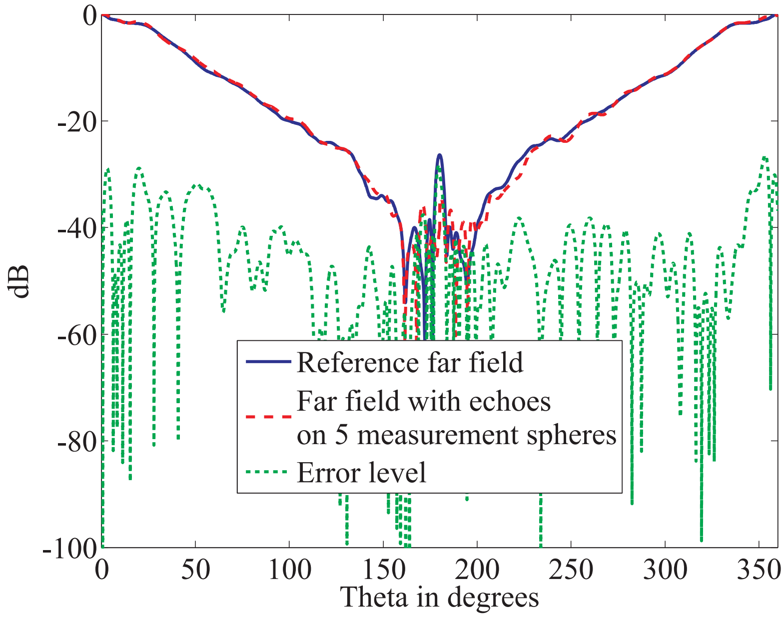

(b) Obtained from near field data on five measurement spheres.

Figure 7.7: Phi = 90° cut for E_θ for the measurement set-up in Fig. 7.6

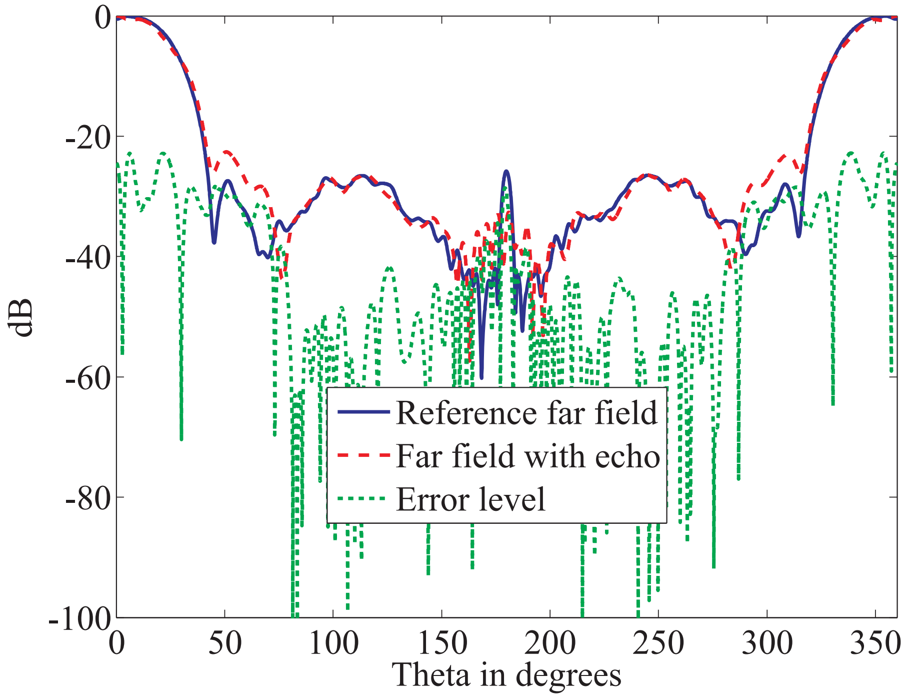

(a) Obtained from near field data on a single measurement sphere.

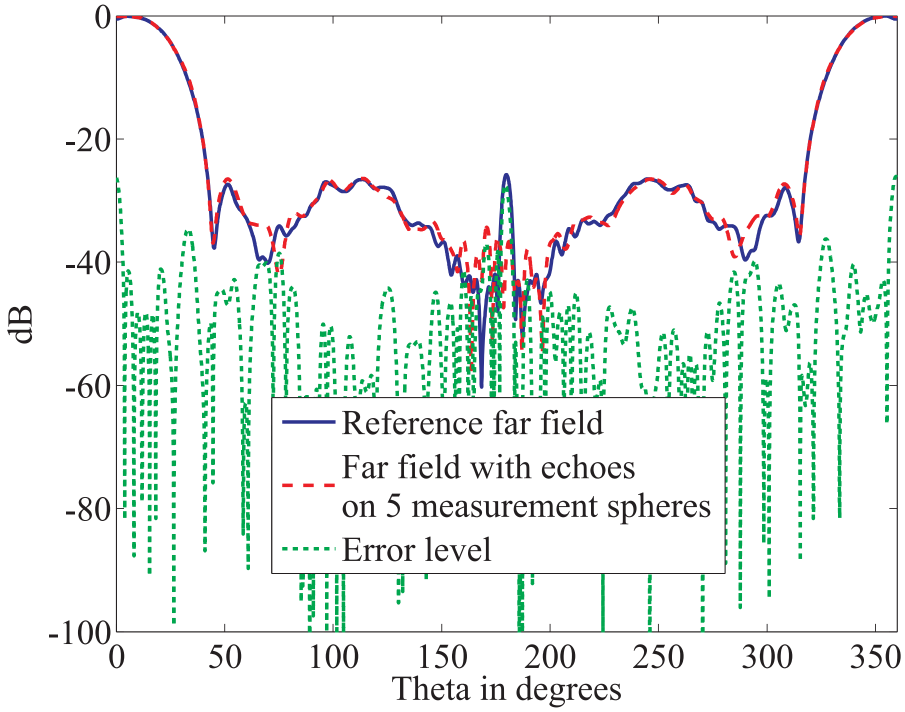

(b) Obtained from near field data on five measurement spheres.

Figure 7.8: Phi = 0° cut for E_ϕ for the measurement set-up in Fig. 7.6

Example 2: HF906 at 3 GHz with metal plate

A second example for echo suppression performance of the multi-distance measurement technique was investigated using the HF906 broadband antenna as AUT. In this example the near-field measurement has been carried out at a frequency of 3 GHz with a sampling rate of 4° along both ϕ and θ directions and the probe is a NSI WR284 probe [Nearfield Systems, Inc., 2014]. The probe was fixed during the measurement of a complete polarization with the AUT rotating. Echo signals were introduced to the measurement by means of a metal plate placed in the measurement room as shown in Fig. 7.9 and Fig. 7.10. The metal plate has a dimension of (1.03 m x 1.03 m) and it is fixed throughout the measurements. The measurement distance for the reference measurement was set at 2.52 m. In order to obtain the far-field pattern, the plane wave based NFFFT algorithm was applied to the measured near-field data. For this purpose, a multipole order of 29 was assumed for the AUT resulting in a plane wave sample spacing of 6° at an accuracy of 10^{-3}. The normal equation resulting from the linear system of equations was solved iteratively using the GMRES algorithm until a relative residual of 10^{-5} was reached. The obtained E_θ and E_ϕ far-field pattern from the reference measurement are shown, respectively, in Fig. 7.11 and Fig. 7.12 and they are also used as reference for the echo suppression results.

In order to observe the effect of the metal plate on the measurement result, the far-field pattern from near-field measurement with the metal plate on a single measurement sphere ($r = 2.52$ m) was obtained using the same settings for the NFFFT algorithm. The results are shown in Fig.7.13(a) and Fig.7.14(a) where the main cuts are compared to those of the reference far-field pattern. The effects of the echo signals can be seen clearly from the relatively high error levels between the obtained far-field patterns with echoes and the reference far-field. In order to generate measurement data for additional measurement spheres, the measurement distance was incremented by 0.05 m (0.5λ). Measurement data was generated with measurement distances of 2.52 m, 2.57 m, 2.62 m, 2.67 m, 2.72 m with the same sample spacing on each of the measurement spheres. This resulted in 5 times the number of measurement samples compared to the initial reference measurements. The plane wave based NFFFT algorithm was then applied to the multiple distance measurement data with the same criteria as previously explained. Additional plane wave translations are performed due to the additional measurement samples. The resulting far-field patterns are shown and compared to the reference far-field pattern in Fig. 7.13(a) and Fig. 7.13(a). The echo suppression capabilities of the multiple sphere measurement can be clearly seen from the reduced error levels as compared to the results from a single sphere near-field data.

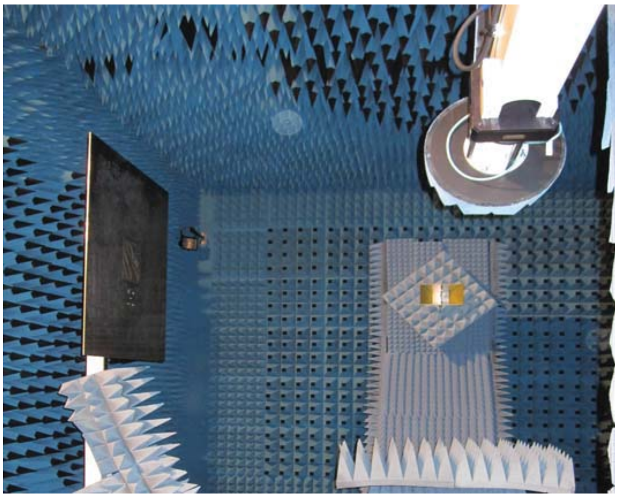

Figure 7.9: Spherical measurement set-up with the double ridged broadband horn antenna HF906 used as AUT. Echoes are generated by means of the metal plate.

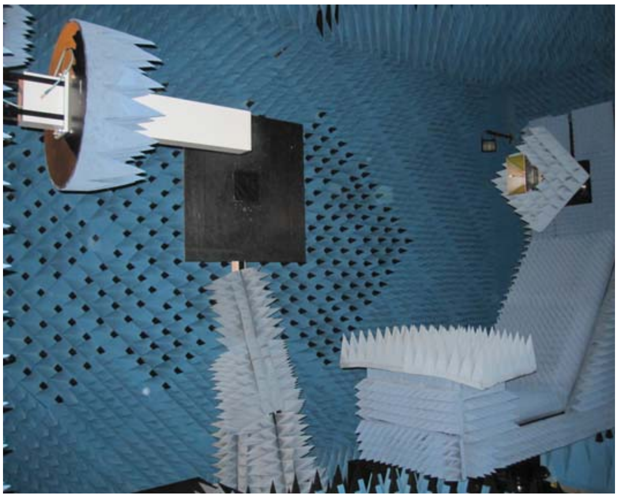

Figure 7.10: Side view of the spherical measurement set-up with the double ridged broadband horn antenna HF906.

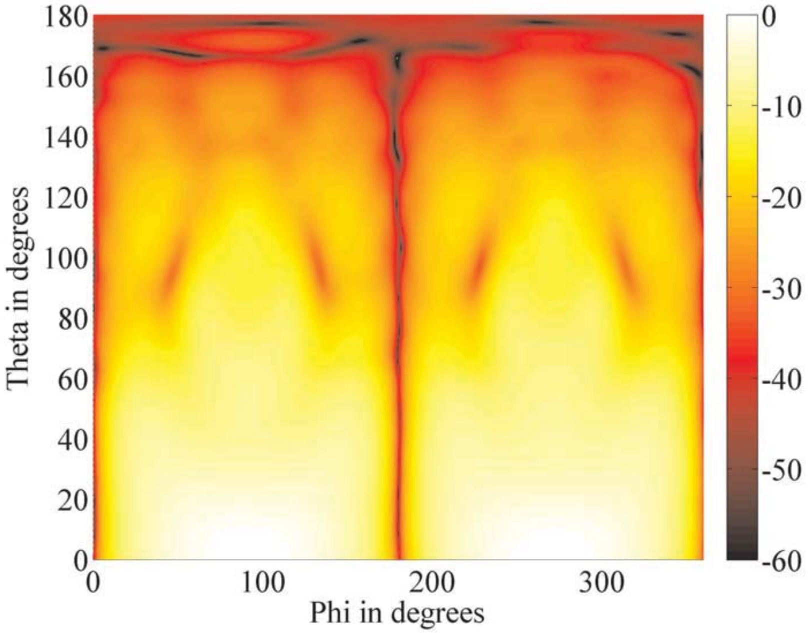

Figure 7.11: Normalized E_θ far-field pattern of the HF906 broadband antenna at 3 GHz in dB obtained without the metal plate.

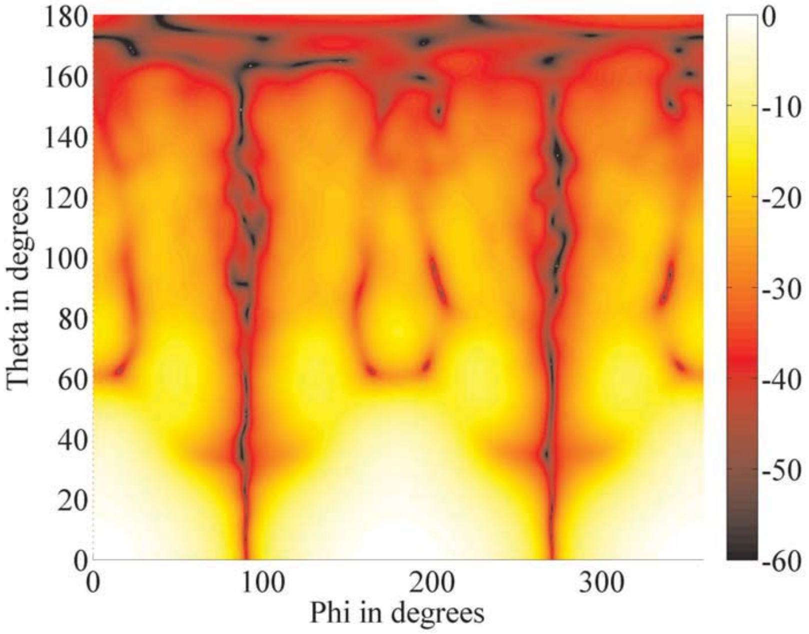

Figure 7.12: Normalized E_ϕ far-field pattern of the HF906 broadband antenna at 3 GHz in dB obtained without the metal plate.

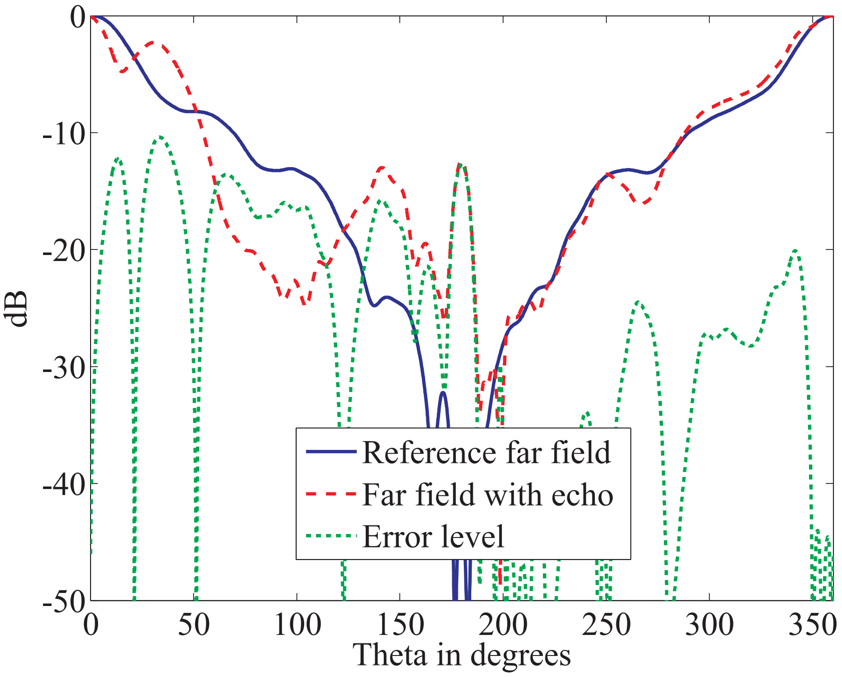

(a) Obtained from near-field data on a single measurement sphere.

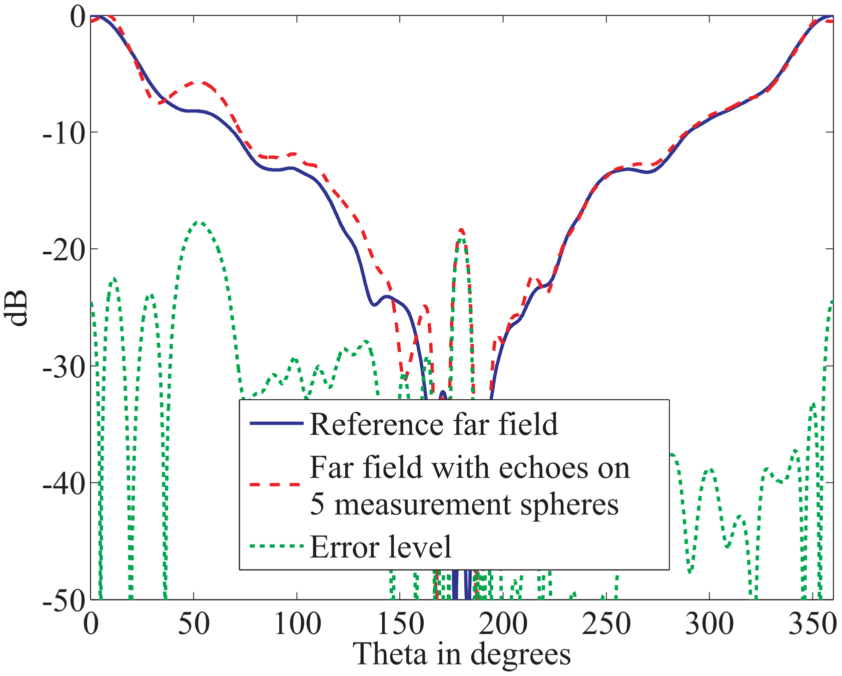

(b) Obtained from near-field data on five measurement spheres.

Figure 7.13: Phi = 90° cut for E_θ for the measurement set-up in Fig. 7.9

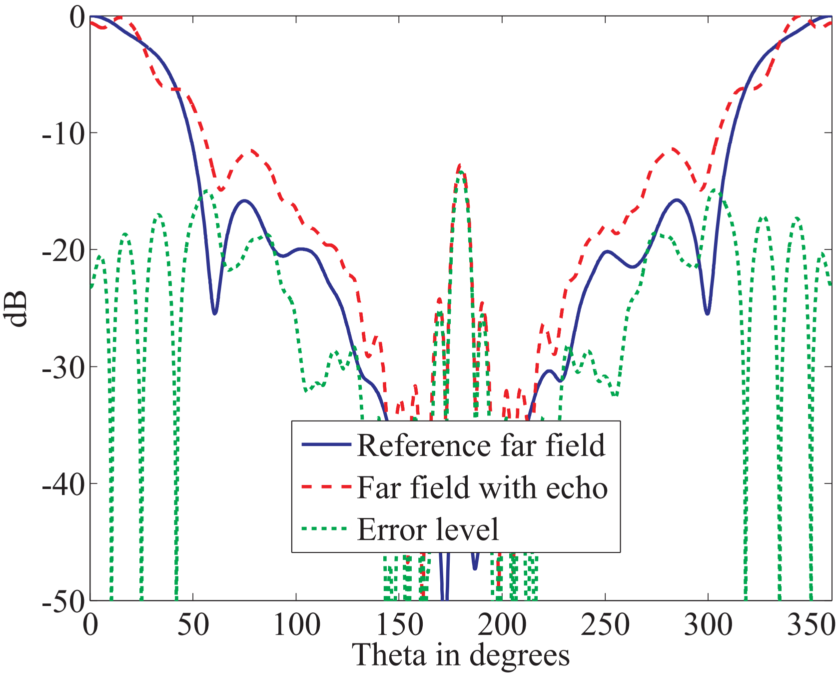

(a) Obtained from near-field data on a single measurement sphere.

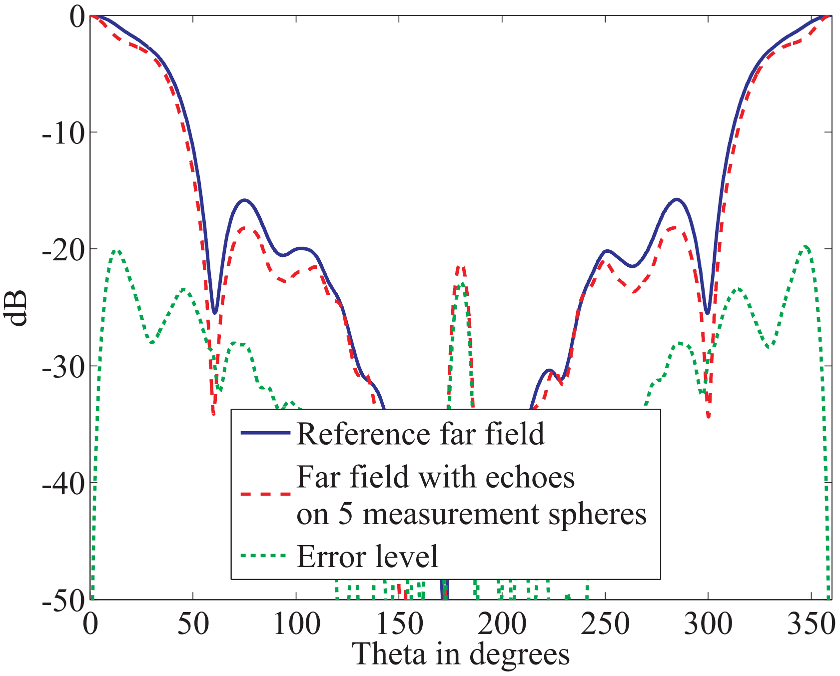

(b) Obtained from near-field data on five measurement spheres.

Figure 7.14: Phi = 0° cut for E_ϕ for the measurement set-up in Fig. 7.9

7.2 Singular Value Decomposition

In linear algebra, the singular value decomposition (SVD) is a popular matrix factorization method used to decompose a matrix

$$\mathbf{A}_{mn} = \mathbf{U}_{mm}\mathbf{\Sigma}_{mn}\mathbf{V}_{nn}^{H} \tag{7.1}$$

into two orthogonal matrices $\mathbf{U}$ and $\mathbf{V}$ and one diagonal matrix $\mathbf{\Sigma}$ containing the singular values of $\mathbf{A}$ usually arranged in descending order. The symbol ^{H} denotes complex conjugate transpose and (m,n) denote the sizes of the matrices. Measurements on multiple spheres contain the same number of modes from the AUT but the modes related to the echo sources are different depending on the measurement radius. This kind of problems are usually solved by utilizing the singular value decomposition to retrieve the signal component that is common to all the measurements. Ideally, the main signal and the interfering signal should be uncorrelated. This is not the case for antenna measurements since the echo signals are directly generated by the AUT and probe interaction. The technique, however, can help to remove some echo contributions and random noise generated through the measurement process. In this technique, the far field is obtained separately for each of the near-field data on the spheres. The several plane wave coefficients are then partitioned into a matrix of size M x N where M is the number of plane wave samples and N is the number of measurement spheres. Since the plane wave coefficients are obtained for the same AUT, this matrix should ideally be a rank 1 matrix. However, due to the variation of the echo signal on the different measurement spheres, the rank of the matrix can be greater than 1. The matrix containing the plane wave coefficients is then expanded into three matrices $\mathbf{A}_1 = \mathbf{U}\mathbf{\Sigma}_1\mathbf{V}^{H}$, where $\mathbf{U}$ and $\mathbf{V}$ coincide with the left-singular and right-singular vectors obtained from the SVD of the matrix $\mathbf{A}$, respectively. The diagonal matrix $\mathbf{\Sigma}_1$ contains the largest singular value of $\mathbf{A}$ with all other singular values set to zero [Manning et al., 2009]. This procedure is used to find the optimal low rank approximation of matrices in a least square sense where one simply sets the desired number of singular values to zero, a result known as the Eckart-Young theorem [Martin and Porter, 2011]. In this way, the rank of matrix $\mathbf{A}$ is downgraded to 1.

For the measurement set-up shown in Fig.7.6, the near-field data was measured over 5 measurement spheres as described previously. The plane wave coefficients were, however, obtained separately for each of the measurement spheres resulting in five different far-field patterns. The plane wave coefficients are then partitioned into a single matrix of size M x 5. The matrix is thereafter processed by utilizing the SVD and setting all except the maximum singular value to zero. The result obtained from the first column of the new matrix is shown in Fig. 7.15. Similar processing of the data measured on multiple sphere for the measurement with the metal plates resulted in the far-field pattern shown in Fig. 7.16. The results are similar to the ones obtained by a joint processing of the measurements acquired on the multiple spheres.

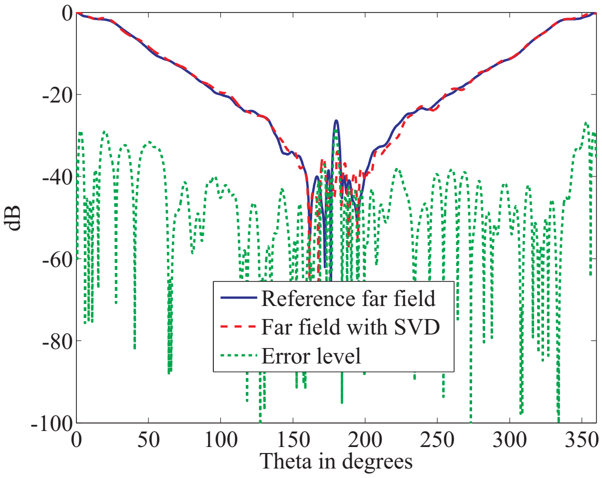

(a) Phi = 90° cut for E_θ

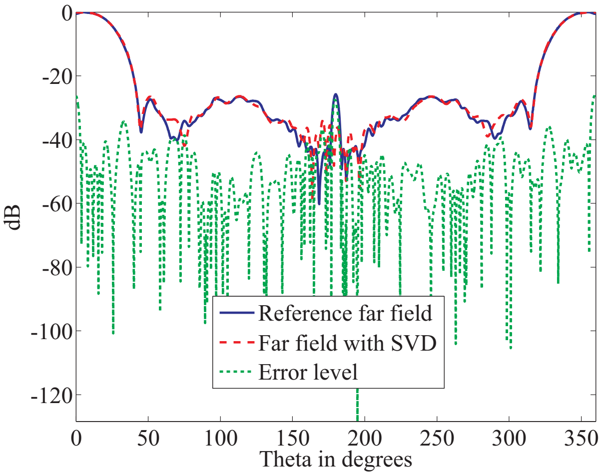

(b) Phi = 0° cut for E_ϕ

Figure 7.15: Far-field pattern for the measurement set-up in Fig. 7.6 (with bucket) obtained with the SVD technique.

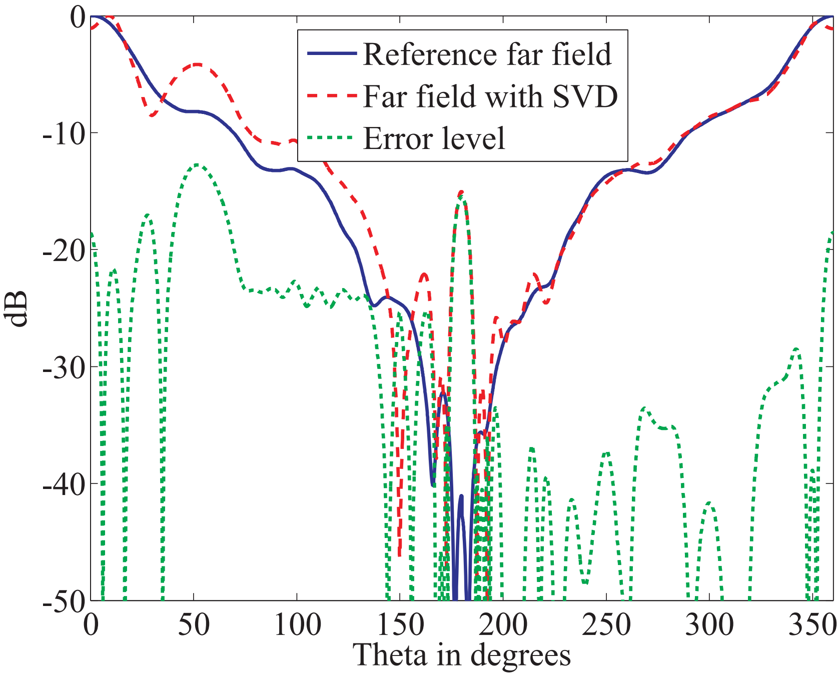

(a) Phi = 90° cut for E_θ

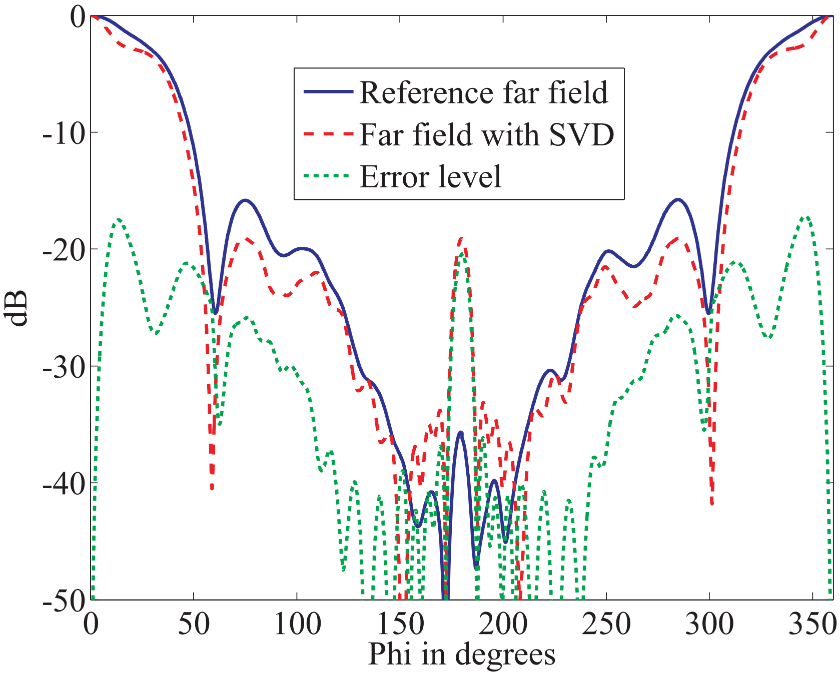

(b) Phi = 0° cut for E_ϕ

Figure 7.16: Far-field pattern for the measurement set-up in Fig. 7.9 (with metal plates) obtained with the SVD technique.

7.3 Summary

In this chapter, statistical techniques for echo suppression in near-field antenna measurements were presented. The techniques are based upon multiple observations of the near field on measurement surfaces with different measurement distances. The multiple observations contain a fixed number of modal contributions from the AUT but varying contributions from the echo sources allowing for techniques derived from the principal component analysis. Echo suppression is achieved by jointly processing the near-field data acquired on the multiple surfaces with the plane wave based NFFFT algorithm or by obtaining the far-field patterns separately from each near-field measurement and applying the SVD technique on the far fields. Both techniques result in an improved far-field pattern from echoic near-field data. However, joint processing of the near-field data results in a better echo suppression.

Chapter 8

Summary and Future Work

Measurement and post-processing techniques for improving the quality of far-field patterns obtained when antennas are measured in non-anechoic environments were presented. The techniques take advantage of certain a priori information about the AUT and the measurement environment. These techniques are summarized in Table 8.1. In particular, the scattering centers representation utilizes auxiliary sources to replace echo sources during the process of the near-field far-field transformation. The acquired near-field data is therefore attributed to both the AUT and the contributing echo sources. Once the equivalent sources representing only the AUT are obtained, the far-field pattern without echo contributions are thereafter evaluated. For non-localized echo sources, a technique was presented to evaluate the direction from which the dominant echo sources were received. This is done by terminating the iterative solution for the linear system of equation at an early stage and obtaining an estimate of the AUT far-field pattern. The far-field residual at this stage provides useful information regarding the directions of the echo sources. It was also demonstrated that once the directions of the echo contributions are known, very good echo suppression can be achieved since the scattering centers representation is robust to errors in the radial placement of auxiliary sources. Results were presented both for point sources through synthetic echo data and for real echo measurements generated in the measurement chamber. For real echo sources, it was found to be more efficient to use several small auxiliary sources over the surface of the echo source than to use one large auxiliary source. This is because small sources incorporate more a priori information about the dimension of the target echo source.

Measurement	Post-processing	Application
Single probe	PWE with auxiliary sources assumed for echo sources. (Chapter 4)	Works well when echo sources are in the directions where the probe is sensitive for the considered measurement points.
	Weighting and combination of neighboring measurement points. (Chapter 6)	Measurement errors can be compounded. Should be used with very accurate measurement equipments. Echo locations are not required.
Inward and outward probe	PWE with auxiliary sources assumed for echo sources. (Section 5.2)	For localized echo sources. Algorithm for localizing dominant echo sources is presented. Applicable to measurements with fixed AUT.
	SWE with incoming and outgoing waves. (Section 5.3)	When echo locations are not known. It requires angular oversampling of near-field data.
Measurement on multiple surfaces enclosing the AUT.	Use measurements on multiple surfaces as additional constraints in linear system of equation for PWE. (Chapter 7)	Echo locations are not required. Measurement time is relatively long due to measurements with multiple distances.
	Apply truncated SVD technique to far-fields from different measurement surfaces. (Section 7.2)	

Table 8.1: Summary of the presented echo suppression techniques.

In order to characterize sources within and outside a measurement volume, it is theoretically necessary to measure both the electric field and the magnetic field distribution on the measurement surface. This can be achieved by utilizing electric and magnetic dipoles or by means of Huygens' source probes which measures a linear combination of the electric and magnetic fields. The multi-probe technique involves measuring the AUT with two sets of probe antennas, namely, inward and outward sets of probes. This ensures that enough information is gathered to resolve both the incoming and outgoing waves from the measurement volume. The measured echoic near-field data was transformed using a plane wave based NFFFT with the effect of the echo sources integrated by means of auxiliary sources. The proposed technique results in a substantial improvement in the far-field pattern obtained from echoic near-field data. Additional measurement samples are required due to the new sets of probe antennas but the technique does not require an increase in the measurement distance or in the sampling density and it is not restricted to canonical measurement geometries. The method is restricted to measurements with a fixed AUT. A great advantage is the adaptability of the scattering centers e.g. in planar measurements the scattering centers amplitude can adapt to the varying echo contributions due to the influence of moving scanner parts.

The location of the AUT during the measurement is usually known and required for most NFFFT algorithms. The beamforming technique takes advantage of this a priori information to improve the signal to echo ratio and to improve the obtained far-field pattern of the AUT from echoic near-field measurements. In this technique the signals from neighboring measurement points are combined and carefully weighted such that the synthetic probe array is steered toward the AUT. This gives the spatial filtering advantages of a larger probe without the penalty of numerical errors due to probe insensitivity which occurs from electrically large probes. The filtered near-field data in this case can be seen as though it is measured with several probes of different sizes depending on the number of points that are being combined. Traditional modal NFFFT algorithms are not able to correct for such probe antennas. However, the flexibility of the plane wave based NFFFT algorithms, allows for specification of different probes for different measurement points.

The idea of taking measurements on multiple planes to reduce the impact of multiple reflection in planar near-field measurements is well-known in the antenna measurement community. A similar technique for echo suppression in antenna measurements was presented for spherical measurements. In this technique, the near-field distribution of the AUT is measured over several concentric spheres. The far field obtained jointly from all the measurement points typically has lower effects from the echo when compared with the far field obtained from the near field on a single measurement sphere. The post-processing with the singular value decomposition was also explained whereby the far field from each measurement sphere is obtained separately. The SVD technique is then applied to the far fields in order to obtain the echo-free far field pattern. The technique requires additional measurement time, however, it is also applicable to narrowband antennas and probes as opposed to time domain echo suppression techniques which require broadband AUT and probes.

The presented multi-probe measurement technique is applicable in situations where the AUT is fixed. However, for most available positioner systems, this is not the case. The AUT is usually mounted on a roll-over-azimuth positioner such that most of the movement is done by the AUT and the probe remains fixed. Measurements on multiple surfaces and application of the SVD is suitable for this measurement set-ups. Also, scattering center placement for cylindrical measurement with rotating AUT has been described. More advanced positioners such as those equipped with robotic arms will allow a more flexible choice regarding the orientation of the probe antenna. The representations of the scattering centers can be done in a multi-level manner such that neighboring scattering centers are combined and fewer direct plane translations are performed from the scattering centers to the probe. New applications can also be found for the presented techniques. It will be interesting and useful to investigate the applicability of the beamforming technique and scattering centers representation for far-field measurements and compact antenna ranges.

Bibliography

J. L. Araque Quijano, G. Vecchi, M. Sabbadini, L. Scialacqua, B. Bencivenga, F. Mioc, and L. Foged. Source reconstruction in advanced processing of antenna measurements. *5th European Conf. on Antennas and Propag. (EuCAP), Rome, Italy*, April 2011.

C. A. Balanis. *Antenna Theory: Analysis and Design*. John Wiley & Sons, Inc., Hoboken, New Jersey, 2005.

C. A. Balanis. *Modern Antenna Handbook*. Wiley-Interscience, New York, NY, USA, 2008.

S. R. Best. Progress in the design and realization of an electrically small huygens source. *Int. Workshop on Antenna Technology (iWAT), Lisbon, Portugal*, March 2010.

D. N. Black, Jr. and E. B. Joy. Test zone field compensation. *IEEE Trans. Antennas Propag.*, 43(4):362–368, April 1995.

S. Blanch, L. Jofre, and J. Romeu. Comparation between classical and equivalent current approach near-field to far-field transformation. In *Antennas and Propagation Society International Symposium*, volume 1, pages 260–263 vol.1, June 1995.

M. D. Blech, M. M. Leibfritz, R. Hellinger, D. Geier, F. A Maier, A. M. Pietsch, and T. F. Eibert. Time-domain spherical near-field antenna measurement system employing a switched continuous-wave hardware gating technique. *IEEE Trans. Instrum. Meas.*, 59 (2):387–395, February 2010.

O. M. Bucci and C. Gennarelli. Application of nonredundant sampling representations of electromagnetic fields to NF-FF transformation techniques. *International Journal of Antennas and Propagation*, 2012(1):1–14, 2102.

O. M. Bucci and D. Migliore. A new method for avoiding the truncation error in near-field antennas measurements. *IEEE Trans. Antennas Propag.*, 54(10):2940–2952, October 2006.

O. M. Bucci, C. Gennarelli, G. Riccio, and C. Savarese. Non-redundant representation of electromagnetic fields over a cylinder: an effective source modelling for elongated antennas. In *Antennas and Propagation Society International Symposium Digest*, volume 1, pages 565–568 vol.1, July 1996.

O. M. Bucci, C. Gennarelli, and C. Savarese. Representation of electromagnetic fields over arbitrary surfaces by a finite and nonredundant number of samples. *IEEE Trans. Antennas Propag.*, 46(3):351–359, March 1998.

D. Calvetti, B. Lewis, and L. Reichel. GMRES, l-curves, and discrete ill-posed problems. *BIT Numerical Mathematics*, 42:44–65, 2002a.

D. Calvetti, B. Lewis, and L. Reichel. On the regularizing properties of the GMRES method. *Numerische Mathematik*, 91:605–625, 2002b.

F. Cano, M. Sierra-Castaner, S. Burgos, and J. L. Besada. Applications of sources reconstruction techniques: Theory and practical results. *4th European Conf. on Antennas and Propag. (EuCAP), Barcelona, Spain.*, 2010.

F. J. Cano-Fácila, S. Burgos, F. Martín, and M. Sierra-Castañer. New reflection suppression method in antenna measurement systems based on diagnostic techniques. *IEEE Trans. Antennas Propag.*, 59(3):941–949, March 2011.

R. Coifman, V. Rokhlin, and S. Wandzura. The fast multipole method for the wave equation: a pedestrian prescription. *IEEE Antennas Propag. Mag.*, 35(3):7–12, June 1993.

F. D'Agostino, F. C. Gennarelli, R. Guerriero, and G. Riccio. An effective technique for reducing the truncation error in the near-field-far-field transformation with plane-polar scanning. *Progress In Electromagnetics Research*, 73:213–238, 2007.

F. D'Agostino, F. Ferrara, C. Gennarelli, G. Gennarelli, R. Guerriero, and M. Migliozzi. On the direct non-redundant near-field-to-far-field transformation in a cylindrical scanning geometry. *IEEE Antennas Propag. Mag.*, 54(1):130–138, February 2012.

R. H. Direen, M. H. Francis, and R. C. Wittmann. Near-field spherical scanning: Test-zone field evaluation. *3rd European Conf. on Antennas and Propag. (EuCAP), Berlin, Germany*, March 2009.

E. W. M. Dudok and D. Fasold. Analysis of compact antenna test range configurations. *International Symposium on Antennas, Nice, France*, 1986.

B. Fourestie, Z. Altman, J. Wiart, and A. Azoulay. On the use of the matrix-pencil method to correlate measurements at different test sites. *IEEE Trans. Antennas Propag.*, 47(10): 1569–1573, October 1999.

M. H. Francis, R. C. Wittmann, D. R. Novotny, and J. A. Gordon. Spherical near-field measurement results at millimeter-wave frequencies using robotic positioning. *AMTA 36th Annual Meeting & Symp., Tucson, USA*, October 2014.

R. W. Freund and N. M. Nachtigal. QMR: a quasi-minimal residual method for non-hermitian linear systems. *Numerische Mathematik*, 60(1):315–339, 1991.

A. Geise, T. Fritzel, H. Steiner, C. Schmidt, and M. Paquay. A portable antenna measurement system for large-scale and multi-contour near-fields. *AMTA 36th Annual Meeting & Symp., Tucson, USA*, October 2014.

C. G. Gonzalez, Y. Alvarez Lopez, A. D. Casas, and F. Las-Heras. Characterization of antenna interaction with scatterers by means of equivalent currents. *Progress Electromagn. Res.*, 116(6):185–202, 2011.

S. F. Gregson, J. McCormick, and C. G. Parini. *Principles of Planar Near-Field Antenna Measurements*. The Institution of Engineering and Technology, London UK, 2007.

S. F. Gregson, A. C. Newell, and G. E. Hindman. Reflection suppression in cylindrical near-field antenna measurememnt systems. *AMTA 31st Annual Meeting & Symp., Salt Lake City, Utah, USA*, November 2009.

S. F. Gregson, A. C. Newell, and G. E. Hindman. Behaviour of orthogonal wave functions and the correction of antenna measurements taken in non-anechoic environments. *Antennas and Propagation Conference (LAPC), Loughborough, UK*, November 2013.

M. Hajian, L. P. Ligthart, and M. Tian. The theory and practice of planar near-field measurements of delft university of technology. *IEEE Instrumentation and Measurement Technology Conference, Irvine, CA*, May 1993.

J. E. Hansen. *Spherical Near-Field Antenna Measurements*. Peter Peregrinus Ltd., London, 1988.

P. Hansen and F. Larsen. Suppression of reflections by directive probes in spherical near-field measurements. *IEEE Trans. Antennas Propag.*, 32(2):119–125, February 1984.

P. C. Hansen. Truncated singular decomposition solutions to discrete ill-posed problems with ill-determined numerical rank. *SIAM, J. Sci. Comput.*, 11(3):503–518, May 1990.

J. Hartmann, J. Habersack, and H.-J. Steiner. Antenna measurement in compact ranges. *Workshop on Space Borne Antennae Technologies and Measurement Techniques, Ahmedabad, India*, 2002.

D. W. Hess. The IsoFilter$^{\text{TM}}$ technique: A method of isolating the pattern of an individual radiator from data measured in a contaminated environment. *IEEE Antennas Propag. Mag.*, 52(1):174–181, February 2010.

D. W. Hess. A theoretical description of the IsoFilter$^{\text{TM}}$ rejection curve. *5th European Conference on Antennas and Propagation (EuCAP), Rome, Italy*, April 2011.

D. W. Hess and S. McBride. Applicability of IsoFilter$^{\text{TM}}$ selectivity to antenna diagnostics. *4th European Conference on Antennas and Propagation (EuCAP), Barcelona, Spain*, April 2010.

M. R. Hestenes and E. Stiefel. Methods of conjugate gradients for solving linear systems. *Journal of Research of the National Bureau of Standards*, 49(6):409–436, December 1952.

D. A. Hill. *Spherical-wave characterization of interior and exterior electromagnetic sources*. Nat. Inst. of Standards and Technology (NIST), Boulder, Colo., 1997.

D. A. Hill. Spherical-wave characterization of interior and exterior sources. *IEEE Int. Symp. on Electromagn. Compat., Denver, USA*, August 1998.

G. E. Hindman and A. C. Newell. Reflection suppression in large spherical near-field range. *AMTA 27th Annual Meeting & Symp., Newport, RI, USA*, October 2005.

IEEE. IEEE standard definitions of terms for antennas. *IEEE Std 145-1993*, pages 1–32, April 2013.

R. C. Johnson, H. A. Ecker, and J. S. Hollis. Determination of far-field antenna patterns from near-field measurements. *Proceedings of the IEEE*, 61(12):1668–1694, December 1973.

U. Karthaus, T. Bierhoff, and R. Noe. Innovative low-cost antenna measurement method based on correlation technique. *1st International Symposium on Communications and Digital Signal Processing, Sheffield Hallam University, UK*, April 1998.

T. Laitinen and O. Breinbjerg. A first/third-order probe correction technique for spherical near-field antenna measurements using three probe orientations. *IEEE Trans. Antennas Propag.*, 56(5):1259–1268, May 2008.

T. A. Laitinen, J. M. Nielsen, S. Pivnenko, and O. Breinbjerg. Errors of first-order probe correction for higher-order probes in spherical near-field antenna measurements. *URSI EMTS International Symposium on Electromagnetic Theory, Pisa, Italy*, May 2004.

C. Lanczos. Solution of systems of linear equations by minimized iterations. *Journal of Research of the National Bureau of Standards*, 49:3353, 1952.

W. Leach, Jr. and D. Paris. Probe compensated near-field measurements on a cylinder. *IEEE Trans. Antennas Propag.*, 21(4):435–445, July 1973.

P. S. H. Leather, J. D. Parsons, and J. Romeu. Signal processing techniques improve antenna pattern measurement. pages 97–100, May 2004a.

P. S. H. Leather, J. D. Parsons, J. Romeu, S. Blanch, and A. Aguasca. Practical validation of antenna pattern measurement interference cancellation using a correlation technique. In *IEEE Antennas and Propagation Society International Symposium*, volume 1, pages 735–738 Vol.1, June 2004b.

J. J. Lee, E. M. Ferren, D. P. Woollen, and K. M. Lee. Near-field probe used as a diagnostic tool to locate defective elements in an array antenna. *IEEE Trans. Antennas Propag.*, 36 (6):884–889, June 1988.

M. M. Leibfritz, M. D. Blech, F. M. Landstorfer, and T. F. Eibert. A comparison of software- and hardware-gating techniques applied to near-field antenna measurements. *Advances in Radio Science*, (5):43–48, 2007a.

M. M. Leibfritz, F. M. Landstorfer, and T. F. Eibert. Diagnosis of antenna-arrays using near-field antenna measurements and a priori information. *IEEE Antennas and Propagation Society International Symposium, Honolulu, USA*, June 2007b.

G. Leon, S. Loredo, S. Zapatero, and F. Las-Heras. Radiation pattern error corrections based on matrix pencil method. *IEEE Antennas and Propagation Society International Symposium, San Diego, USA*, July 2008.

G. Leon Fernandez, S. Loredo, S. Zapatero, and F. Las-Heras. Radiation pattern retrieval in non-anechoic chambers using the matrix pencil algorithm. *Progress Electromagn. Res. Lett.*, 9(6):119–127, 2009.

S. Loredo, M. R. Pino, F. Las-Heras, and T. K. Sarkar. Echo identification and cancellation techniques for antenna measurement in non-anechoic test sites. *IEEE Antennas Propag. Mag.*, 46(1):100–107, February 2004.

S. Loredo, G. Leon, S. Zapatero, and F. Las-Heras. Measurement of low-gain antennas in non-anechoic test sites through wideband channel characterization and echo cancellation [measurements corner]. *IEEE Antennas Propag. Mag.*, 51(1):128–135, February 2009.

A. Ludwig. Near-field far-field transformations using spherical-wave expansions. *IEEE Trans. Antennas Propag.*, 19(2):214–220, March 1971.

A. Ludwig. The definition of cross polarization. *IEEE Trans. Antennas Propag.*, 21(1): 116–119, January 1973.

C. D. Manning, P. Raghavan, and H. Schütze. *An Introduction to Information Retrieval*, page 410. Cambridge University Press, Cambridge, England, 2009.

C. D. Martin and M. A. Porter. The extraordinary svd. 2011.

G. F. Masters. Coordinate system plotting for antenna measurements. *Nearfield Systems Inc.*, 2014.

J. Moon, S. Oh, and Y. Jung. Echo-cancellation technique with recursive data in nonanechoic test sites. *IEEE Antennas and Wireless Propagation Letters*, 8:558–560, 2009.

Nearfield Systems, Inc. Open ended waveguide (OEWG) probes, 2014.

W. G. Newall and T. S. Rappaport. An antenna pattern measurement technique using wideband channel profiles to resolve multipath signal component. *AMTA 19th Annual Meeting & Symp., Boston, USA*, November 1997.

A. C. Newell. Error analysis techniques for planar near-field measurements. *IEEE Trans. Antennas Propag.*, 36(6):754–768, June 1988.

A. C. Newell. Near field antenna measurement theory, planar, cylindrical and spherical. *Lecture Notes, Near-Field Systems Inc.*, 2009.

A. C. Newell and M. L. Crawford. *Planar near-field measurements on high performance array antennas*. National Bureau of Standards, NBSIR 74-380, 1974.

A. C. Newell and S. F. Gregson. Estimating the effect of higher order modes in spherical near-field probe correction. *AMTA 35th Annual Meeting & Symp., Columbus, USA*, October 2013.

A. D. Olver. Compact antenna test ranges. *Seventh International Conference on Antennas and Propagation ICAP, York, UK*, April 1991.

D. Paris, W. Leach, Jr., and E. B. Joy. Basic theory of probe-compensated near-field measurements. *IEEE Trans. Antennas Propag.*, 26(3):373–379, May 1978.

P. Petre and T. K. Sarkar. Planar near-field to far-field transformation using an equivalent magnetic current approach. *IEEE Trans. Antennas Propag.*, 40(11):1348–1356, November 1992.

P. Petre and T. K. Sarkar. Planar near-field to far-field transformation using an array of dipole probes. *IEEE Trans. Antennas Propag.*, 42(4):534–537, April 1994.

R. J. Pogorzelski. Extended probe instrument calibration (EPIC) for accurate spherical near-field antenna measurements. *IEEE Trans. Antennas Propag.*, 57(10):3366–3375, October 2009.

R. J. Pogorzelski. Experimental demonstration of the extended probe instrument calibration (EPIC) technique. *IEEE Trans. Antennas Propag.*, 58(6):2093–2097, June 2010.

J. L. A. Quijano and G. Vecchi. Field and source equivalence in source reconstruction on 3D surfaces. *Progress In Electromagnetics Research*, 103:67–100, 2010.

J. L. A. Quijano, L. Scialacqua, J. Zackrisson, L. J. Foged, M. Sabbadini, and G. Vecchi. Suppression of undesired radiated fields based on equivalent currents reconstruction from measured data. *IEEE Antennas and Wireless Propagation Letters*, 10:314–317, 2011.

M. A. Qureshi, C. H. Schmidt, and T. F. Eibert. Comparative probe parameter error analysis for planar near-field measurements with a novel approach for reduced probe-aut interaction. *AMTA 34st Annual Meeting & Symp., Seattle, USA*, October 2012a.

M. A. Qureshi, C. H. Schmidt, K. A. Yinusa, and T. F. Eibert. Far-field uncertainty due to instrumentation errors in multilevel plane wave based near-field far-field transformed planar near-field measurements. *6th European Conf. on Antennas and Propag. (EuCAP), Prague, Czech Republic*, March 2012b.

M. A. Qureshi, C. H. Schmidt, and T. F. Eibert. Adaptive sampling in spherical and cylindrical near-field antenna measurements. *IEEE Antennas Propag. Mag.*, 55(1):243–249, March 2013.

RF Spin. *http://www.rfspin.cz/en/antennas/drh18.php*, 2014.

Rohde & Schwarz. *http://www2.rohde-schwarz.com*, 2014.

Y. Saad. *Iterative Methods for Sparse Linear Systems*. Society for Industrial and Applied Mathematics Philadelphia, PA, USA, 2003.

Y. Saad and M. H. Schultz. GMRES: A generalized minimal residual algorithm for solving nonsymmetric linear systems. *SIAM J. Sci. and Stat. Comput.*, 7:856–869, 1986.

D. Sánchez-Escuderos, M. Baquero-Escudero, J. I. Herranz-Herruzo, and F. Vico-Bondía. Iterative algorithm for probe calibration in spherical near-field antenna measurement. *IEEE Trans. Antennas Propag.*, 58(9):3069–3074, 2010.

T. K. Sarkar and O. Pereira. Using the matrix pencil method to estimate the parameters of a sum of complex exponentials. *IEEE Antennas Propag. Mag.*, 37(1):48–55, February 1995.

T. K. Sarkar and A. Taaghol. Near-field to near/far-field transformation for arbitrary near-field geometry utilizing an equivalent electric current and mom. *IEEE Trans. Antennas Propag.*, 47(3):566–573, March 1999.

V. Schejbal, V. Kovarik, and D. Cermak. Synthesized-reference-wave holography for determining antenna radiation characteristics. *IEEE Trans. Antennas Propag.*, 50(5):71–83, October 2008.

C. H. Schmidt and T. F. Eibert. Multilevel plane wave based near-field far-field transformation for electrically large antennas in free-space or above material halfspace. *IEEE Trans. Antennas Propag.*, 57(5):1382–1390, May 2009.

C. H. Schmidt and T. F. Eibert. Sub spectra representation of antennas for plane wave based near-field far-field transformation at short measurement distances. *IEEE Antennas and Propagation Society International Symposium, Chicago, IL, USA*, July 2012.

C. H. Schmidt, M. M. Leibfritz, and T. F. Eibert. Fully probe-corrected near-field far-field transformation employing plane wave expansion and diagonal translation operators. *IEEE Trans. Antennas Propag.*, 56(3):737–746, March 2008.

C. H. Schmidt, D. T. Schobert, and T. F. Eibert. Electric dipole based synthetic data generation for probe-corrected near-field antenna measurements. *5th European Conf. on Antennas and Propag. (EuCAP), Rome, Italy*, April 2011.

D. Slater. Near field test facility design. *Antenna Measurement Technique Association AMTA Conference, Redondo Beach, CA*, 1985.

A. N. Tikhonov and V. Y. Arsenin. *Solution of Ill-posed Problems*. Winston & Sons, Washington, USA, 1977.

J. T. Toivanen, T. A. Laitinen, and P. Vainikainen. Modified test zone field compensation for small-antenna measurements. *IEEE Trans. Antennas Propag.*, 58(11):3471–3479, November 2010.

UVSAR. *http://www.exchange3d.com*.

J. J. H. Wang. An examination of the theory and practices of planar near-field measurement. *IEEE Trans. Antennas Propag.*, 36(6):746–753, June 1988.

G. A. Watson. Conjugate gradient methods for indefinite systems. *Proceedings of the Dundee Biennal Conference on Numerical Analysis*, page pp. 7389., 1974.

R. C. Wittmann. Spherical near-field scanning: determining the incident field near a rotatable probe. *Antennas and Propagation Society International Symposium, Dallas, TX, USA*, May 1990.

P. J. Wood. The prediction of antenna characteristics from spherical near field measurements. part I - theory. *Marconi Review*, 40(204):42–68, March 1977a.

P. J. Wood. The prediction of antenna characteristics from spherical near field measurements. part II - experimental validation. *Marconi Review*, 40(205):117–155, March 1977b.

P. Xu. Truncated svd methods for discrete linear ill-posed problems. *Geophysical Journal International*, 135(2):505–514, 1998.

A. D. Yaghjian. *Upper-bound errors in far-field antenna parameters determined from planar near-field measurements : PART 1: analysis*. NBS Technical Note 667, U.S. Government Printing Office, Washington, DC, USA, 1975.

A. D. Yaghjian. *Near-field antenna measurement on a cylindrical surface: a source scattering matrix formulation*. NBS Technical Note 696, U.S. Government Printing Office, Washington, DC, USA, 1977.

A. D. Yaghjian. An overview of near-field antenna measurements. *IEEE Trans. Antennas Propag.*, 34(1):30–45, January 1986.

K. A. Yinusa and T. F. Eibert. Echo suppression by means of multi-probe antenna measurements. *AMTA 35th Annual Meeting & Symp., Columbus, USA*, October 2013a.

K. A. Yinusa and T. F. Eibert. Multi-probe measurement technique for echo suppression in near-field measurements. *7th European Conference on Antennas and Propagation (EuCAP), Gothenburg, Sweden*, April 2013b.

K. A. Yinusa and T. F. Eibert. A multi-probe antenna measurement technique with echo suppression capability. *IEEE Trans. Antennas Propag.*, 61(10):5008–5016, October 2013c.

K. A. Yinusa, C. H. Schmidt, and T. F. Eibert. Scattering centers modeling of non-anechoic measurement environments. *Kleinheubacher Tagung, Miltenberg, Germany*, September 2011.

K. A. Yinusa, C. H. Schmidt, and T. F. Eibert. Scattering centers modeling of non-anechoic measurement environments. *Advances in Radio Science*, 10:69 – 73, 2012a.

K. A. Yinusa, C. H. Schmidt, and T. F. Eibert. Modeling of unknown echoic measurement facilities with equivalent scattering centers. *6th European Conf. on Antennas and Propag. (EuCAP), Prague, Czech Republic*, March 2012b.

K. A. Yinusa, R. A. M. Mauermayer, and T. F. Eibert. Beamforming filtering for planar near-field antenna measurements. *AMTA 36th Annual Meeting & Symp., Tucson, USA*, October 2014.

List of Author’s Publications

- K. A. Yinusa, R. A. M. Mauermeyer and T. F. Eibert, Beamforming Filtering for Planar Near-Field Antenna Measurements, *36th Annual Antenna Measurement Techniques Association (AMTA) Symposium*, Tucson, USA, October 2014.
- K. A. Yinusa and T. F. Eibert, A multi-probe antenna measurement technique with echo suppression capability. *IEEE Trans. Antennas Propag.*, 61(10):5008-5016, October 2013. ISSN 0018-926X. doi: 10.1109/TAP.2013.2271495.
- K. A. Yinusa and T. F. Eibert, Echo Suppression by Means of Multi-Probe Antenna Measurements, *35th Annual Antenna Measurement Techniques Association (AMTA) Symposium*, Columbus, USA, October 2013.
- K. A. Yinusa and T. F. Eibert, Multi-Probe Measurement Technique for Echo Suppression in Near-Field Measurements, *7th European Conference on Antennas and Propagation (EUCAP)*, Gothenburg, Sweden, April 2013.
- K. A. Yinusa, C. H. Schmidt and T. F. Eibert, Modeling of Unknown Echoic Measurement Facilities with Equivalent Scattering Centers, *6th European Conference on Antenna and Propagation (EUCAP)*, Prag, Czech Republic, 2012.
- M. A. Qureshi, C. H. Schmidt, K. A. Yinusa and T. F. Eibert, Far-Field Uncertainty Due to Instrumentation Errors in Multilevel Plane Wave Based Near-Field Far-Field Transformed Planar Near-Field Measurements, *6th European Conference on Antennas and Propagation (EUCAP)*, Prag, Czech Republic, 2012.
- K. A. Yinusa, C. H. Schmidt and T. F. Eibert, Scattering Centers Modeling of Non-Anechoic Measurement Environments, *Advances in Radio Science*, Vol. 10, pages 69 - 73, 2012. doi: 10.5194/ars-10-69-2012.

- K. A. Yinusa, C. H. Schmidt and T. F. Eibert, Scattering Centers Modeling of Non-Anechoic Measurement Environments, *Kleinheubacher Tagung*, Miltenberg, Germany, September 2011.